論文 / 著書情報
Article / Book Information

題目(和文)	微構造の3次元可視化による焼結の熱力学的駆動力の解明
Title(English)	Clarification of thermodynamic driving force for sinteringfrom 3-D visualization of the microstructure
著者(和文)	大熊学
Author(English)	Gaku Okuma
出典(和文)	学位:博士(工学), 学位授与機関:東京工業大学, 報告番号:甲第10999号, 授与年月日:2018年9月20日, 学位の種別:課程博士, 審査員:若井 史博,東 正樹,尾中 晋,安田 公一,吉田 克己,西山 宣正,田中 諭
Citation(English)	Degree:Doctor (Engineering), Conferring organization: Tokyo Institute of Technology, Report number:甲第10999号, Conferred date:2018/9/20, Degree Type:Course doctor, Examiner:,,,,,,
学位種別(和文)	博士論文
Type(English)	Doctoral Thesis

Clarification of thermodynamic driving force for sintering from 3-D visualization of the microstructure

微構造の3次元可視化による焼結の熱力学的駆動力の解明

Tokyo Institute of Technology

School of Material and Chemical Technology

Gaku OKUMA

Contents

Chapter 1 Introduction **1**
1.1 Mechanical reliability of ceramics 1
1.2 What is sintering? 2
1.3 Continuum mechanics of sintering 5
1.4 Three-dimensional visualization of sintering 10
1.5 Objective of this research 12
1.6 Abstract of doctoral dissertation 13
References 15

Chapter 2 Interface topology for distinguishing stages of sintering **30**
2.1 Introduction 30
2.2 Experimental procedure 32
2.3 Results 34
2.3.1 Microstructural evolution in sintering 34
2.3.2 Euler characteristic for describing interface topology 36
2.3.3 Transition between different stages 38
2.4 Discussion 39
2.4.1 Comparison with other sintering mechanisms 39
2.4.2 Euler characteristic per unit volume 40
2.4.3 Simulation of topological evolution 41
2.4.4 Topology and sintering mechanics 43
2.5 Conclusions 45
References 46

Chapter 3 Computation of sintering stress and bulk viscosity for each stage of sintering **59**
3.1 Introduction 59
3.2 Experimental procedure 61
3.3 Results 62
3.3.1 Evolution of pore morphology observed by 3D visualization 62
3.3.2 Relative density and specific surface area 62
3.3.3 Curvature of pore surface 63
3.3.4 Sintering stress derived from three methods 64
3.3.5 Bulk viscosity 64

3.4 Discussion 65
3.4.1 Sintering stress in the initial stage of sintering 65
3.4.2 Sintering stress in constrained sintering 67
3.4.3 Pore coarsening in constrained sintering 68
3.5 Conclusions 70
References 71

Chapter 4 Experimental verification of sintering stress and bulk viscosity estimated from X-ray microtomography 82
4.1 Introduction 82
4.2 Mechanics of sinter forging 83
4.3 Experimental procedure 85
4.4 Results 86
4.5 Discussion 88
4.5.1 Methods to estimate sintering stress from the microstructure 88
4.5.2 Comparison with sinter forging results 89
4.5.3 Difference between the viscous sintering and the sintering of crystalline materials 90
4.6 Conclusions 92
References 93

Chapter 5 Determination of the size of representative volume element for viscous sintering 103
5.1 Introduction 103
5.2 Experimental procedure 104
5.3 Results and discussion 106
5.3.1 Micro structural evolution in viscous sintering 106
5.3.2 Relative density, specific surface area and sintering stress 107
5.4 Conclusions 110
References 111

Chapter 6 Summary 120

Acknowledgements 128

Chapter 1 Introduction

1.1 Mechanical reliability of ceramics

Ceramics has been widely used in modern industry due to its excellent characteristics. Ceramic materials are produced by powder processing, followed by sintering, that is, the thermal process of transforming powder compacts into complex shaped components (Fig. 1.1).[1] Powder processing involves four steps as follows; the powder manufacture, the powder preparation for consolidation, the consolidation to an engineering shape, and the densification development that eliminates void space.[2] However, each step in powder processing originate the microstructural heterogeneities. This heterogeneous density distribution may lead to inhomogeneous shrinkage, and generate internal stress during sintering. Since ceramics is a brittle material, strength depends on small flaws generated by internal stresses during sintering. Therefore, the mechanical reliability of ceramics depends on the control of heterogeneity in processing. Evans[3] described fracture occurs from void and cracks around inclusions inside specimens, as observed in Figure. 1.2. The difference in the strain rate produces stresses around rigid inclusions in sintering of composites, in sintering of thin films on substrates, and in sintering of multilayered systems such as low temperature co-fired ceramics (LTCC) and solid oxide fuel cells (SOFC). These stresses modify the shrinkage rate. They can generate cavities, cracks, delamination, and warping of the structure, even though there is no large void or cracks in the initial powder packings. Therefore, it is most important to understand what is the micro mechanics behind the defect formation during sintering.

1.2 What is sintering?

Sintering is one of the oldest technologies dating back to around 10,000years ago, nevertheless, the scientific approach to this technology has started only after 1940s. Sintering is known as a common technique of consolidating powder compacts by thermal energy. This technique provides an engineering process for the production of not only ceramics, but also metals, glasses, polymers and composites. A huge number of particles undergoes a change in shape at elevated temperatures by matter transport driven by surface tension, the kinetics of which is controlled by viscous flow for amorphous particles[4,5,6] or diffusion mechanisms for crystalline particles[7,8,9]. Since sintering occurs so as to decrease the total interface energy, surface area per unit volume, which is called specific surface area S_V, decreases with sintering time. Concurrently, the total pore volume decreases, thereby, the sintering process is described as densification using the relative density ρ as a state parameter. Then, ρ increases with time and approaches towards the maximum value of 1.

In 1961, Coble[8] illustrated in Figure 1.3 the evolution of particle-pore structure schematically, and identified three stages of sintering, (i) initial stage, (ii) intermediate stage, and (iii) final stage. Coble described about three stages of sintering, as follows;

(i) Initial stage

Initial stage is characterized as the formation and growth of contact between neighboring particles, where ρ increases from 0.5 to 0.6. In the initial stage, the mechanism of material transport during sintering of crystalline particle is presented as follows; lattice diffusion, grain boundary diffusion, surface diffusion, and gas phase transport. On the other hand, the viscous flow mechanism, which was first proposed by Frenkel[9], can be applied in the sintering of viscous materials like glass.

Fig. 1.4 illustrates the material transport paths during sintering[10]. The material transport due to the difference in interface curvature occurs under the parallel actions of various mechanisms, but the dominant mechanism depends on particle size r_0, neck radius (contact radius between particles *c*), temperature and time[11]. Some of these material transport mechanisms contribute to densification and shrinkage while others do not. The interparticle distance can be reduce only by bulk material flow via viscous flow or by grain boundary diffusion from the grain boundary to the surface. The materials transport from the particle surface to the neck increases the neck size, but do not contribute to the shrinkage of the interparticle distance. Therefore, the grain boundary is the source of material transport for densification and shrinkage in crystalline powder compacts. The lattice diffusion of atoms from the grain boundary to the neck allows the boundary to act as a site for vacancy annihilation. The shrinkage kinetics is expressed as follows[12];

$$\frac{\Delta l}{l} = \left(\frac{D_l \gamma_s V_m}{RTa^3} \right)^{1/2} t^{1/2} \tag{1.1}$$

where l is the sample size, γ_s is the solid surface energy, D_l is the lattice diffusion coefficient, V_m is the molar volume of the solid, and a is the particle radius.

In some respects material transport from the grain boundary to the neck by grain boundary diffusion is similar to diffusional creep by grain boundary diffusion.[13] For the grain boundary diffusion from grain boundaries, the shrinkage kinetics is expressed as follows;

$$\frac{\Delta l}{l} = \left(\frac{3D_b \delta_b \gamma_s V_m}{4RTa^4} \right)^{1/3} t^{1/3} \tag{1.2}$$

where D_b is the grain boundary diffusion coefficient and δ_b is the diffusion thickness of grain boundary diffusion. In this case the material transported to the neck surface by grain boundary diffusion should be redistributed via another mechanism. If the redistribution of material is not fast enough compared to the material transport by grain boundary diffusion, this secondary redistribution may control the neck growth.

For the viscous flow mechanism, if the material follows the behavior of a Newtonian fluid, the shrinkage kinetics is expressed as follows[4];

$$\frac{\Delta l}{l} \approx \frac{\gamma_s}{\mu a} t \tag{1.3}$$

where μ is the viscosity of material, a is the particle radius, and t is the sintering time.

(ii) Intermediate stage

In the intermediate stage, the pore structure evolves into an interconnected channel with cylindrical pore lying along three grain edges (see Fig 1.3(b)). Here, for the atom flux, two mechanisms are available: lattice diffusion and grain boundary diffusion[14].

For the lattice diffusion, the densification rate is expressed as follows;

$$\frac{d\rho}{dt} = \frac{336 D_l \gamma_s V_m}{RTG^3} \tag{1.4}$$

where $d\rho/dt$ is the densification rate, D_l is the lattice diffusion coefficient, V_m is the molar volume of the solid, G is the grain diameter. In reality, grain growth during sintering of crystalline particle, and hence, G is not constant parameter.

(iii) Final stage

The final stage begins when closed pores are formed by pinch-off of interconnected pore channels at ρ = 0.9. The final stage of sintering of crystalline particles is usually accompanied by coarsening and grain growth[15, 16]. Classical sintering theories, which predict the rate of density change, have been proposed with the assumption of

simplified geometrical model for each stage[8, 16]. For this model, the densification rate is expressed as follows[10];

$$\frac{d\rho}{dt} = \frac{288 D_l \gamma_s V_m}{RTG^3} \tag{1.5}$$

This equation indicates that the densification rate is inversely proportion to the cube of grain size. This result is the same as that found for the dependence of neck growth and shrinkage on particle size in the initial stage model.

1.3 Continuum mechanics of sintering

Continuum mechanics is a powerful method to predict the macroscopic dimensional changes, and also to analyze internal stresses generated during sintering of heterogeneous porous materials. When the microstructure is isotropic, the macroscopic deformation during sintering is expressed by the following constitutive equation[17-19]:

$$\dot{E}_{ij} = \frac{\Sigma'_{ij}}{2G} + \delta_{ij} \frac{\left(\Sigma_m - \Sigma^s\right)}{3K} \tag{1.6}$$

where $\dot{E}_{ij}$ is the macroscopic strain rate, Σ'_{ij} and Σ^m are deviatoric and hydrostatic components of macroscopic stress, Σ^s is the sintering stress, and G and K are the shear viscosity and the bulk viscosity, respectively. Note that the sign convention used for sintering stress, or sintering pressure,[20] is opposite to that used for stress, since pressure is positive if it is compressive. The densification rate is given by the trace of the macroscopic strain rate tensor $\dot{\rho}/\rho = -3\dot{E}$. In the absence of external and internal stresses, the true strain rate $\dot{E}$ in free sintering is proportional to the sintering stress:

$$\dot{E}_f = \frac{-\Sigma^s}{3K} \tag{1.7}$$

Here, Σ^s, G, and K, are not constant, and depend on the relative density, ρ. They depend on different factors, such as the nature of powders, powder processing, particle packing, sintering temperature, and grain growth.

Practically, the continuum model is useful in analyzing the effect of applied stress in stress-assisted sintering, such as hot pressing, spark plasma sintering, and hot isostatic pressing. It is also useful to predict the internal stress, which is generated from the difference in shrinkage rate in constrained sintering. In microscopic scale, void and cracks are generated by the microscopic stresses during constrained sintering. [17,21] For example, in the sintering of thin film on substrate (Fig. 1.5(a)), tensile stress is generated inside the film. This stress is proportional to the free sintering strain rate $\dot{E}$, which is caused by the sintering stress Σ^s. Here, the sintering stress is driving force for shrinkage, but it generates internal stress Σ^{film} in the film which suppresses shrinkage in constrained sintering. The internal stress is given by[17]:

$$\Sigma^{film} = \frac{E}{1-\nu}\dot{E}_f \tag{1.8}$$

where E_f is the free sintering strain rate (Eq. (1.7)), E is the uniaxial viscosity, and ν is the viscous Poisson's ratio. The internal stress suppresses shrinkage in constrained sintering, and induces cracks, debonding, or delamination in co-sintering of low temperature co-fired ceramics and solid oxide fuel cell.

The continuum mechanical parameters for sintering, Σ^s, G, and K, are not constant since they depend on the relative density of the compact. These sintering parameters are physical quantities that can be determined experimentally by sinter forging, in which strain rates are typically measured at a fixed applied stress for a specific microstructure. Figure 1.6 shows the uniaxial viscosity and sintering stress of

alumina powder during sintering determined by sinter forging.[22] This experimental result shows the uniaxial viscosity increases with increasing the relative density (Fig. 1.6 (a)), and the sintering stress varies with the relative density (Fig. 1.6 (b)). Sintering stress of pressure-filtrated compact increases, and becomes very large, more than 30 MPa. This stress is almost the same with that in hot pressing and spark plasma sintering. On the other hand, the sintering stress of dry pressed compact is small and does not vary significantly with densification. Their result is very important, because it shows that sintering stress depends on powder processing. The starting powder is most important for sintering. Furthermore, there are many powder processing methods; press forming, tape forming, slip casting, injection molding, and extrusion. The powder packing, which is either isotropic or anisotropic, depends on these processing methods. The macroscopic sintering stress and viscosity depends on the powder packing. The macroscopic shrinkage depends on sintering stress and viscosity. Therefore, the increase of sintering stress by optimized powder processing is the core technology of pressureless sintering. After all, clarification of the relationship between macroscopic and microscopic sintering parameters, such as sintering stress and bulk viscosity, is very important.

The sintering stress in macroscopic scale arises from the microscopic pore structures. The sintering stress can be defined rigorously for pore structures in equilibrium where the mechanical force just balances the surface tension forces, so that the porous materials do not shrink. The sintering stress is calculated from curvature and energy for periodic porous structures under the constraint of fixed volume, where the curvature is constant at any point on pore surface.[23] In the constant mean curvature (CMC) surface, the sintering stress Σ^s for viscous sintering of glass is calculated from

the curvature κ:

$$\Sigma^s = \gamma_s \kappa \tag{1.9}$$

where γ_s is the surface energy. Alternatively, the sintering stress is given by[24]:

$$\Sigma^s = \rho \gamma_s \kappa + \frac{2\gamma_s A_{pore}}{3V} \tag{1.10}$$

where A_{pore} is the total surface area in a volume element V.

Substitution of Equation (1.9) and $\rho = (V - V_{pore})/V$ into Equation (1.10) gives[25]:

$$\Sigma^s = \frac{2\gamma_s A_{pore}}{3V_{pore}} \tag{1.11}$$

where V_{pore} is the total pore volume in the volume element. The porous microstructure is characterized by the specific surface area $S_V \equiv A_{pore}/V$, then, Equation (1.11) is expressed as follows[26]:

$$\Sigma^s = \frac{2\gamma_s S_V}{3(1-\rho)} \tag{1.12}$$

The curvature method (Equation (1.9)), the mixed method (Equation (1.10)), and the surface energy method (Equations (1.11) and (1.12)) give the identical value for the CMC surface of glass.

However, real porous structures are nonequilibrium, nonperiodic, and nonuniform, then the curvature is not constant on pore surface. Here, we consider the final stage of sintering where closed pores are dispersed in a viscous material as shown in Fig. 1.7(b) [25]. Sintering stress of a pore of arbitrary shape is defined as:

$$\sigma_{ij}^s = \frac{1}{V_n} \int_{A_n} \gamma_s \left(\delta_{ij} - n_i n_j \right) dA \tag{1.13}$$

where n_i is the unit (outward) normal to the pore surface. The macroscopic sintering stress in V is defined as the volume average of local sintering stress of pores:

$$\Sigma_{ij}^{s} = \frac{1}{V_{pore}} \sum_{n} V_n \sigma_{ij}^{s} \tag{1.14}$$

where $V_{pore} = \sum_n V_n$ is the total pore volume.

A non-spherical pore has deviatoric components of local sintering stress. However, the macroscopic sintering stress is hydrostatic in isotropic structures, because a random distribution of arbitrary shaped pores does not confer any directional macroscopic properties. And hence, the hydrostatic sintering stress Σ^s is expressed as Eq. (1.11), and Σ^s is simply calculated from the total surface area and the total pore volume. Thus, the energy method (Equations (1.11) and (1.12)) can be applied to nonequilibrium process of viscous sintering in the final stage, where closed pores with different sizes are dispersed randomly in a viscous material.

1.4 Three-dimensional visualization of sintering

The microstructural evolution during sintering has been usually observed by 2D imaging techniques such as SEM and optical microscopy. Although the quantitative microscopy provides geometric quantities from the 2D images, the understanding of complicate 3D microstructure was difficult.

Recent advances in X-ray microtomography enable us to observe the internal structures of the actual sample by three-dimensional (3D) visualization. Here, X-ray microtomography uses X-ray beam to create (2D) cross sectional image of the object that can be used to reconstruct a 3D model (Fig.1.8). FIB-SEM tomography is also known as a micrometer or nanometer scale imaging technique which combines a focused ion beam (FIB) with a scanning electron microscope to obtain information on the internal structure of specimen.[27] Although FIB-SEM tomography provides the high resolution image, we cannot observe the same positon during the microstructural evolution, because it is destructive technique. By contrast, X-ray microtomography is the non-destructive technique and it overcomes the limitations of 2D imaging techniques, like SEM and optical microscopy. The direct measurement of a 3D structure, which is now readily available from X-ray microtomography, provides a basis for the statistical analysis of microstructural characteristics, such as relative density ρ, specific surface area S_V, surface curvature κ, particle size r, neck radius c [28,29], coordination number Z[29], heterogeneous particle displacement[30,31], particle rotation[32], pore orientation[33], pore coarsening[34,35], grain growth[36], and microstructural anisotropy[37]. The knowledge of microstructure obtained from X-ray microtomography is the first step to understand the realistic property-microstructure relationship during sintering. Since 2000s, 3D microstructural evolution in sintering of

metal particles[38] was observed by synchrotron X-ray microtomography. Figure 1.9[28] is the example of the viscous sintering of glass particles observed by synchrotron X-ray microtomography. Fig. 1.9(a) shows the particle packing, and the Fig. 1.5(b) shows the spaces between particles, that is pore or void space. Actually, the local particle arrangements and inhomogeneity at the particle scale during sintering are revealed by X-ray microtomography.[28, 38] For example, Wakai and Guillon[26] showed the pore space evolution in viscous sintering of spherical glass particles in Figure 1.10. Here, we note that the 3D pore space evolution during sintering is far more complicated than the simplified model shown in Figure 1.3. This limits the applicability of classical models in real situations. Therefore, it is expected that the analysis of 3D microstructural evolution by using X-ray microtomography provides new insights beyond the classical models.

1.5 Objective of this research

The purpose of this study is to construct the experimental and theoretical methods to estimate sintering parameters, such as sintering stress and bulk viscosity, which are fundamental quantities for predicting the macroscopic shrinkage behavior in sintering, from 3D visualization of microstructures observed by X-ray microtomography. Glass was chosen as a model material, because the mechanism of material transport during sintering of glass is much simpler than that of crystalline particle, and hence, we only consider about viscous flow mechanism. In this research, I propose the speedy and reliable method of predicting the sintering stress and bulk viscosity. Finally, I believe the application of the new research methods and theory developed through this work will be related to the innovative materials developments in ceramic fields.

1.6 Abstract of doctoral dissertation

This doctoral dissertation was divided into 6 chapters, and abstract of each chapter was described as below;

Chapter 2[39]: Sintering is a common process during which nanoparticles and microparticles are bonded, leading to the shrinkage of interstitial pore space. Understanding morphological evolution during sintering is a challenge, because pore structures are elusive and very complex. A topological model of sintering is presented here, providing insight for understanding 3-D microstructures observed by X-ray microtomography. I find that the topological evolution is described by Euler characteristics as a function of relative density. The result is general, and applicable not only to viscous sintering of glasses but also to sintering of crystalline particles. It provides criteria to distinguish the stages of sintering, and the foundations to identify the range of applicability of the methods for determining the thermodynamic driving force of sintering.

Chapter 3[40]: Sintering stress and bulk viscosity were derived as functions of relative density from microtomographic images in viscous sintering of glass particles. Three methods were proposed to estimate the sintering stress from relative density, specific surface area, and average of curvature on pore surface, which were directly measured by X−ray microtomography. The surface energy method gave valid value in the final stage of sintering, while the mixed method gave better estimation in the intermediate stage. For the initial stage of sintering, the sintering stress was calculated from the average contact radius and the average coordination number observed by X‐ray microtomography. The sintering stress at the final stage increased in free sintering,

but it decreased in constrained sintering due to pore coarsening. The bulk viscosity was calculated from the shrinkage rate and the sintering stress.

Chapter 4[41]: The macroscopic sintering parameters, sintering stress, bulk viscosity, and shear viscosity, were measured by the discontinuous sinter forging experiment for viscous sintering of calcium aluminosilicate (CAS) glass. The calculated results were compared with experimental values from the microstructural evolution during viscous sintering of spherical soda lime glass particles by X-ray microtomography. The sintering stress of CAS glass normalized by surface energy and the initial particle size was in good agreement with values estimated from the microtomography data of soda lime glass, despite the differences in particle shape and chemical composition. The bulk viscosity obtained by discontinuous sinter forging agreed fairly well with that estimated by X-ray microtomography observation, when they were normalized by glass viscosity.

Chapter 5[42]: The representative volume element (RVE) is a basic concept in the continuum mechanics of sintering of random heterogeneous porous materials. A quantitative determination of its size was performed by using synchrotron X-ray microtomography data of constrained sintering of thin glass film on a rigid substrate. A RVE size is associated with a property of interest; I determined it for relative density, specific surface area, and hydrostatic component of sintering stress. The RVE size was estimated to be from 11 to 17 times larger than the average initial particle size. The RVE size was associated with a given precision of the property. It depended on the volume fraction of porous structure, or, relative density, so that it varied with microstructural evolution.

Chapter 6: The conclusion of each chapter was summarized.

References

1. T. Kraft, H. Riedel, Numerical simulation of solid state sintering; model and application, J. Euro. Ceram. Soc. 24, 2, 345-361 (2004).

2. F. F. Lang. Powder processing science and technology for increased reliability. J. Am. Ceram. Soc. 72, 1, 3-15 (1989).

3. A. G. Evans, Structural reliability: A processing-dependent phenomenon, J. Am. Ceram. Soc. 65, 3, 127-137 (1982).

4. J. Frenkel, Viscous flow of crystalline bodies under the action of surface tension. J. Phys USSR 9, 385–391 (1945).

5. J. K. Mackenzie, R. Shuttleworth, A phenomenological theory of sintering. Proc. Phys. Soc. Lond. 62, 833–852 (1949).

6. G. W. Scherer, Sintering of low-density glasses: I, Theory. J. Am. Ceram. Soc. 60, 236–239 (1977).

7. W. D. Kingery, M. Berg, Study of the initial stages of sintering solids by viscous flow, evaporation-condensation, and surface-diffusion. J. Appl. Phys. 26, 1205–1212 (1955).

8. R. L. Coble. Sintering crystalline solids. I. Intermediate and final state diffusion models. J. Appl. Phys. 32, 787–792 (1961).

9. J. Frenkel. Viscous flow of crystalline bodies under the action of surface tension. J. Phys. 9, 385-391 (1945).

10. S. L. Kang. Sintering – Densification, grain growth and microstructure. 39-62 (2005).

11. F. B. Swinkels, M. F. Ashby. A second report on sintering diagrams. Acta Metall. 29, 259–281 (1981).

12. E. H. Exner, P. Bross. Material transport rate and stress distribution during grain boundary diffusion driven by surface tension. Acta Metall. 27, 1007-1012 (1979).

13. R. L. Coble. A model for boundary diffusion controlled creep in polycrystalline materials. J. Appl. Phys. 34, 1679-1682 (1963).

14. R. L. Coble. Intermediate-stage sintering: Modification and correction of a lattice-diffusion model. J. Appl. Phys. 36, 2327 (1965).

15. R. D. German, Coarsening in sintering: Grain shape distribution, grain size distribution, and grain growth kinetics in solid-pore systems. Crit. Rev. Solid State Mater. Sci. 35, 263–305 (2010).

16. I.-W. Chen, X.-H. Wang, Sintering dense nanocrystalline ceramics without final-stage grain growth. Nature 404, 168–171 (2000).

17. R. K. Bordia, G. W. Scherer. On constrained sintering – I. Constitu-tive model for a sintering body. Acta Metall. 36, 2393-2397 (1988).

18. R. M. McMeeking, L. T. Kuhn. A diffusional creep law for powdercompacts. Acta Metall Mater. 40, 961-969 (1992).

19. H. Riedel, H. Zipse, J. Svoboda. Equilibrium pore surfaces, sinter-ing stresses and constitutive equations for the intermediate andlate stages of sintering – II. Diffusional densification and creep.Acta Metall Mater. 42, 445-452 (1994).

20. G. W. Scherer., Sintering with rigid inclusions. J. Am. Ceram. Soc. 79, 719-725 (1987).

21. D. J. Green, O. Guillon, J. Rodel. Constrained sintering: A delicate balance of scales. J. Euro. Ceram. Soc. 28, 1451-1466 (2008).

22. O. Guillon, J. Rödel, R.K. Bordia, Effect of green-state processing on the sintering stress and viscosity of alumina compacts, J. Am. Ceram. Soc. 90, 1637-1640 (2007).

23. J. Svoboda, H. Riedel. H. Zipse. Equilibrium pore surfaces, sintering stress and constitutive equations for the intermediate and late stages of sintering – I. computation of equilibrium surfaces. Acta. Metall. 42, 435-443 (1994).

24. F. Wakai, Y. Shinoda, T. Akatsu. Methods to calculate sintering stress of porous materials in equilibrium. Acta. Mater. 52, 5621-5631 (2004).

25. F. Wakai. Mechanics of viscous sintering on the micro-andmacro-scale. Acta. Mater. 61, 239-247 (2013).

26. F. Wakai, O. Guillon. Evaluation of sintering stress from 3-D visualization of microstructure: case study of glass films sintered by viscous flow and imaged by x-ray microtomography. Acta. Mater. 66, 54-62 (2014).

27. G. Prieto. FIB-SEM Tomography. Encyclopedia of Membranes. Springer, Berlin, Heidelberg (2015)

28. D. Bernard, D. Gendron, J.-M. Heintz, S. Bordère, J. Etourneau. First direct 3D visualization of microstructural evolutions during sintering through X-ray computed microtomography. Acta Mater. 53, 121-128 (2005).

29. A. Vagnon, et al. 3D statistical analysis of a copper powder sintering observed in situ by synchrotron microtomography. Acta Mater. 56, 1084-1093 (2008).

30. L. Olmos, C. L. Martin, D. Bouvard, D. Bellet, M. D. Michiel, Investigation of the sintering of heterogeneous powder systems by synchrotron microtomography and discrete element simulation. J. Am. Ceram. Soc. 92, 1492-1499 (2009).

31. S. A. McDonald, P. J. Withers, Combining X-ray microtomography and three-dimensional digital volume correlation to track microstructure evolution during sintering of copper powder. J. Strain Anal. Eng. 49, 257-269 (2014).

32. R. Grupp, M. Nöthe, B. Kieback, J. Banhart, Cooperative material transport

during the early stage of sintering. Nat. Commun. 2, 298 (2011).

33. O. Lame, D. Bellet, M. D. Michiel, D. Bouvard, Bulk observation of metal powder sintering by X-ray synchrotron microtomography. Acta Mater. 52, 977-984 (2004).

34. L. Olmos, D. Bouvard, L. Salvo, D. Bellet, M. D. Michiel, Characterization of the swelling during sintering of uniaxially pressed copper powders by in situ X-ray microtomography. J. Mater. Sci. 49, 4225-4235 (2014).

35. T. Hondo, Z. Kato, K. Yasuda, F. Wakai, S. Tanaka, Coarse pore evolution in dry-pressed alumina ceramics during sintering. Adv. Powder Tech. 27, 1006-1012 (2016).

36. V. Tikare, M. Braginsky, D. Bouvard, A. Vagnon, Numerical simulation of microstructural evolution during sintering at the mesoscale in a 3D powder compact. Comp. Mater. Sci. 48, 317-325 (2010).

37. D. Bernard, O. Guillon, N. Combaret, E. Plougonve. Acta Mater. 59, 6228-6238 (2011).

38. O. Lame, D. Ballet, M. Di Michiel, D. Bouvard. Bulk observation of metal powder sintering by X-ray synchrotron microtomography. Acta. Mater. 52, 977-984 (2004).

39. G. Okuma, D. Kadowaki, T. Hondo, S. Tanaka, F. Wakai, Interface topology for distinguishing stages of sintering, Sci Rep.7, 11106 (2017).

40. G. Okuma, D. Kadowaki, T. Hondo, A. Sato, S. Tanaka, F. Wakai, Computation of Sintering Stress and Bulk Viscosity from Microtomographic Images in Viscous Sintering of Glass Particles, J. Am. Ceram Soc. 100, 867-875 (2017).

41. G. Okuma, J. Gonzalez-Julian, O. Guillon, F. Wakai, Comparison between sinter forging and X-ray microtomograhy methods for determining sintering stress and bulk

viscosity, J. Euro. Ceram. Soc. 38, 4, 2053-2058 (2018).

42. G. Okuma, D. Kadowaki, Y. Shinoda, T. Akatsu, O. Guillon and F. Wakai, Determination of the size of representative volume element for viscous sintering, J. Ceram. Soc. Japan. 124 [4], 421-425 (2016).

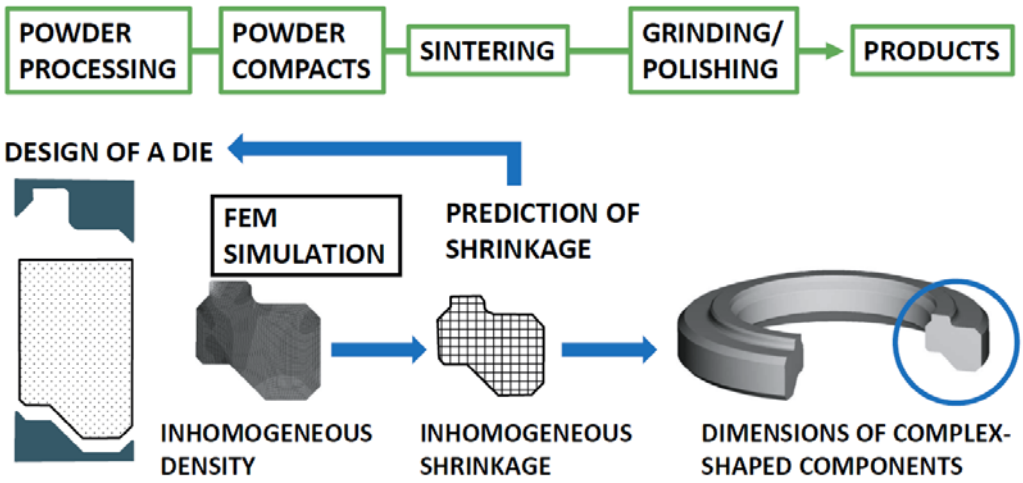

Fig.1.1. Powder processing and sintering. The continuum theory of sintering is of considerable help in predicting the dimension and shape of products or in designing industrial processes. [1]

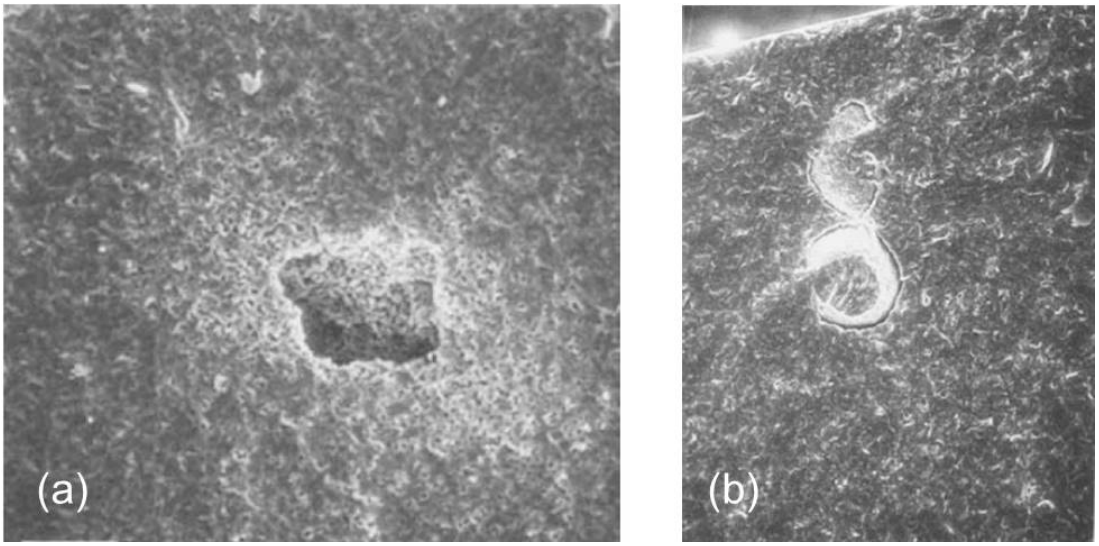

Fig.1.2. Scanning electron micrograph of (a) large void fracture (b) cracklike cavity.[3]

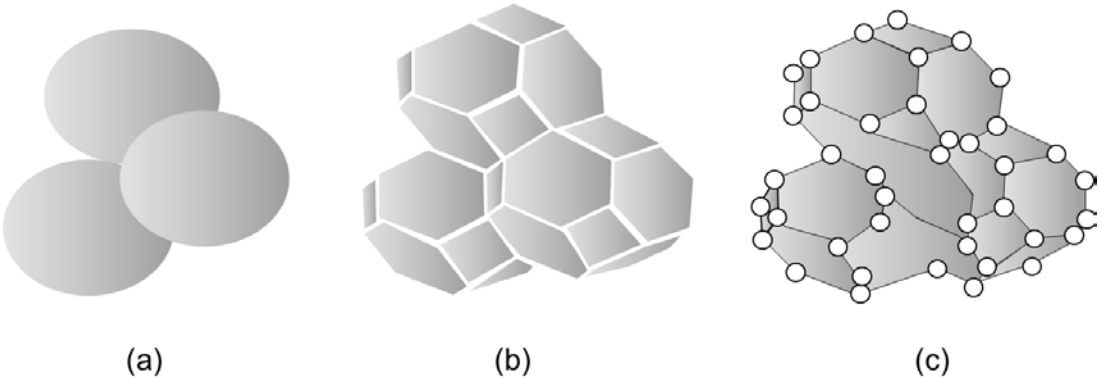

Fig.1.3. Coble's simplified geometrical model for distinguishing stages of sintering. (a) Initial stage of sintering; model structure represented by spheres in tangential contact. (b) Intermediate stage; dark grains have adopted shape of tetrakaidecahedron, enclosing white pore channels at grain edges. (c) Final stage; pores are tetrahedral inclusions at corners where four tetrakaidecahedra meet. [8]

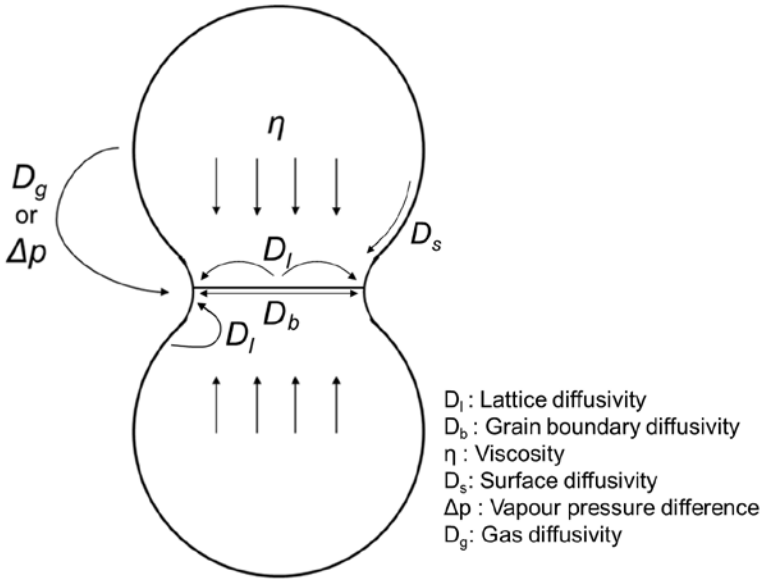

Fig.1.4. Material transport paths during initial stage of sintering.[10]

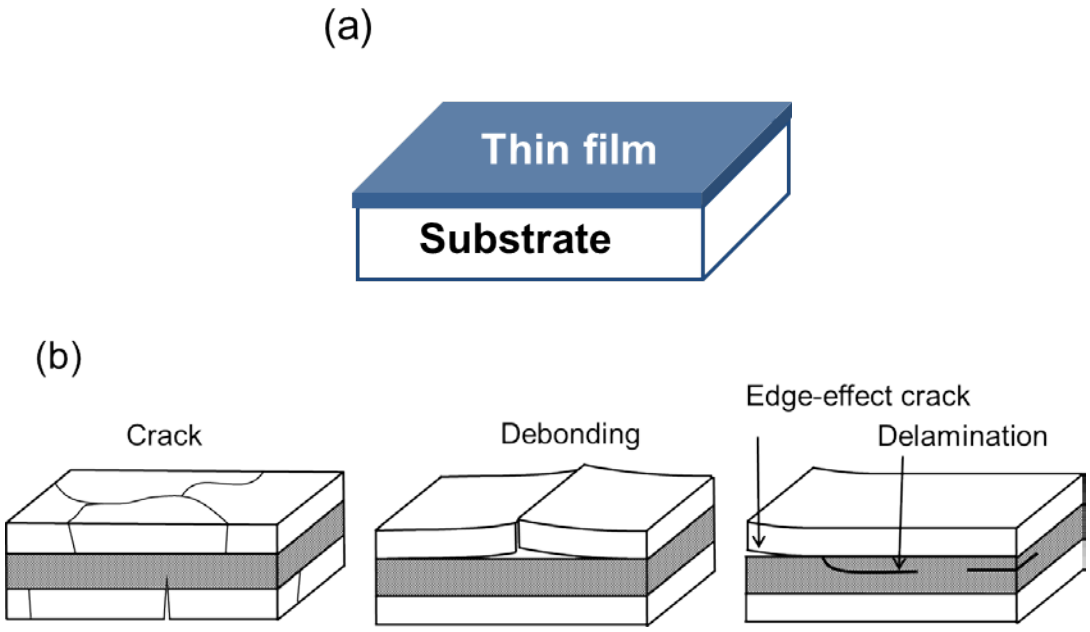

Fig.1.5. Schematic image of (a) constrained sintering, (b) co-sintering. Internal stresses induce cracks, debonding, or delamination in co-sintering.

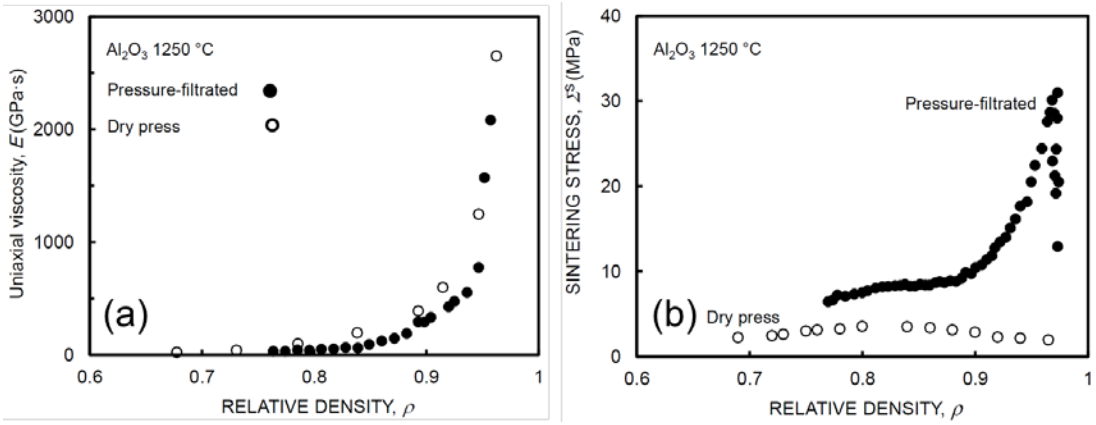

Fig.1.6. (a) Uniaxial viscosity, and (b) Sintering stress of alumina powder during sintering determined by sinter forging. [22]

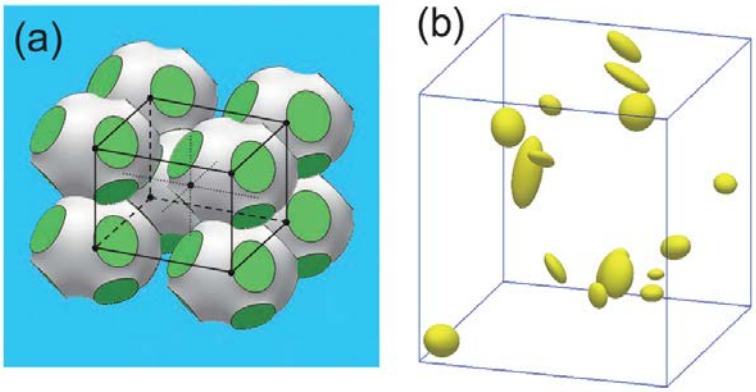

Fig.1.7. Sintering models. (a) Intermediate stage, (b) Final stage.[25]

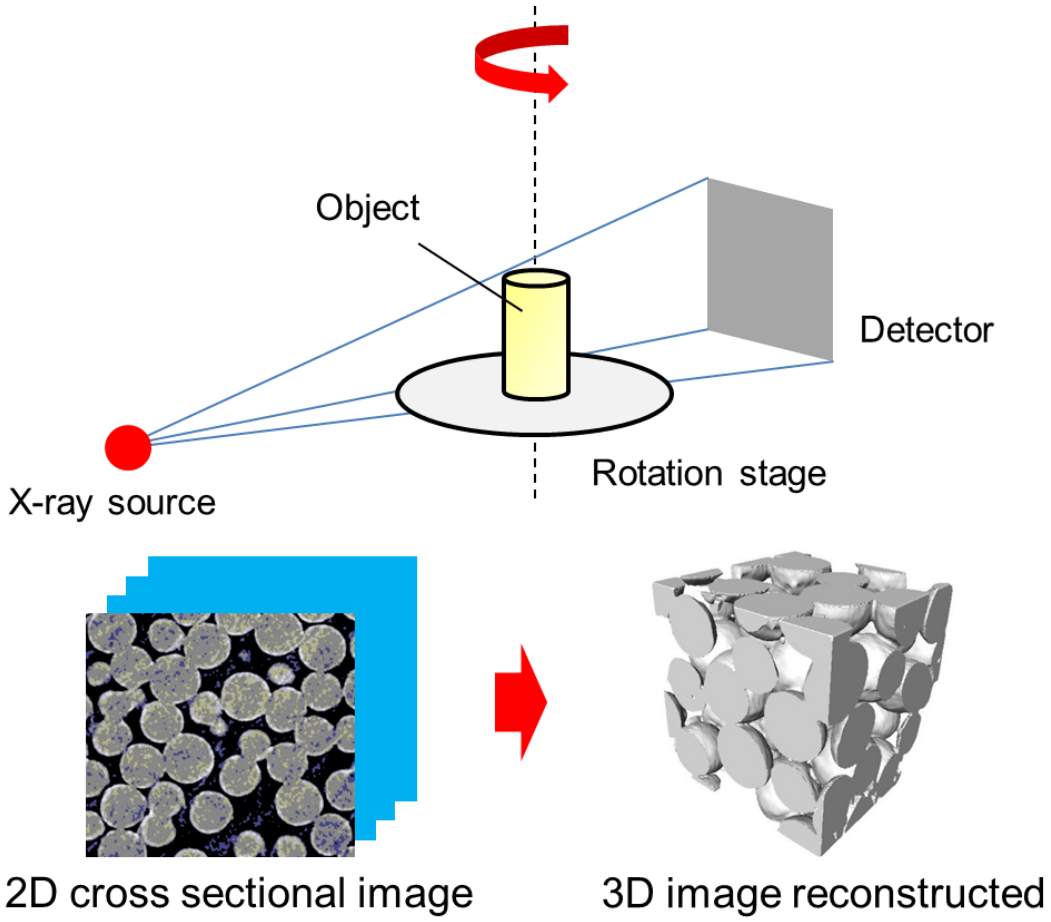

Fig.1.8. Schematic explanation of X-ray microtomography. X-ray microtomography used x-ray beam to create (2D) cross sectional image of the object that can be used to reconstruct a 3D model.

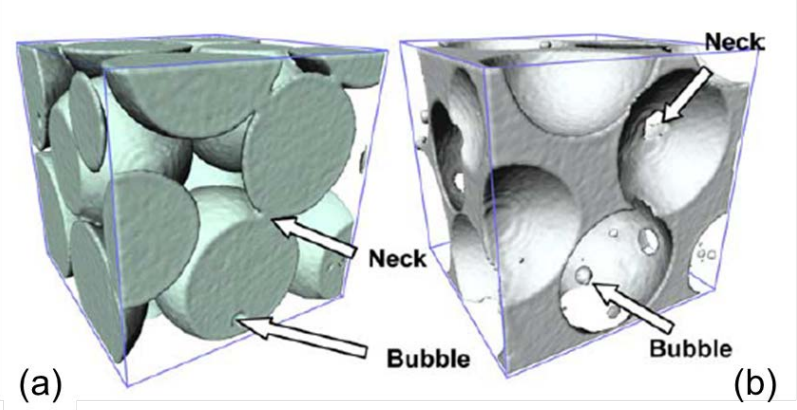

Fig.1.9. Example of viscous sintering of glass particles observed by synchrotron X-ray microtomography. (a) Solid phase, (b) Void space.[28]

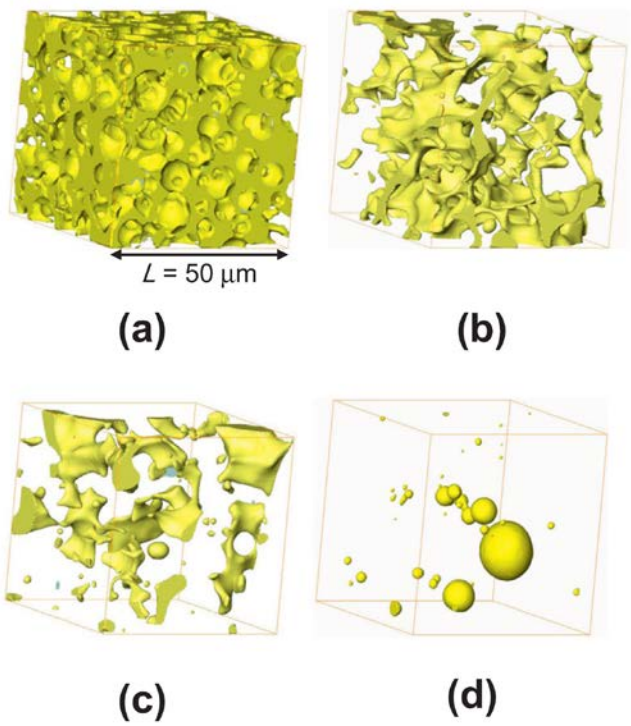

Fig.1.10. Evolution of pore space in sintering: (a) relative density, ρ = 63.5%, (b) ρ = 87.8%, (c) ρ = 94.1%, (d) ρ = 98.4%.[26]

Chapter 2 Interface topology for distinguishing stages of sintering

2.1 Introduction

As mentioned in the introduction, Coble[1] illustrated the evolution of particle-pore structure schematically in Fig. 1.3, and identified three stages of sintering. The initial stage is characterized as the formation and growth of contact between neighboring particles, where relative density increases from 0.5 to 0.6. In the intermediate stage, the pore structure evolves into an interconnected channel with cylindrical pores lying primarily along three grain edges. The final stage begins when the pinch-off of interconnected pore channel forms closed pores at the relative density of 0.9. The final stage of sintering of crystalline particles is usually accompanied by coarsening and grain growth[2,3]. Classical sintering theories, which predict the rate of density change, have been proposed with the assumption of simplified geometrical model for each stage[1,4].

However, understanding actual morphological evolution during sintering is a challenge, because pore structures are elusive and very complex, as observed in X-ray mocrotomography image (Fig. 1.10). And hence, no theoretical criterion exists for distinguishing stages of sintering by using relative density ρ and specific surface area S_V, which are metric properties and vary monotonically during sintering.

Alternatively, topological properties are required to quantify the complex microstructural changes in three stages of sintering. Rhines, DeHoff, and Aigeltinger[5,6,7] made a pioneering attempt to analyze the topological properties (e.g.,

the connectivity or genus per unit volume, and the number of pores per unit volume) by using a stereological method. But, their analysis has not been used widely in the sintering community due to the difficulty in the analysis of two dimensional cross sectional data. Here, the aim of this chapter is to obtain quantitative knowledges on topological properties, which provide insights for distinguishing stages in sintering. The microstructural evolution in sintering is an example of morphogenesis, defined as the ensemble of mechanisms responsible for the formation of patterns and shapes[8]. The observation of interface topology by X-ray microtomography affects our thinking on sintering significantly. While most of sintering studies are concerned with distinguishing matter transport mechanisms, we show that the evolution of interface topology shows remarkable similarity between viscous sintering of glass and diffusional sintering of crystalline particles.

2.2 Experimental procedure

The soda lime glass powder used in this work consisted of spherical particles (Spheriglass GB-AD, Potters Industries). It had a composition of 72.0 wt% SiO_2, 13.5 wt% Na_2O/K_2O, 9.0 wt% CaO, 3.4 wt% MgO, 2.0 wt% Al_2O_3, and 0.1 wt% Fe_2O_3. The glass spheres were sieved to obtain a homogeneous particle size distribution between 155 and 183 μm in diameter. Particle size is large because the spatial resolution of X-ray microtomography used in this work is not high. This powder was mixed with polyvinylalcohol and surfynol, and resulted in aqueous slurry (60 vol% solid content). The slurry was casted on an alumina substrate using a doctor blade with the front and rear doctor blades adjusted to a gap height of 4 and 5 mm, respectively. Tape casting speed was 10 cm/s. Drying was performed at room temperature for 72 hour. The dried green sheets were removed from the substrate and cut to the desired sample size (4.5 mm × 6.8 mm × 3.0 mm). Binder burnout and calcination were conducted by heating the sample at a rate of 3°C/min up to 450°C, and 5°C/min up to 690°C, then, held for 30 minute. The isothermal sintering treatment was performed in an external furnace, and then, taken off for microtomography measurement. This step was repeated for one sample. In each sintering step, the sample was heated at 5°C/min and held at 690°C in air with a holding time of 30 minute. The final sintering step was conducted at 700°C in air for 240 minute.

The sample was analyzed by X-ray computed microtomography (SKYSCAN 1172; Bruker, Kontich, Belgium). The X-ray source was set at a voltage of 80 kV and a current of 100 μA. The sample was rotated by steps of 0.1° until 180°. The 3D mappings with voxel size of 2.5 μm × 2.5 μm × 2.5 μm were reconstructed from the acquired data using the filtered back‐projection method. The 3D visualization and

geometrical measurements were performed using Amira (VSG, Burlington, MA) in this study. A Gaussian filtering was applied to reduce the noise in 2D images. Local thresholding method was used to segment the gray value image into pore and material, so as to determine the pore volume V_{pore}. The pore surface was discretized using triangular meshing, from which the pore area A_{pore} was calculated. The curvature on each triangle was calculated from the eigenvalues and eigenvectors of the quadratic form.

2.3 Results

2.3.1 Microstructural evolution in sintering

The viscous sintering of spherical glass particles was observed by X-ray microtomography. The microstructural evolution is illustrated in Figure 2.1. In the loose packing of particles (relative density $\rho = 64\%$, Fig. 2.1(a)), individual particles have contacts with neighbor particles, but some neighbors are not touching yet. In the pore space view (Fig. 2.1(b)), particles, which intersect with the bounding box, are seen as concave surface, where circular apertures indicate contacts with neighbor particles. For example, in sintering of a cluster of four particles (A, B, C, and D), three apertures (arrows) can be seen on the surface of particle A.

The arrangement of spherical particles reconstructed from a tomography image at $\rho = 74\%$ is illustrated in Fig. 2.2(a), and the topology of solid phase is schematically shown in Fig. 2.2(b). A point (node, vertex) represents each particle. A contact between two particles is represented by an arc (branch, edge) between the representative points. A face is defined by a polygon composed of these vertices and edges. A cell is defined by a 3-D space partitioned by these faces[9]. There is a void in each cell, from which a closed pore may be formed during sintering. The irregular bond network can be characterized by a combination of faces and partial polyhedral cells. Some local structure models depicted in Fig. 2.2(c)-(e) consist of triangular, rectangular, and pentagonal faces, respectively. There is a hole at the center of each face, then, the porous solid phase structure is a continuous network with numerous holes. In the pore space view, this structure is represented as voids inside cells which are connected by pore channels passing through faces.

The cluster of four particles (Fig. 2.2(c)) is indeed observed by X-ray microtomography (particles A, B, C, and D in Fig. 2.1(b)). As the contact radius (i.e., neck radius) grows with time, the size of a hole in the ring of three particles becomes smaller, and can be seen as a pore channel or a ligament (red arrows in Fig. 2.1(c)). The breakup of pore channel among three particles (A, B, and D) has already occurred in Fig. 2.1(c). When two remaining pore channels are pinched off, a single small closed pore is formed at the center of the tetrahedral particle cluster. But, the formed pore disappears quickly. The shrinkage of a tetrahedral pore, which is the characteristics of the “final stage” in the classical sintering model, takes place in very early stage actually.

The cross section of a pore channel is a polygon with rounded corners, where the number of edges is the number of particles surrounding the channel. For example, the pore channel outlined in red (Fig. 2.1(e)) is formed by five particles (A, E, F, G, H). The size of the pore channel decreases with densification, and becomes zero at the pinch-off finally. The initial size of a pore channel usually increases with the number of particles surrounding it. The pore channel formed by the ring of three spheres has a small initial size, and can be seen in the early stage (red arrows, Fig. 2.1(c)). But, such pore channel along three-grain junction is pinched off quickly. Large pore channels surrounded by many particles are important in the intermediate stage. An example of pore channel formed by the ring of four spheres (G, H, I, J) is seen in Fig. 2.1(e) (blue arrow). Such large pore channel remains up to the relative density of 94% before the pinch-off (Fig. 2.1(g)). When a pore channel is pinched off, one hole is closed, thereby decreasing the number of holes.

Many tetrahedral cells form small closed pores by the pinch-off of pore channels, and these small tetrahedral pores shrink and disappear quickly. The size of a cell, and its void space, usually increases with the number of particles surrounding it, or pore coordination number[10]. The closed pores larger than the particle size are formed from large voids preexisting in the random packing of particles. Such voids are connected with open pore channels initially, and are separated later through consecutive pinch-offs. Closed pores formed by viscous sintering in air become spherical (Fig. 2.1(i)), and shrink by gas diffusion in the glass. The number of spherical pores decreases to zero ultimately in the final stage of sintering.

2.3.2 Euler characteristic for describing interface topology

The naturally evolving interface changes its topology during sintering. The topological transitions are summarized as follows: (1) Formation of contacts among particles leading to the increase of number of holes *G*in the networks, (2) Pinch-off of pore channels, i.e., the decrease of *G* by the closure of holes, (3) Formation of closed pores, i.e., the increase of number of pores *N*, (4) Disappearance of closed pores, i.e., the decrease of *N*. The term “holes” is used for pore channels between porous cells throughout this paper, then, “hole closure” means the pinch-off of pore channel. The topology of a surface is characterized by its genus *g*; roughly speaking it is the number of holes in the surface. A single sphere has $g = 0$, and a torus (doughnut shape) has $g = 1$. The genus is mathematically related to the Euler characteristic as $\chi = 2 - 2g$. For partially sintered particle clusters, tetrahedron (Fig. 2.2(c)), cube (Fig. 2.2(d)), and dodecahedron (Fig. 2.2(e)), the Euler characteristic is −4, −8, and

−20, respectively. Here, we consider the half of total Euler characteristic $X/2$ as a sum of Euler characteristics of all pores

$$X/2 = \sum_{n=1}^{N} (1-g) \tag{2.1}$$

Since the sum of genus $\sum g$ is approximately equal to the total number of holes G, Eq. (2.1) becomes $X/2 \approx N - G$. The evolution of interfacial topology is, then, described by using the total Euler characteristic.

Using the Gauss-Bonnet theorem, the total Euler characteristic is calculated from the integral of Gaussian curvature $K = \kappa_1\kappa_2$ over all pore surfaces

$$X/2 = \frac{1}{4\pi}\int_A K dA \tag{2.2}$$

The normalized Euler characteristic per unit volume V is given as

$$X/2V = \bar{K}S_V/4\pi \tag{2.3}$$

where $\bar{K}$ is the average Gaussian curvature (Figure 2.3(a)), $S_V = A_{pore}/V$ is the specific surface area (Fig. 2.4), and A_{pore} is the total surface area in the unit volume. $\bar{K}$, S_V are derived from the tomography data, and plotted as functions of relative density in Fig. 2.3(a) and Fig. 2.4, respectively. $X/2V$ is calculated from these data, and is plotted as a function of relative density in Fig. 2.5(a). The unit volume V is defined as a cube with edge length $L = 20r_0$, where r_0 is the initial particle radius. Three stages of sintering can be distinguished by using Euler characteristic. In the initial stage of sintering, Euler characteristic is negative, and decreases slightly with relative density up to $\rho = 74\%$. The intermediate stage is the region where Euler characteristic increases with relative density until it has a maximum value (positive) at $\rho = 96\%$. The final stage is characterized as a region

where Euler characteristic decreases to zero ultimately. These quantitative criteria for distinguishing stages of sintering agree to the classical qualitative definition based on microstructures fairy well, as seen in Fig. 2.1).

The changes of Euler characteristic can be analyzed by comparing the number of closed pores N/V, which is plotted in Fig. 2.5(b). The increase in the number of closed pores shows that they are formed continuously during both the initial and the intermediate stages, although formation rate is limited during the initial stage ($<\rho = 74\%$). This result indicates that the slight decrease of Euler characteristic occurs because the rate of formation of holes is higher than that of hole closure in the initial stage. New holes are created as new contacts with neighbor particles are formed during densification. At the beginning of intermediate stage the increase of Euler characteristic occurs due to hole closures. The rate of hole closure decreases with densification, while the number of closed pores increases. The maximum Euler characteristic at $\rho = 96\%$ is almost the same with the number of closed pores. The ratio of open porosity to total porosity ($1-\rho$) is also plotted in Fig. 2.5(b). The ratio of open porosity decreases significantly as large closed pores are formed. In the final stage of sintering, the Euler characteristic decreases as the number of closed pores decreases.

2.3.3 Transition between different stages

The transition from the initial to the intermediate stage is related to an evolution towards a system of interconnected channels with more or less constant curvature in the conventional approach. However, the areal distribution functions of Gaussian curvature $K = \kappa_1 \kappa_2$ and mean curvature $H = (\kappa_1 + \kappa_2)/2$ (Fig.2.6) show that

the heterogeneity in curvature does not seem to be a pertinent parameter for distinguishing stages of sintering. Both mean curvature H (Fig. 2.3(b)) and Gaussian curvature K (Fig. 2.3(a)) increase with relative density monotonously, so that they do not distinguish stages. On the other hand, the transition from the initial to the intermediate stage can be distinguished clearly as an augment of the Euler characteristic.

2.4 Discussion

2.4.1 Comparison with other sintering mechanisms

Aigeltinger and DeHoff[6] analyzed the number of holes G and the number of pores N in sintering of copper particles by using quantitative microscopy. The Euler characteristic was calculated by using their data, and plotted in Fig. 2.5(a) for comparison. The Euler characteristic curves are of similar shape, when they are normalized by the average particle size. Three stages of sintering can be distinguished by using Euler characteristic not only for viscous sintering of glass but also for sintering of copper particles by diffusion.

It should be noted that sintering of amorphous and sintering of crystalline materials are rather different. The particle coarsening results from the surface motion in sintering of crystalline materials by evaporation-condensation and surface diffusion. The grain growth results from grain boundary motion by curvature. Although both coarsening and grain growth affects microstructure evolution in sintering of crystalline materials[2], such effects are not involved in viscous sintering. Nevertheless, as far as we focus on topological nature of microstructure, common features are observed for sintering of both amorphous and crystalline materials.

The effect of particle size on viscous sintering of glass particles can be predicted by using scaling law of Herring[11], thereby, we suppose the microstructure is self-similar for different particle size. In Fig. 2.4(a), the normalized $X/2V$ in viscous sintering of large glass particles ($r_0 = 80$ μm, present work) was compared with that in sintering of small glass particles ($r_0 = 4$ μm), which was observed by synchrotron X-ray microtomography[12]. Euler characteristic vs relative density curves were self-similar despite the difference in particle size.

The sintering of crystalline materials is affected significantly with the decrease of particle size into the nanometer range[13]. The particle rotation and sliding contribute to densification in the initial stage of sintering of loosely packed nanocrystalline powder[14]. Common features observed in sintering of coarse particles may not be observed in sintering of such loosely packed powder. For example, Schleef and co-workers[15] reported that Euler characteristic increased monotonically in sintering of fresh snow with relative density of 0.1. However, at present, the voxel resolution (0.28–2.5 μm) of X-ray microtomography is insufficient to study sintering of nanocrystalline particles.

2.4.2 Euler characteristic per unit volume

Consider the initial stage of sintering of identical spheres periodically arranged in a simple cubic lattice. Because there is one unique interconnected pore ($N = 1$ in Eq. (2.1)), the half of total Euler characteristic is a sum of genus made on the porous cells $X/2 = 1 - \sum g$. The periodic cubic cell structure is topologically the same with Schwartz P surface, which has the genus 3 for a unit cell (Fig. 2.7(a)). The average number of particles P in the unit volume is given as $P = 6000\rho/\pi$ where ρ is the

relative density. At $\rho = 0.6$, the normalized Euler characteristic per unit volume $X/2V$ is about −2800, which is in good agreement with experimental results in Fig. 2.5(a). The Euler characteristic per unit volume depends on the particle shape, the distribution function of particle size, and that of pore size. It is clearly shown that the number of small pores, where the pore size is normalized by the average particle radius, is larger in sintering of large particles than in the sintering of small particles (Fig. 2.8). This is partly due to the difference in relative resolution (the ratio of voxel size to the particle radius), which is 0.03 and 0.07 for the sintering of large particles (present work) and the sintering of small particles, respectively. It should be noted that Euler characteristic is sensitive to the relative resolution, because small bodies are weighted equally with large bodies.

2.4.3 Simulation of topological evolution

In order to visualize the topological evolution in sintering, we performed a computer simulation using a mathematically simple model for the case the grain boundary energy is zero, so as to compare with the microstructure evolution in viscous sintering. The computer simulation of sintering was conducted by assuming a case where the bulk diffusion is so fast that the sintering rate is controlled by the rate of creation/annihilation of vacancies on the surface[16,17].

As a mathematically simple sintering mechanism, we consider a model, where the bulk diffusion is so fast that the shrinkage rate is controlled by the interface reaction (creation and elimination of vacancies by the surface)[16]. We assume grain boundary is not the source/sink of vacancy for simplicity. Closed pores can shrink by bulk diffusion from surface to pore surface. The chemical potential in the bulk will be uniform, if the

bulk diffusion is infinitely fast. It is supposed that the interface reaction rate is proportional to the difference in chemical potential between the bulk and the surface. The surface moves inward when a vacancy is created on the pore surface. The normal velocity of surface is expressed as

$$\upsilon = M\gamma_s(\kappa - \kappa_{av}) \tag{2.4}$$

where M is the mobility, γ_s is surface energy, $\kappa = 2H$ is curvature, and κ_{av} is the average curvature. The detailed derivation of Eq. (2.4) is given in Appendix D of Ref. 38.

Brakke's Surface Evolver program[18] was used to simulate the microstructural evolution in sintering by interface-reaction controlled bulk diffusion. The outline of the program is described here briefly. Both the surface and the grain boundary of particles are represented as a set of triangular finite elements, or facets. Each facet consists of three edges and three vertices. The surface and the grain boundary have energies proportional to their area. The Surface Evolver program evolves the surface toward minimal energy by a gradient descent method under any constraint. The gradient of energy at a vertex is a force, which must be converted to a velocity vector for the motion. This conversion involves what may be called the mobility factor: how a vertex responds to the force on it. In the interface-reaction controlled sintering, the resistance of motion is actually due to the surface, not the vertex. In order to approximate this, the resistance to motion of a vertex is proportional to the area associated with vertex. The actual motion is found by multiplying the velocity by a scale factor. The physical interpretation of the scale factor is the time step. The surface motion can be approximated by enforcing the constraint on conservation of the total volume of

particles. The Surface Evolver program had been applied to simulate the interface-reaction controlled sintering[16,17], for example, evaporation-condensation, interface-reaction controlled bulk diffusion, and interface-reaction controlled surface diffusion.

The sintering of a cluster of 128 spherical particles was simulated. The result was analyzed by using the dimensionless time defined as $t^* = \gamma_s M t / r_0^2$, where r_0 is the initial radius.

Closed pores shrink by bulk diffusion from surface to pore surface[4]. Figure 2.9(a) show the evolution of pore structures in sintering of a cluster of 128 spheres. The movie clearly shows that large closed pores are formed by consecutive pinch-off of pore channels in a similar way to the microstructural evolution in viscous sintering. Figures 2.10 illustrate how a void and pore channels evolve from the topological cell of particles. Figure 2.9(b) shows the Euler characteristic varies with a dimensionless time. The Euler characteristic increased after a plateau region, reached to a maximum, and decreased toward zero. This topological feature agreed with experimental observations qualitatively, although sintering mechanisms differed with each other.

2.4.4 Topology and sintering mechanics

The sintering mechanics depends on the topology of microstructure. For the initial stage, large scale simulations of sintering of many particles have been successfully achieved by using discrete element method (DEM) recently[19,20,21]. The mechanics underlying this method is a relationship between the relative velocity of particles and the sintering force acting among neighbor particles in both sintering by

grain boundary diffusion[22,23] and in viscous sintering[24]. The macroscopic sintering stress can be estimated from the microscopic sintering force, which is a function of the average contact radius and the average particle coordination number[25]. In the final stage where closed pores are dispersed randomly, each pore has a local sintering stress[16]. For viscous sintering, the macroscopic sintering stress is defined as a volume average of local sintering stress of pores[26]. It is simply calculated from the relative density and the specific surface area[12]. The present authors have shown that sintering stress can be derived as functions of relative density directly from the knowledge of microstructure observed by X-ray microtomography[12, 25], and proposed a method to calculate the sintering stress in the intermediate state by using the average curvature of pore surface. The range in application of these three methods can be clearly defined by distinguishing stages of sintering from Euler characteristic.

2.5 Conclusions

Three stages of sintering are distinguished by using Euler characteristic, which is given as the number of closed pores minus the genus. The random packing of particles is expressed as vertices, edges, faces, and cells topologically. The genus is the number of holes, which is equivalent to the number of pore channels connecting voids inside each cell. The elementary processes in morphological transformation of pore structure is the creation and annihilation of pore channels and those of closed pores. Although the Euler characteristic vs relative density curve was studied only for viscous sintering of silicate glass particles here, I believe the result is general and may explain the sintering behavior of many ceramic and metallic particles.

These results may open the way to control internal defects formed during sintering, because it is crucial to understand the evolution of heterogeneous pore structures for improving the mechanical reliability of products. The interfacial topology provides a description of stages of sintering, and helps to recognize the roles of forces behind the microstructural evolution.

References

1. R. L. Coble, Sintering crystalline solids. I. Intermediate and final state diffusion models. J. Appl. Phys. 32, 787-792 (1961).

2. R. D. German, Coarsening in sintering: Grain shape distribution, grain size distribution, and grain growth kinetics in solid-pore systems. Crit. Rev. Solid State Mater. Sci. 35, 263-305 (2010).

3. I.-W. Chen, X.-H. Wang. Sintering dense nanocrystalline ceramics without final-stage grain growth. Nature 404, 168-171 (2000).

4. F. B. Swinkels, M. F. Ashby, A second report on sintering diagrams. Acta Metall. 29, 259-281 (1981).

5. R. T. DeHoff, K. R. Aigeltinger, K. R. Craig. Experimental determination of the topological properties of three-dimensional microstructures. J. Microscopy 95, 69-91 (1971).

6. E. H. Aigeltinger, R. T. DeHoff. Quantitative determination of topological and metric properties during sintering of copper. Metall. Trans. A 6, 1853-1862 (1975).

7. F. N. Rhines, R. T. DeHoff. Channel network decay in sintering. Mater. Sci. Res. 16, 49-61 (1984).

8. D. S. Kim, Y. J. Cha, M. H. Kim. Lavrentovich, O. D. & Yoon, D. K. Controlling Gaussian and mean curvatures at microscale by sublimation and condensation of smectic liquid crystals. Nat. Commun. 7, 10236 (2016).

9. C. Lin, M. H. Cohen. Quantitative methods for microgeometric modeling. J. Appl. Phys. 53, 4152–4165 (1982).

10. H. J. Frost. Cavities in dense random packings. Acta Metall. 30, 889–904 (1982).

11. C. Herring. Effect of change of scale on sintering phenomena. J. Appl. Phys. 53,

4152-4165 (1982).

12. F. Wakai, O. Guillon. Evaluation of sintering stress from 3-D visualization of microstructure: case study of glass films sintered by viscous flow and imaged by x-ray microtomography. Acta. Mater. 66, 54-62 (2014).

13. R. Chaim, M. Levin, A. Shlayer, C. Estournes. Sintering and densification of nanocrystalline ceramic oxide powders: a review. Adv. Appl. Ceram. 107, 159–169 (2008).

14. R. Chaim. Densification mechanisms in spark plasma sintering of nanocrystalline ceramics. Mater. Sci. Engn. A 443, 25–32 (2007).

15. S. Schleef, H. Löwe, M. Schneebeli. Influence of stress, temperature and crystal morphology on isothermal densification and specific surface area decrease of new snow. The Cryosphere 8, 1825–1838 (2014).

16. F. Wakai, T. Akatsu, Y. Shinoda. Shrinkage and disappearance of a closed pore in the sintering of particle cluster. Acta Mater. 54, 793-805 (2006).

17. F. Wakai. Modeling and simulation of elementary processes in ideal sintering. J. Am. Ceram. Soc. 89, 1471-1484 (2006).

18. K. A. Brakke. The Surface Evolver. Exp. Math. 1, 141-165 (1992).

19. F. Parhami, R. M. McMeeking. A network model for initial stage sintering. Mech. Mater. 27, 111-124 (1998).

20. A. Wonisch, et al. Stress-induced anisotropy of sintering alumina: Discrete element modelling and experiments. Acta Mater. 55, 5187-5199 (2007).

21. C. L. Martin, Z. Yan, D. Jauffres, D. Bouvard, R. K. Bordia. Sintered ceramics with controlled microstructures: numerical investigations with the Discrete Element Method. J. Ceram. Soc. Japan. 124, 340-345 (2016).

22. H. Riedel, H. Zipse, J. Svoboda. Equilibrium pore surfaces, sintering stresses and constitutive equations for the intermediate and late stages of sintering-II. Diffusion densification and creep. Acta Metall. Mater. 42, 445-452 (1994).

23. F. Wakai, K. A. Brakke, Mechanics of sintering for coupled grain boundary and surface diffusion. Acta Mater. 59, 5379-5387 (2011).

24. F. Wakai, et al. Sintering force behind the viscous sintering of two particles. Acta Mater. 109, 292-299 (2016).

25. G. Okuma, et al. Computation of sintering stress and bulk viscosity from microtomographic images in viscous sintering of glass particles. J. Am. Ceram. Soc. 100, 867-875 (2017).

26. F. Wakai. Mechanics of viscous sintering on the micro- and macro scale. Acta Mater. 61, 239-247 (2013).

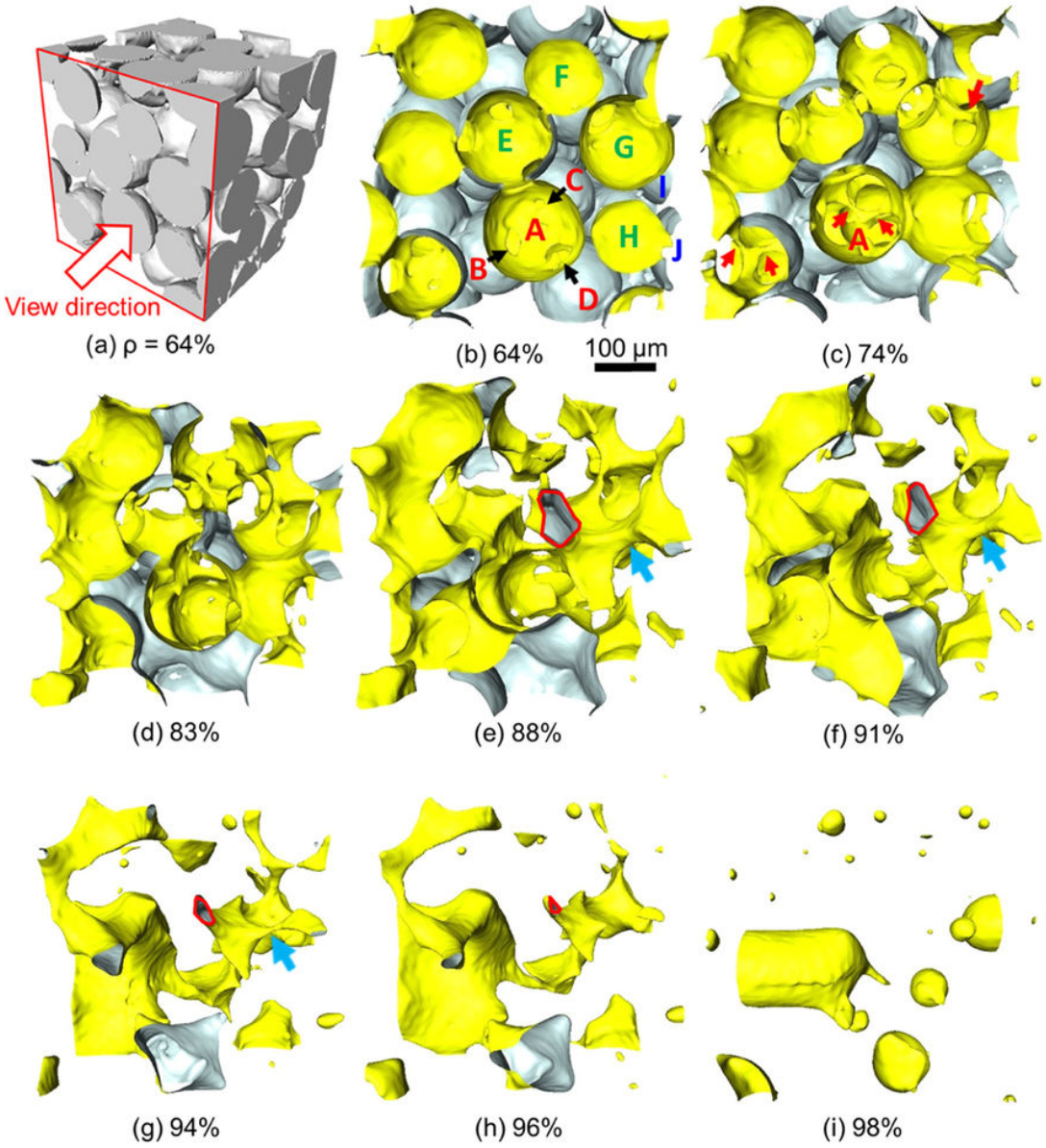

Fig.2.1. Microstructural evolution in viscous sintering of spherical glass particles. (a) solid phase at the initial relative density ρ of 64%, (b–i) pore space view as seen in the direction of arrow in (a). Particle surfaces are shown in white, while pore surfaces are shown in yellow. The size of the reconstructed subvolume is 500 × 500 × 500 μm.

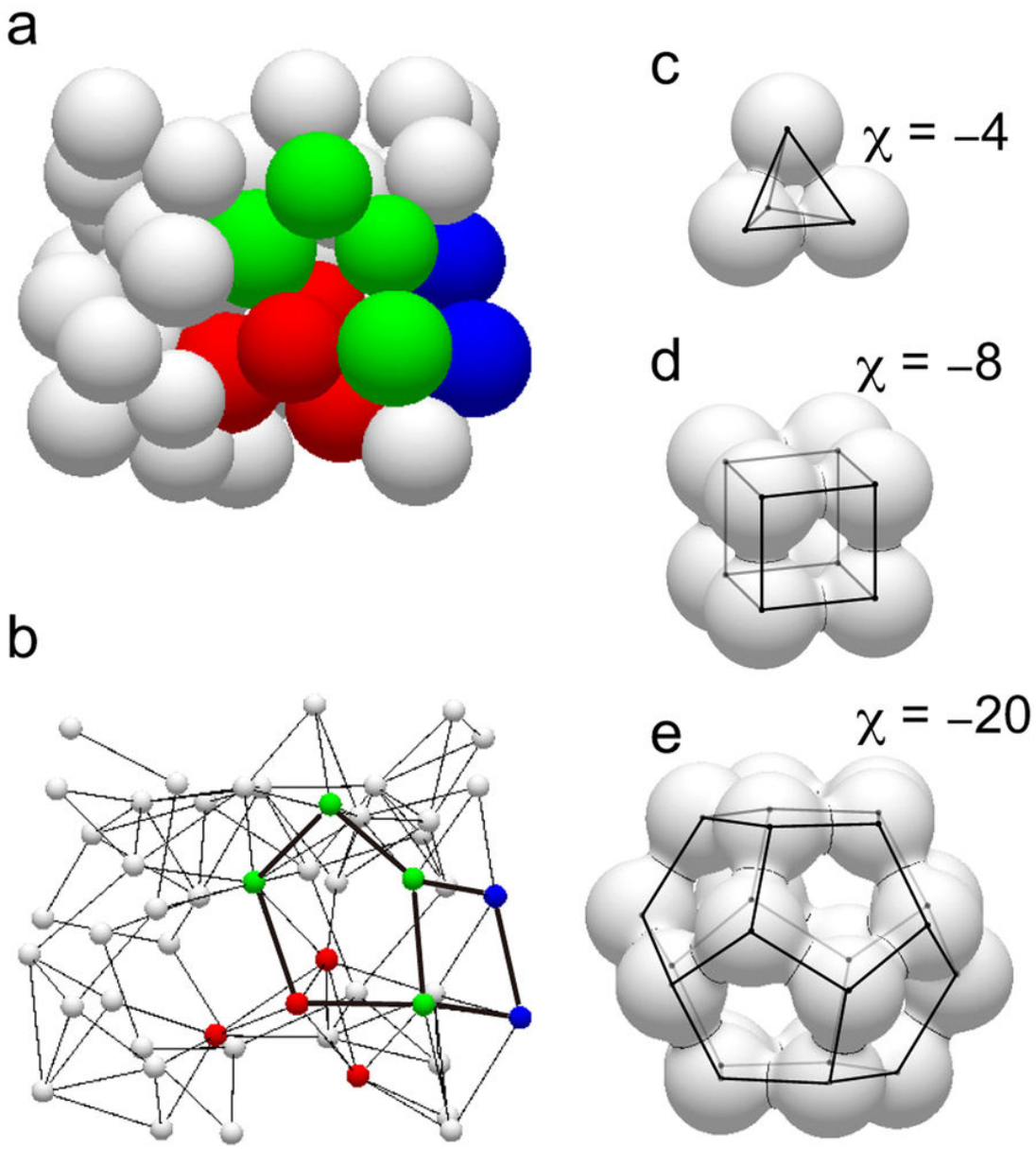

Fig.2.2. Packing model of spherical particles. (a) Sphere packing at ρ = 74%. (b) The bond network model consisting of vertices, edges, faces, and cells. A quadrilateral face and a pentagonal face are shown for example. Some polyhedral cells ((c) tetrahedron, (d) cube, and (e) dodecahedron) illustrate that voids inside cells are connected by pore channel (or hole) at the center of each face.

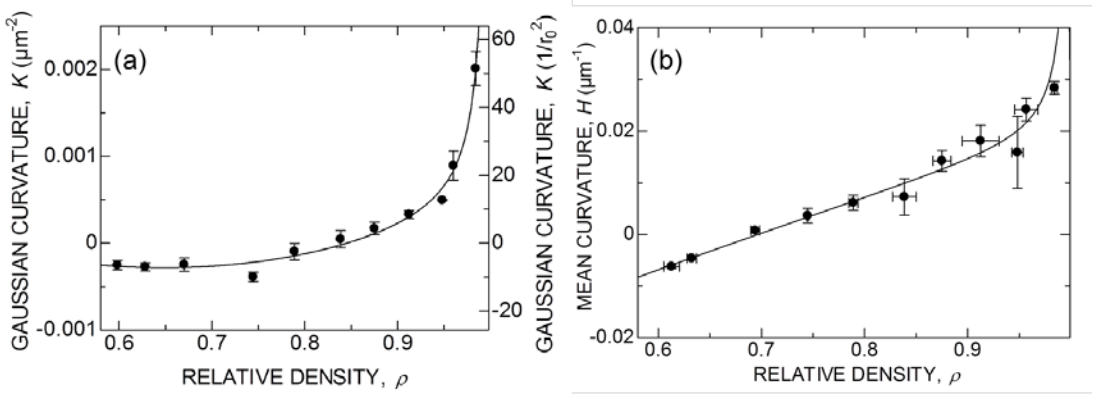

Fig.2.3. (a) Average Gaussian curvature K, (b) Mean curvature H on pore surface as a function of relative density. The local curvature on pore surface varies widely, so that we choose large volume elements with $L =$ 1.5 mm to define the average. The error bar indicates the heterogeneity inside the specimen (4.5 mm × 6.8 mm × 3.0 mm).

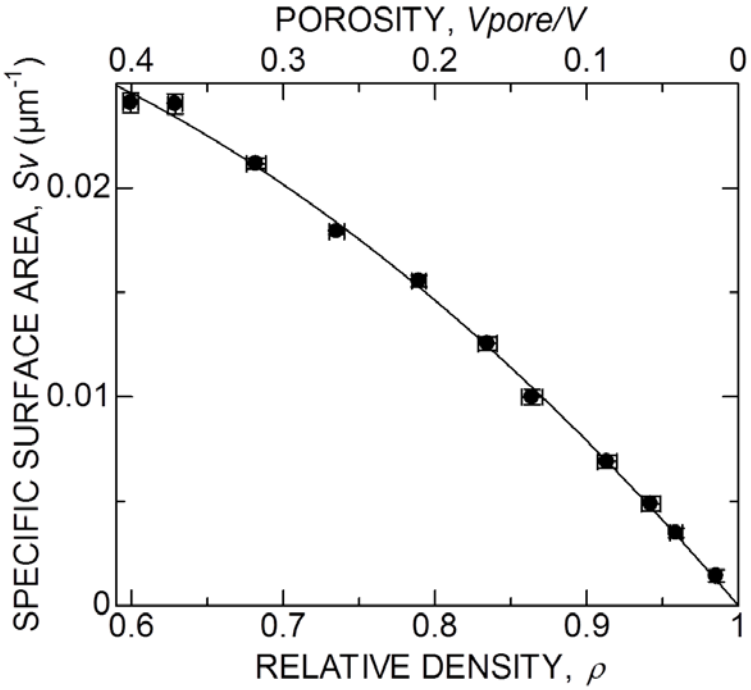

Fig.2.4. Relationship between specific surface area S_V and relative density ρ.

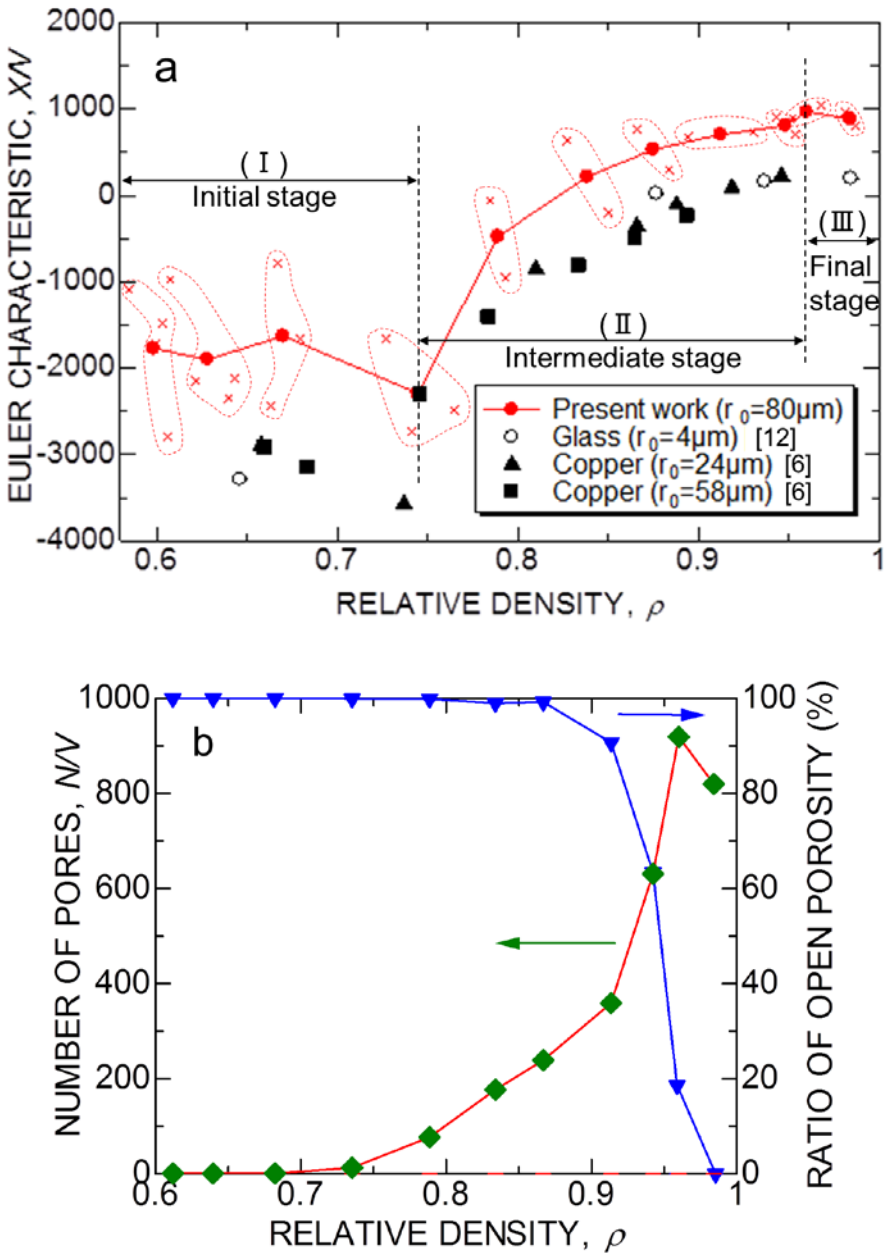

Fig.2.5. Packing model of spherical particles. (a) Sphere packing at ρ = 74%. (b) The bond network model consisting of vertices, edges, faces, and cells. A quadrilateral face and a pentagonal face are shown for example. Some polyhedral cells ((c) tetrahedron, (d) cube, and (e) dodecahedron) illustrate that voids inside cells are connected by pore channel (or hole) at the center of each face.

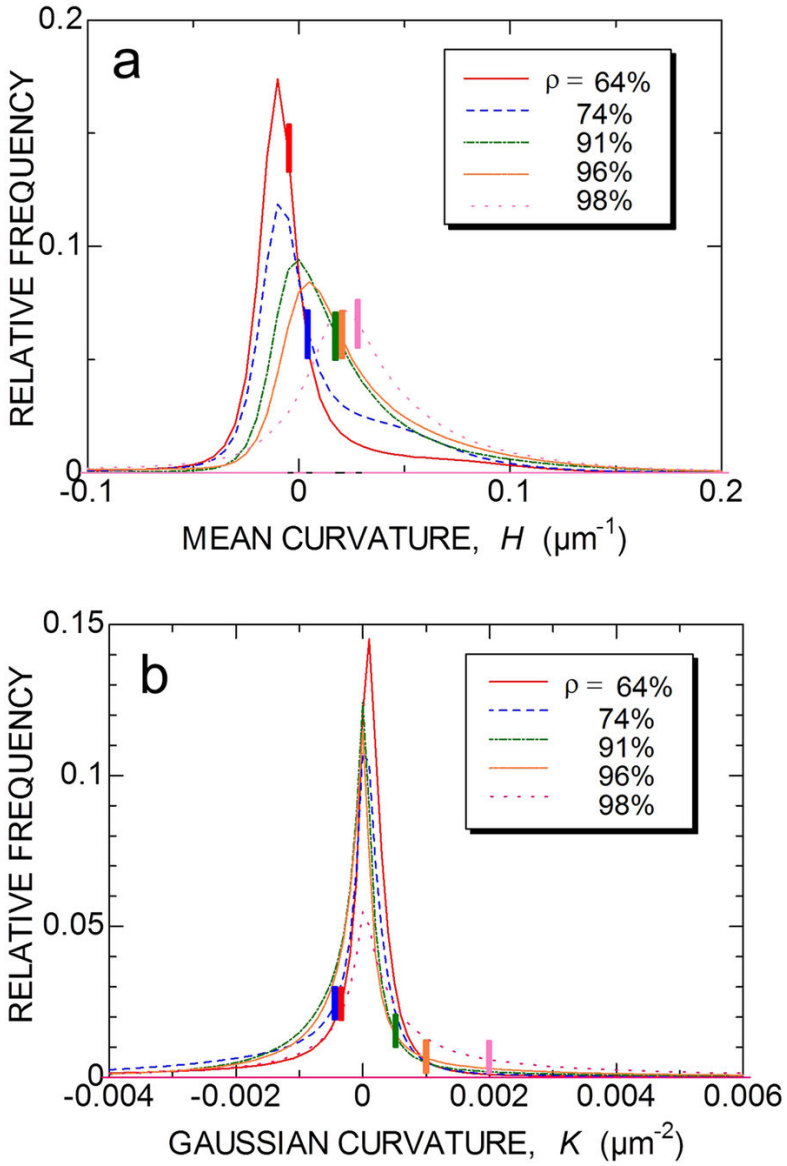

Fig.2.6. Distribution function of curvatures on pore surface. (a) Mean curvature $H = (\kappa_1 + \kappa_2)/2$, (b) Gaussian curvature $K = \kappa_1 \kappa_2$. The mean curvature is defined as positive for a spherical pore and negative for a spherical particle.

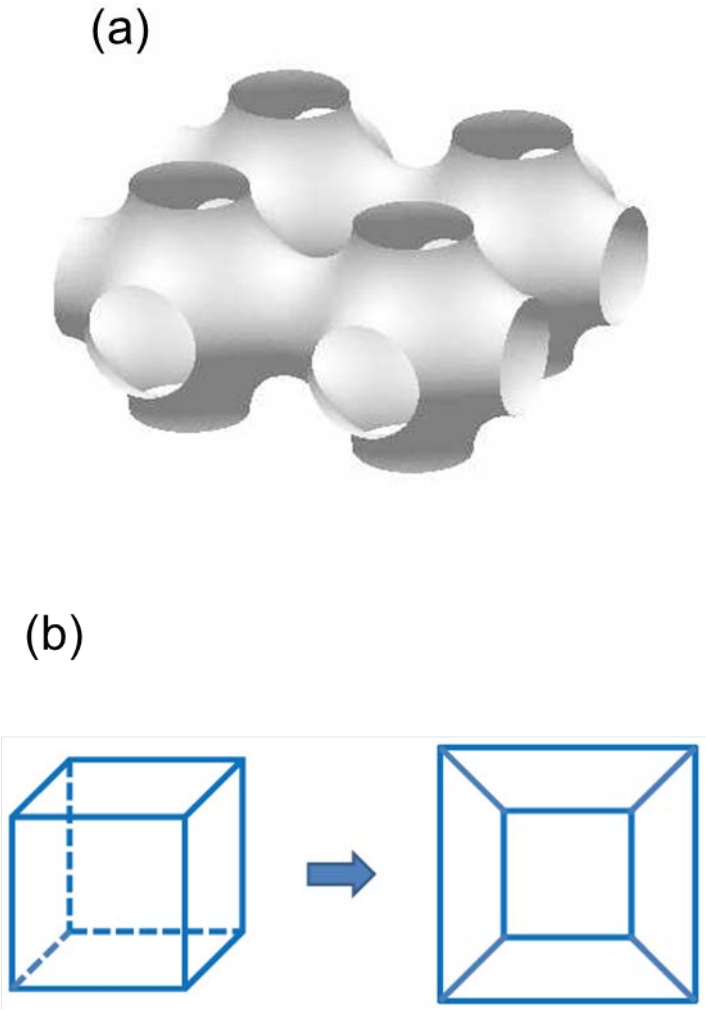

Fig.2.7. Genus of cubic structures. (a) Schwartz P surface with genus 3, (b) A cubic cluster of particles. For an isolated cluster (left model), we can stretch the top hole so that it is large enough. Then, collapse the top portion to flatten the model (right model). The number of through holes is actually five, and then the genus is 5 ($\chi = -8$ in Fig. 2 d).

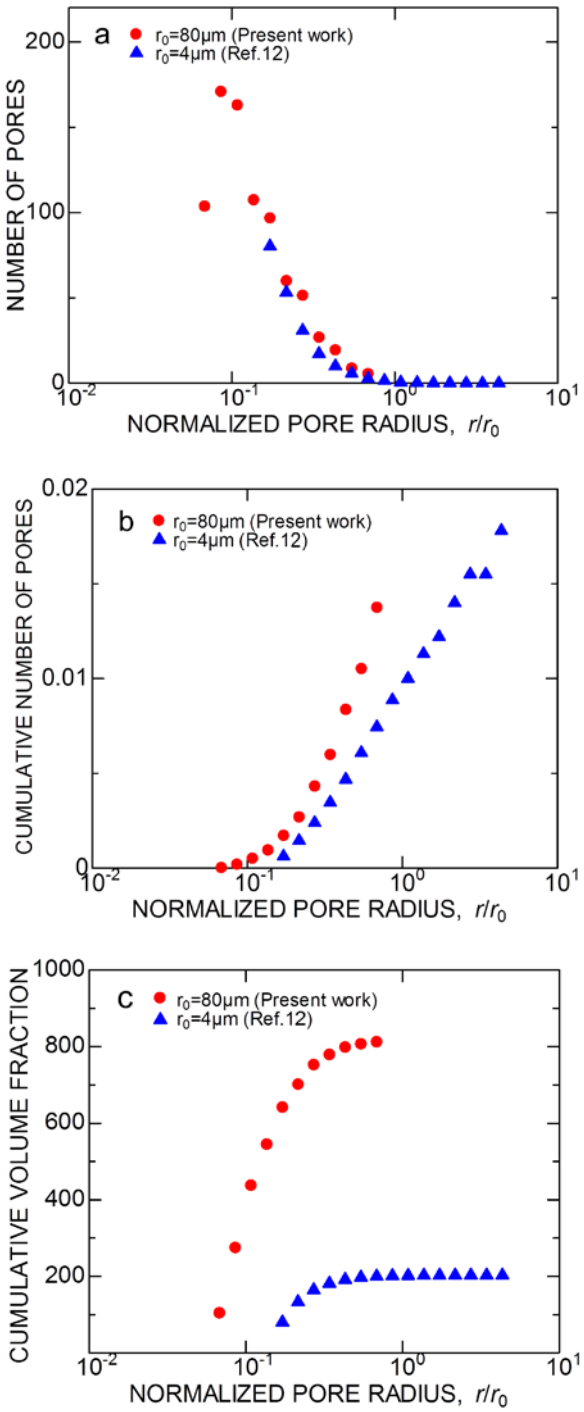

Fig.2.8. Normalized pore size distribution in the final stage of sintering. (a) The number of pores in the unit volume, (b) Cumulative number of pores, (c) Cumulative pore volume fraction.

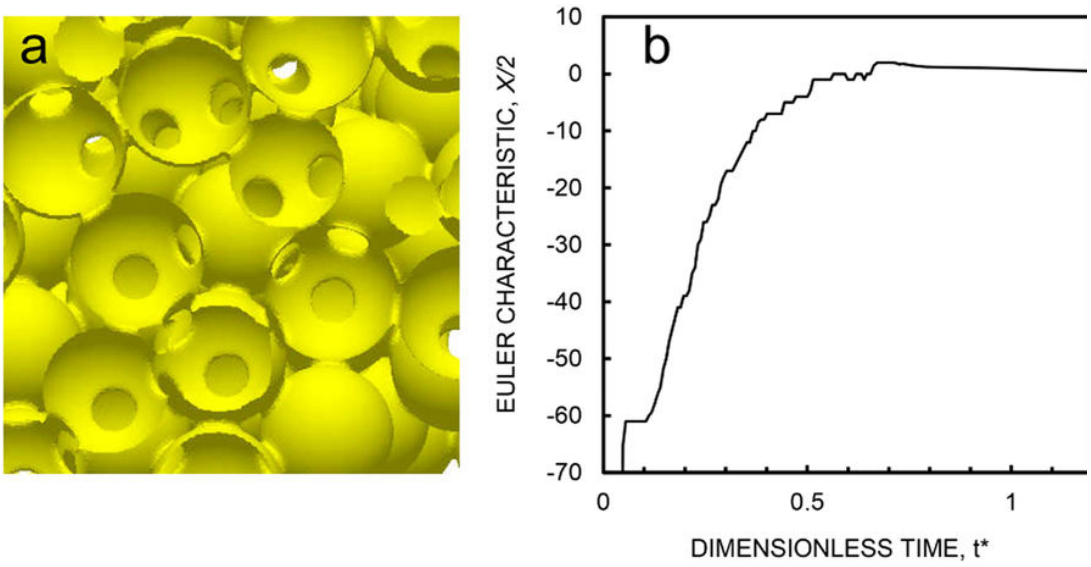

Fig.2.9. Computer simulation of sintering by bulk diffusion. (a) Snap shot at the initial stage, (b) Euler characteristic.

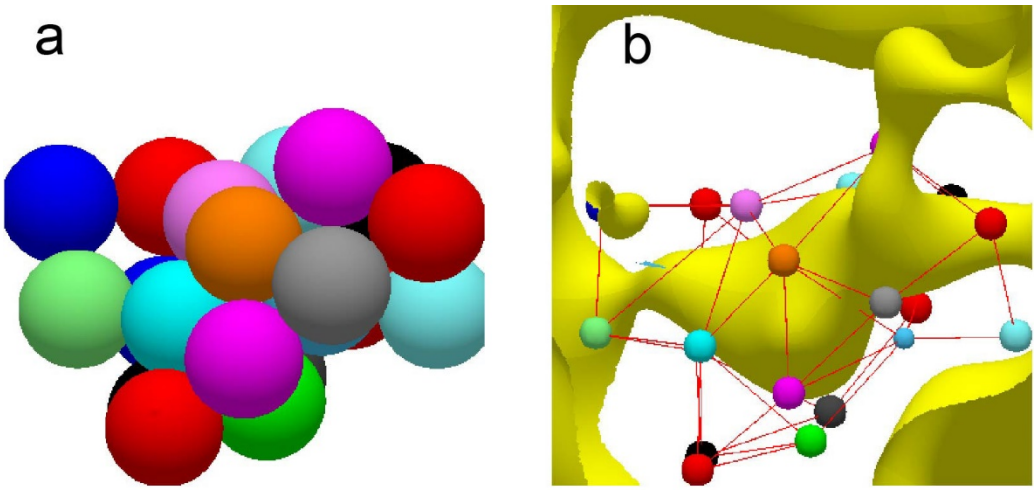

Fig.2.10. Computer simulation of sintering by bulk diffusion. (a) An example of initial particle packing, (b) A void and pore channels together with the topological cell model.

Chapter 3 Computation of sintering stress and bulk viscosity for each stage of sintering

3.1 Introduction

Although powder processing is the most efficient method to form ceramics, it is prone to heterogeneities and nonuniformity in both microscopic and macroscopic scales.[1] Inhomogeneous regions in powder compacts results in nonuniform densification rates and internal stresses, which in turn, lead to inhomogeneous shrinkage and may create defects during sintering.[2] Therefore, the mechanical reliability of products depends on microstructural evolution of heterogeneity during sintering.

The continuum mechanics fully described in section 1.3 is useful to predict the macroscopic dimensional changes, and also to analyze internal stresses generated during sintering of heterogeneous porous materials. The shrinkage rate is proportional to the sum of sintering stress and the mechanical stress, and it is inversely proportional to the bulk viscosity.[3-7] The continuum mechanics is normally concerned with the behavior of matter on a macroscopic scale that is large compared with particles. The macroscopic properties in heterogeneous materials are defined as the average over the representative volume element (RVE), which will be described in chapter chapter5.[8] This separation of scales is known as the Micro-Meso-Macro principle,[9] so that the property of RVE provides a basis for multiscale analysis.

As mentioned in section 1.4, X-ray microtomography allow us to observe three-dimensional (3D) microstructural evolution in sintering, and provide us a basis for the statistical analysis of microstructural characteristics, such as relative density ρ,

specific surface area S_V, surface curvature κ, particle size r, neck radius c, and coordination number Z. While constitutive parameters, such as sintering stress and bulk viscosity, are physical quantities that can be determined by macroscopic sinter forging experiments, they depend on the details of local particle packing, which are influenced by powder processing.[10] In this chapter 3, I describe methods to estimate constitutive parameters in the scale of RVE from 3D visualization of microstructures observed by X-ray microtomography in viscous sintering of glass particles. I present microstructural observations of 10 stages in the range of relative density from 0.6 to 0.98. This approach will be useful for understanding the relationship between microstructure and microscopic densification behavior.

3.2 Experimental procedure

Sintering of glass particles and X-ray microtomography have been fully described in chapter 2 and will be outlined here. The soda lime glass powder used in this work consisted of spherical particles (Spheriglass GB-AD, Potters Industries). It had a composition of 72.0 wt% SiO_2, 13.5 wt% Na_2O/K_2O, 9.0 wt% CaO, 3.4 wt% MgO, 2.0 wt% Al_2O_3, and 0.1 wt% Fe_2O_3. The viscosity of the glass was predicted using the multicomponent model of Fluegel[11] developed for industrial glass-forming silicate melts. The temperature dependence of viscosity μ (Pa·s) of the glass is given by the following Vogel–Fulcher–Tammann equation:

$$\log_{10}(\mu) = -2.6879 + \frac{4475.9}{T - 524.037} \tag{3.1}$$

where T stands for temperature in Kelvin. The viscosity was 3.2×10^7 Pa·s and 1.9×10^7 Pa·s at 690°C and 700°C, respectively.

The glass particles were sieved to obtain a homogeneous particle size distribution between 155 and 183 μm in diameter. We assumed the average radius of 80 μm for the polydispersed particles. This powder was mixed with polyvinylalcohol (PVA) and surfynol, and the resulted aqueous slurry (60 vol% solid content) was casted on an alumina substrate using a doctor blade. The dried green sheets were removed from the substrate and cut to the desired sample size (4.5 × 6.8 × 3.0 mm). Binder burnout and calcination were conducted by heating the sample at a rate of 3 °C/min up to 450 °C, and 5 °C/min up to 690 °C, then held for 30 minutes. The isothermal sintering treatment was performed in an external furnace, and then, taken off for microtomography measurement. This step was repeated for one sample. In each step, the sample was heated at 5 °C/min and held at 690 °C in air for 30 minutes.

3.3 Results

3.3.1 Evolution of pore morphology observed by 3D visualization

Figure 3.1 shows the evolution of pore morphology during viscous sintering, where the size of the reconstructed subvolume is 750 μm × 750 μm × 750 μm. Pore space is shown in Figure. 3.1. As mentioned in chapter 2,[12] the topology of pore structure changes drastically as the volume fraction of pore space decreases in sintering. In the initial stage (Fig 3.1(a)), spherical voids represent particles, and neck i.e. contacts between particles can be seen as circular holes. In the intermediate stages (Fig. 3.1(b)), voids are connected by pore channels. In the final stage (Fig. 3.1(c)) closed pores shrink and disappear.

3.3.2 Relative density and specific surface area

The relative density ρ and the specific surface area S_V were defined for cubic volume elements with edge length of 1000 μm, which is about 7-8 times larger than the average particle size. The average value of the sample was defined from eight nonoverlapping volume elements, then it ensures the relevant results. The average relative density is plotted as a function of sintering time in Figure 3.2, which is the sum of holding time at 690 °C. The final holding time at 700 °C, Δt (700 °C), was corrected for effective time at 690 °C using viscosity $\Delta t = \Delta t\,(700\ °C)\,\mu\,(690\ °C) / \mu\,(700\ °C)$. The densification curve obtained from microtomography resembles that for isothermal sintering. The error bar in Fig.3.2 indicates the spatial heterogeneity in density.

Specific surface area, shown in Fig. 2.4, S_V decreases with relative density. The linear relationship between S_V and relative density[14-16] has been found using stereologi-cal method, where S_V is estimated from the mean pore intercept length.[17]

Wakai[18] also reported a linear relationship in viscous sintering based on 3D observation of four stages in viscous sintering using synchrotron X-ray microtomography. However, the data in this study were best fitted by a curved line suggesting a nonlinear relationship.

3.3.3 Curvature of pore surface

The sintering of glass powder occurs by viscous flow driven by surface tension. The traction on the pore surface is proportional to local curvature, $\kappa=\kappa_1 + \kappa_2$, where κ_1 and κ_2 are two principal curvatures. In this work, the sign of curvature is defined as positive for a spherical pore and negative for a spherical particle. The local curvature on pore surface varies widely, so that we choose large volume elements with L=1500 μm to define the mean curvature H. Figure 2.3(b) shows the relationship between mean curvature $H = (\kappa_1 + \kappa_2)/2$ and relative density ρ. The error bar indicates that the local heterogeneity of H is still larger than those of relative density (Fig.3.2) and specific surface area (Fig.2.4). The average curvature is negative in the initial stage of sintering, and is close to the curvature of spherical particles. It increases with densification, as the saddle-shaped interparticle contacts grow and closed pores with positive curvatures are formed in the intermediate and the final stages of sintering.

3.3.4 Sintering stress derived from three methods

I estimated the sintering stress of nonequilibrium porous structure by substituting the average curvature $\bar{\kappa} = 2H$ into Equations (1.9) and (1.10). The values obtained by the curvature method and the mixed method are compared with that obtained by the surface energy method (Equations (1.11) and (1.12)) in Figure 3.3. Here, Σ^s is normalized by γ_S / r_0 where r_0 is the average initial particle radius. Actually, the particles are polydisperse, then, we assumed r_0 of 80 μm for convenience. The three methods gave different values of Σ^s in the initial stage; the surface energy method gave the largest value, the curvature method gave the smallest value, and the mixed method gave the intermediate value. The curvature method is not valid since it predicts negative Σ^s, which is unphysical, in the initial stage. As the relative density increases, these values increase, and coincide with each other in the final stage. The sintering stress at ρ=0.98 is estimated to be 16.2 kPa by assuming the surface energy of 0.304 J/m^2, which is measured from the surface tension at 1200°C.[19] The sintering stress was very low, simply because we used glass particles with very large size.

3.3.5 Bulk viscosity

The true strain rate $\dot{E}$ is calculated from the data of Figure 3.2, and plotted in Figure 3.4. A smooth curve is fitted to the plotted data, and the true strain rate is given as a function of relative density. The bulk viscosity was estimated using Equation (1.7) from sintering stresses determined by the energy method and the mixed method, and plotted in Figure 3.5. The bulk viscosity starts from values about 3.3×10^7 Pa・s in the initial stage and increases gradually up to relative density of 90%. The bulk viscosity increases steeply around relative density of 95% and reaches to 5.4×10^9 Pa・s.

Mackenzie and Shuttleworth[20] gave the relation between bulk viscosity and porosity in the final stage of viscous sintering by assuming spherical pores of identical size. It is written as a function of relative density:

$$K = \frac{4\mu\rho}{3(1-\rho)} \tag{3.2}$$

where μ is the viscosity of glass. Wakai[21] showed that Equation (3.2) can be applied also to closed pores with wide size distribution. The solid line in Figure 3.5 shows the theoretical prediction of bulk viscosity by assuming μ of 6.0×10^7 Pa・s. This value agree fairly well with the viscosity of the glass (3.2×10^7 Pa・s at 690 °C), which is predicted from the chemical composition.

3.4 Discussion

3.4.1 Sintering stress in the initial stage of sintering

Shrinkage in the initial stage is the result of the motion of many particles, which interact with their neighbors. The interaction between two spherical particles is the first step for understanding the mechanics of viscous sintering. The shrinkage rate between two identical particles is proportional to the sintering force, F^S, which can be approximated as a parabolic function of contact or neck radius, *c*, in the early stage $(0.1 \le c/r_0 \le 0.7)$[22]:

$$F^S = \gamma_S r_0 \left[-11.53(c/r_0)^2 + 13.58(c/r_0) + 0.40\right] \tag{3.3}$$

The microscopic sintering stress can be calculated from the sum of sintering forces acting on a single particle in the initial stage. For simplicity, consider the sintering of periodically packed monodispersed spheres with radius r_0. The coordination numbers are Z=6 for the simple cubic lattice, and Z=8 for the body-centered cubic

lattice when only nearest neighbors are in contact as shown in Figure 3.6. For the simple cubic lattice, a sphere is contained in the Wigner-Seitz cell, which is a cube bounded by six square faces with edge length of $2r_0$. Circular contacts lies on each face of the cell, then, the sintering stress in the initial stage is defined as

$$\Sigma^S = F^S / A \tag{3.4}$$

where A is the area of the face. For the body-centered cubic lattice, the sintering stress is calculated by considering an inscribed sphere in an octahedron, which is bounded by eight triangular faces with an edge length of $r_0\sqrt{6}$. The average contact radius and the average particle coordination number were directly measured by X-ray microtomography. The coordination number was measured by counting the number of contacts, which appeared as circular holes in Figure 3.1(a). The average coordination number was defined using at least 10 particles. The average contact radius was defined using all contacts on these particles. The average contact radius at ρ =0.63 and 0.68 was c=20.3 and 27.8 μm, respectively. The coordination numbers Z ranged from 6 to 8 in the initial stage. Vagnon[14] reported the average coordination number of 7.8 at ρ =0.7, and Z increased with densification. Therefore, we assumed that Z=6 is the lower bound and Z=8 is the upper bound for the initial stage. The particles are polydisperse, but the sintering force in viscous sintering of two particles of different sizes is not known yet. We estimated the range of sintering stress among polydispersed particles using Equation (3.3) as follows. For a given contact radius, the sintering force between two particles of different sizes is estimated to lie between that in sintering of two particles of minimum size (77 μm) and that in sintering of two particles of maximum size (91μm). The sintering stress is calculated by Equation (3.4) using face areas corresponding to either particles of maximum size or those of minimum size. Furthermore, the coordination

number is either Z=6 or 8. We calculated every combination of grain sizes and coordination numbers. Rectangular bars in Figure 3.3 show the range of sintering stress derived by this procedure. The sintering stress estimated from Equation (3.4) agrees with the value calculated by the mixed method fairly well. The result indicates that the surface energy method, which is valid for the final stage of sintering, cannot be applied to the initial stage. The authors conclude that the mixed method gives a better estimation of sintering stress in the initial and the intermediate stages.

3.4.2 Sintering stress in constrained sintering

The present work analyzed the microstructure of a tape in free sintering, where the sheet was sintered after it was removed from the substrate. On the other hand, Wakai and Guillon[18] studied the sintering of a sheet under constraint by a rigid substrate, and estimated deviatoric and hydrostatic components of sintering stress from the microstructural observation by synchrotron X-ray microtomography. The hydrostatic component of sintering stress in constrained sintering is calculated using the three methods, and plotted as a function of relative density in Fig. 3.7. Since they used glass particles with smaller radius (r_0 = 4μm), the sintering stress is about 20 times higher than the present work. However, the sintering stress normalized by γ_S / r_0 is comparable to the present work. The three methods gave different values of sintering stress in the initial stage of sintering (ρ = 0.635). As the relative density increased, the difference in sintering stress decreased in the intermediate stage, and all three method gave the identical value at ρ = 0.941. The sintering stress in the final stage of sintering is correctly predicted by the surface energy method from the distribution function of pore size.[21] In the final stage (ρ = 0.984), the value obtained by the surface energy method

decreased, while values obtained by the curvature method and the mixed method, which are valid only when all pores has the same size, increased. Figure 3.8 shows the distribution of normalized pore size in constrained sintering (ρ= 0.984) and free sintering (ρ= 0.98). The pore size, r, is defined as the radius of equivalent sphere, and normalized by the initial particle radius r_0. Although the number of large pore (r/r_0>1) is small, they constitute a large volume fraction. It is clearly seen that large pores are formed much more in the constrained sintering than in the free sintering. The macroscopic sintering stress of the surface energy method is defined as the volume average of local sintering stress of pores, so that it is governed by the largest pore. [21] On the other hand, the macroscopic sintering stress of the curvature method is defined as the surface average of local sintering stress of the pores. The origin of the low sintering stress by the energy method is the pore coarsening in the final stage during constrained sintering.

3.4.3 Pore coarsening in constrained sintering

Scherer[23] presented a model of pore coarsening of a viscous material under hydrostatic constraint. The smaller pores can shrink at the expense of the larger pores, so that some regions densify while others dilate. Here, we formulate pore coarsening in a viscous sheet on a rigid substrate. From the boundary condition of constraint, Bordia and Raj[24] showed that the internal in-plane stress was generated in the sheet due to the macroscopic sintering stress Σ^s:

$$\Sigma_{11} = \Sigma_{22} = \frac{6G}{3K + 4G}\Sigma^S \tag{3.5}$$

The hydrostatic component of the stress is given as follows:

$$\Sigma_m = \frac{4G}{3K + 4G}\Sigma^S \tag{3.6}$$

Since Σ^s is positive, Σ_m is positive also, then so is the tension. Each closed pore has its local sintering stress, σ^S, which is $2\gamma_S / r$ for spherical pores. From Eq. (1.4), small pores with high local sintering stress ($\sigma^S > \Sigma_m$) shrink, and large pores with low sintering stress ($\sigma^S < \Sigma_m$) increase their volume. Therefore, the initial tensile stress is responsible for pore coarsening in constrained sintering. Of course, every pore can shrink in free sintering. And pore coarsening is suppressed by the application of compressive stress ($\Sigma_m \leq 0$).

3.5 Conclusions

I have shown that both sintering stress and bulk viscosity can be derived as functions of relative density directly from microtomographic images. In the initial stage of sintering, the sintering stress is estimated from the sintering force acting among particles. The mixed method gives fairly good estimate of sintering stress in the initial and the intermediate states. The surface energy method is valid in the final stage of sintering. I have demonstrated also that the sintering stress obtained by the surface energy method depends on the pore size distribution. The decrease of sintering stress in the final stage results from pore coarsening. The sintering stress is the driving force for shrinkage, but can generate internal tensile stress when the shrinkage of the sample is constrained. The presence of internal stress is the origin of microstructural instability, so that pore coarsening occurs in the constrained sintering. Overall, we have demonstrated the feasibility of combining microtomographic images with constitutive parameters to predict the sintering behaviors of specific powder compacts. This approach can be applied to study the relationship between powder processing and sintering mechanics from the point of view of the nature of initial particle packing.

References

1. F. F. Lange. Powder processing science and technology for increased reliability. J. Am. Ceram. Soc. 72, 3-15 (1989).

2. A. G. Evans, Consideration of inhomogeneity effects in sintering. J. Am. Ceram. Soc. 65, 497-501 (1982).

3. R. K. Bordia, G. W. Scherer. On constrained sintering – I. Constitutive model for a sintering body. Acta. Metall. 36, 2393-2397 (1988).

4. R. M. McMeeking, L. T. Kuhn. A diffusional creep law for powder compacts. Acta. Metall. Mater. 40, 961-969 (1992).

5. H. Riedel, H. Zipse, Svoboda J. Equilibrium pore surfaces, sintering stresses and constitutive equations for the intermediate and late stages of sintering – II. Diffusional densification and creep. Acta. Metall. Mater. 42, 445-452 (1994).

6. E. A. Olevsky. Theory of sintering: from discrete to continuum. Mater. Sci. Engn. R. 23, 41-100 (1998).

7. T. Kraft, H. Riedel. Numerical simulation of solid state sintering; model and application. J. Eur. Ceram. Soc. 24, 345-361 (2004).

8. R. Hill. Elastic properties of reinforced solids: some theoretical principles. J. Mech. Phys. Solids. 11, 357-372 (1963).

9. Z. Hashin. Analysis of composite materials. J. Appl. Mech. 50, 481-505 (1983).

10. O. Guillon, J. Rodel, R. K. Bordia. Effect of green-state processing on the sintering stress and viscosity of alumina compacts. J. Am. Ceram. Soc. 90, 1637-1640 (2007).

11. A. Flugel. Glass viscosity calculation based on a global statistical modelling approach. Eur. J. Glass. Sci. Technol. A. 48, 13-30 (2007).

12. G. Okuma et al. Interface topology for distinguishing stages of sintering. Sci Rep, 7,

11106 (2017).

13. G. Okuma, et al. Determination of the size of representative volume element for viscous sintering. J. Ceram. Soc. Japan. 124 [4], 421-425 (2016).

14. A. Vagon, J. P. Riviere, J. M. Missiaen et al. 3D statistical analysis of a copper powder sintering observed in situ by synchrotron microtomography. Acta. Mater. 56, 1084-1093 (2008).

15. R. A. Gregg, F. N. Rhines. Surface tension and the sintering force in copper. Metall Trans. 4, 1365-1374 (1973).

16. E. H. Aigeltinger, R. T. DeHoff. Quantitative determination of topological and metric properties during sintering of copper. Metall. Trans. A. 6, 1853-1862 (1975).

17. R. T. DeHoff, F. N. Rhines. Quantitative Microscopy. New York City, New York: McGraw-Hill (1968).

18. F. Wakai, O. Guillon. Evaluation of sintering stress from 3-D visualization of microstructure: case study of glass films sintered by viscous flow and imaged by X-ray microtomography. Acta. Mater. 66, 54-62 (2014).

19. A. E. Badger, C. W. Parmelee, A. E. Williams. Surface tension of various molten glasses. J. Am. Ceram. Soc. 20, 325-379 (1937).

20. J. K. Mackenzie, R. Shuttleworth. A phenomenological theory of sintering. Proc Phys Soc London. 62, 833-852 (1949).

21. F. Wakai. Mechanics of viscous sintering on the micro-andmacro-scale. Acta. Mater. 61, 239-247 (2013).

22. F. Wakai et al. Sintering force behind the viscous sintering of two particles. Acta Mater. 109. 292-299 (2016).

23. G. W. Scherer. Coarsening in a viscous matrix. J. Am. Ceram. Soc. 81, 49-54

(1998).

24. R. K. Bordia, R. Raj. Sintering behavior of ceramic films constrained by a rigid substrate. J. Am. Ceram. Soc. 68, 287-292 (1985).

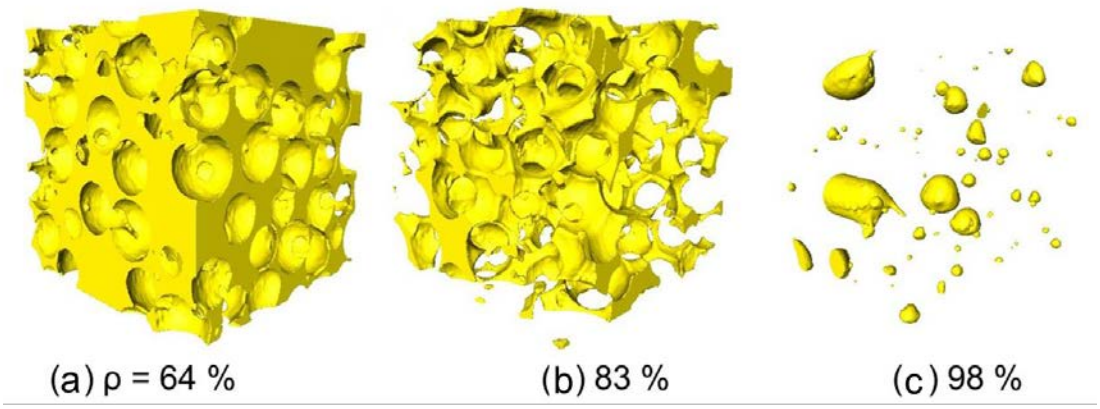

Fig.3.1. Evolution of pore space in viscous sintering and the change in pore morphology: (a) Initial stage (relative density, ρ=64%); (b) Intermediate stage (ρ=83%); (c) Final stage (ρ=98%)

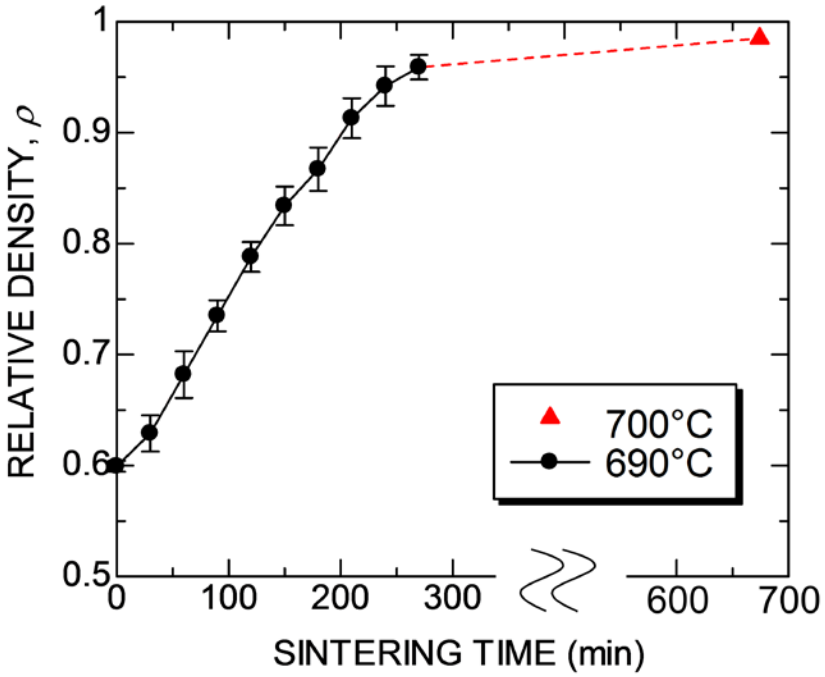

Fig.3.2 Densification curve obtained from the analysis of microtomography. The sintering time is defined as a sum of holding time at 690°C. The final holding time at 700°C (▲) was corrected for effective time at 690°C.

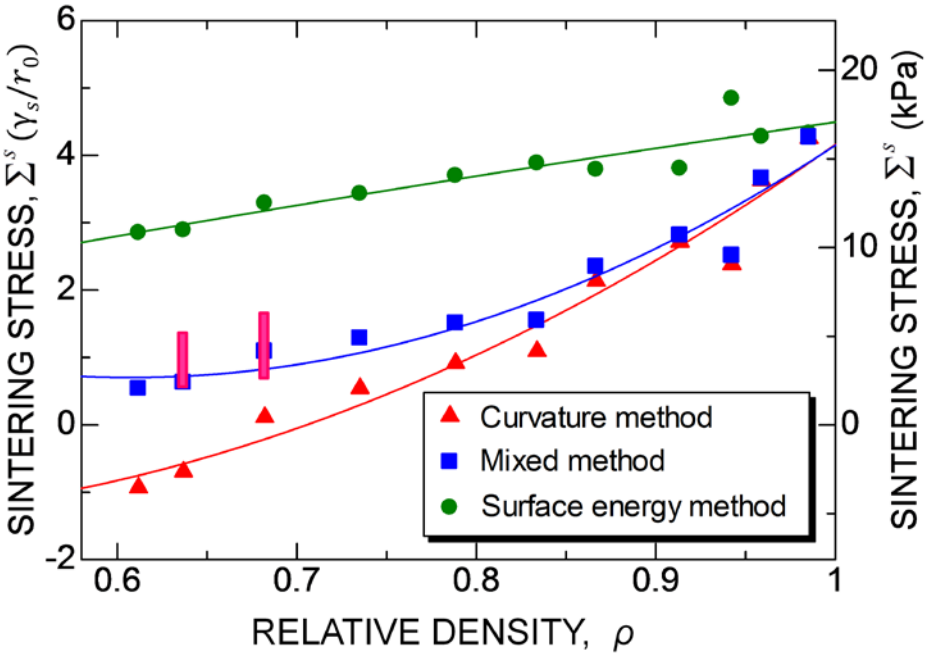

Fig.3.3. Relationship between sintering stress and relative density ρ. Sintering stress Σ^s by curvature method (▲); Σ^s by the mixed method (■); Σ^s by the surface energy method (●). Rectangular bars show the range of Σ^s estimated from the average contact radius and the average coordination numbers.

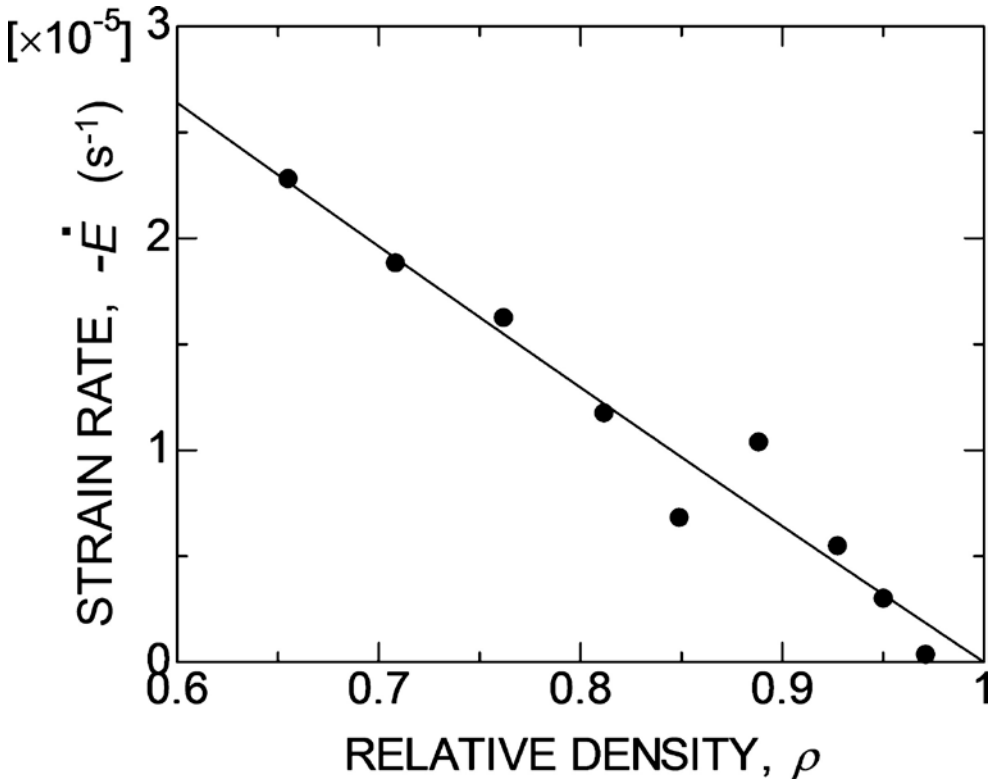

Fig.3.4. Relationship between strain rate and relative density ρ. Strain rate was estimated from the analysis of microtomography.

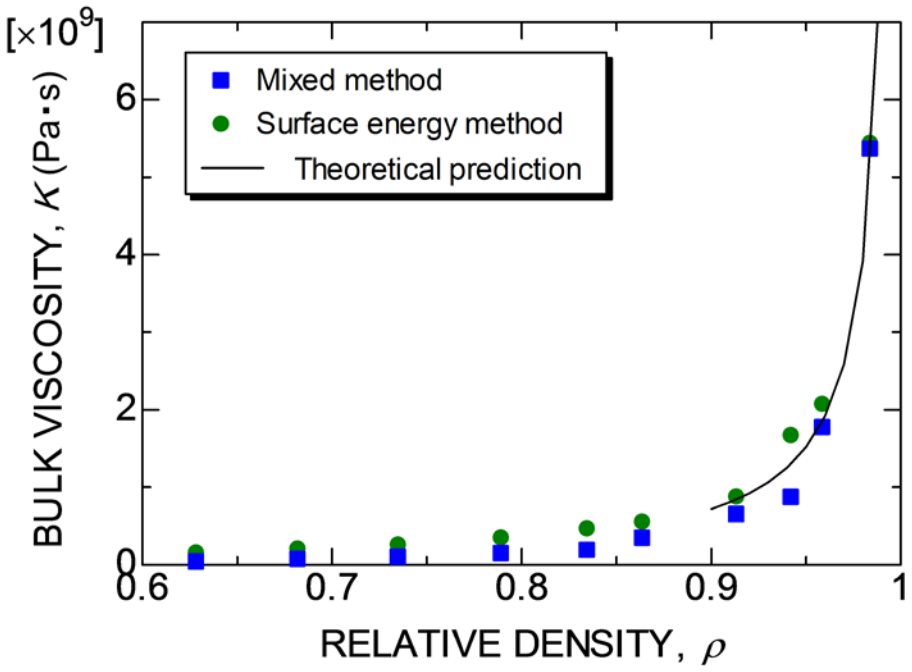

Fig.3.5. Relationship between bulk viscosity K and relative density ρ. Bulk viscosities were calculated from Equation (3.2) using estimated sintering stress.

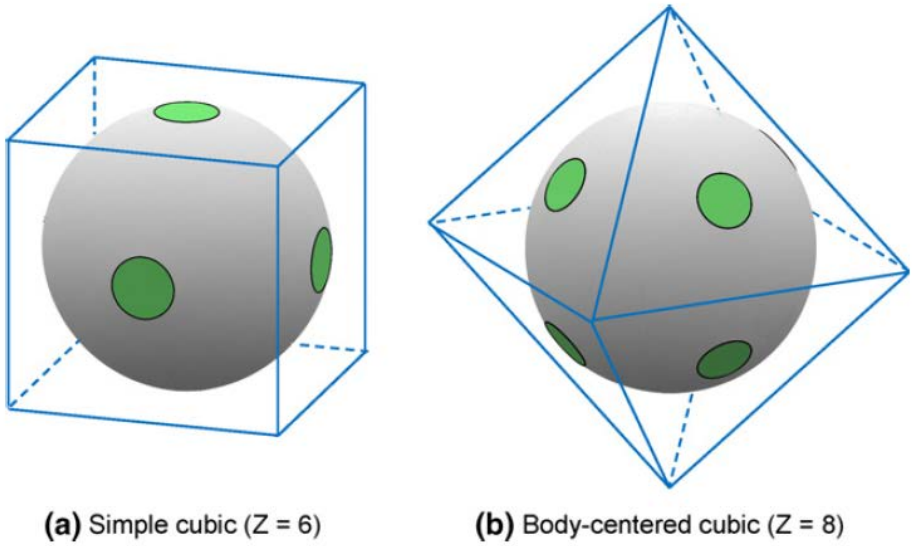

Fig. 3.6. Local coordination structure in sintering of periodically packed monodispersed particles. (a) the simple cubic lattice (Z=6), (b) the body centered cubic lattice (Z=8).

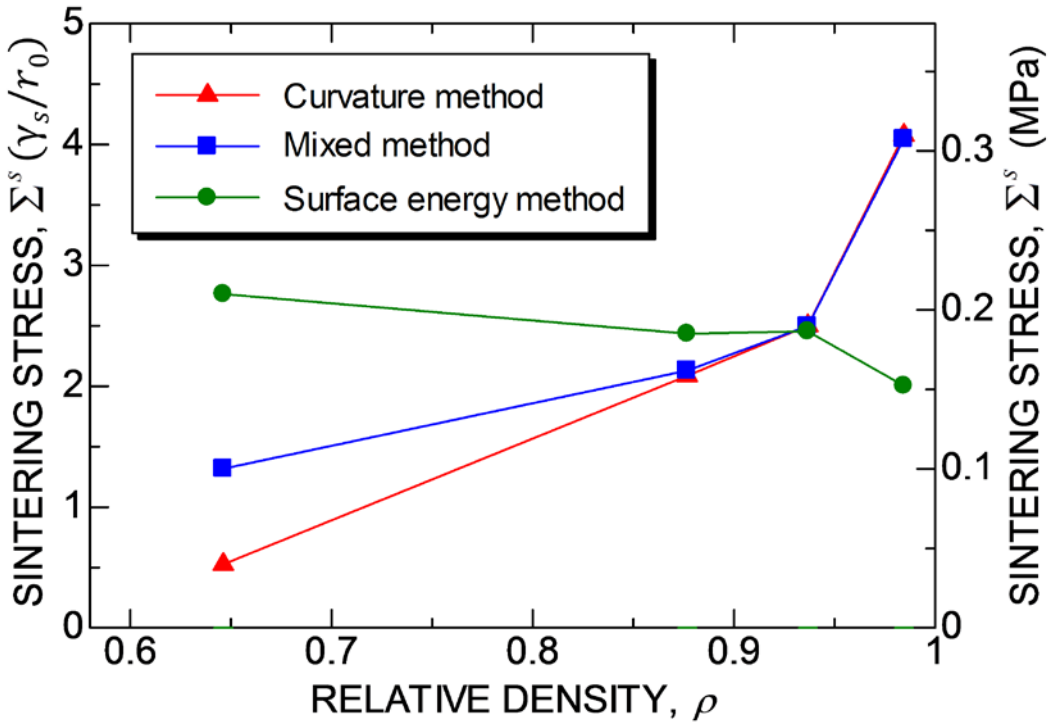

Fig.3.7. Relationship between sintering stress and relative density ρ in constrained sintering. [18] Sintering stress Σ^s by the mixed method (■): Σ^s by the surface energy method (●).

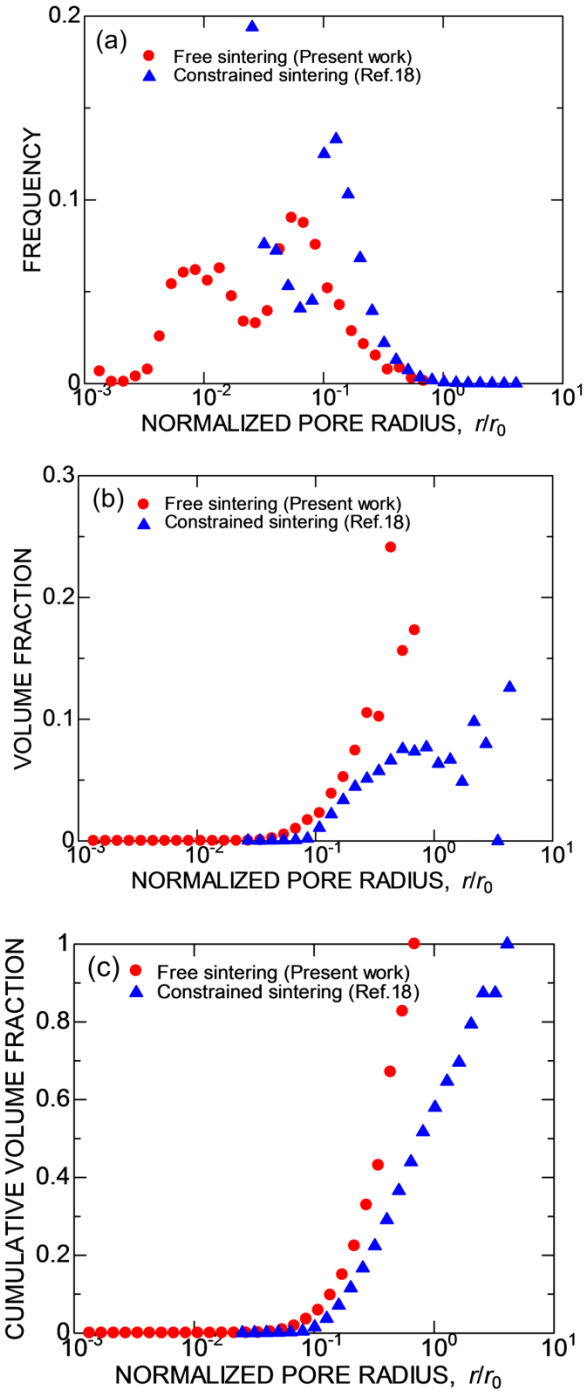

Fig.3.8. Normalized pore size distribution in the final stage of sintering (Free sintering (● Present work); Constrained sintering (▲ Ref. [18]). (a) frequency, (b) volume fraction, and (c) cumulative volume fraction. Pore radius is normalized by the initial

Chapter 4 Experimental verification of sintering stress and bulk viscosity estimated from X-ray microtomography

4.1 Introduction

The macroscopic shrinkage in sintering is described by continuum mechanics, where the strain rate is expressed as a response to the mechanical stress and the sintering stress Σ^s as described in Eq. (1.6) in section 1.3. The continuum mechanical parameters for sintering, i.e. Σ^s, shear viscosity *G*, and bulk viscosity *K*, are not constant since they depend on the relative density of the compact. Theoretical and semi-empirical formulas have been proposed to calculate those parameters, and have been well reviewed by Olevsky[1]. However, these parameters depend on different factors, such as the nature of starting powder, powder processing, particle packing, sintering temperature, and grain growth. Thus, for accurate simulation, it is necessary to determine these parameters experimentally under different conditions of powder processing and sintering. Among several experimental methods, sinter forging [2,3] has been widely used to determine these parameters, in which strain rates are typically measured at a fixed applied stress for a specific microstructure. Zuo, Aulbach, and Rödel[4] have proposed an approach of discontinuous sinter forging (DSF) in order to accurately determine the sintering parameters, eliminating the microstructural anisotropy during forging induced by the application of uniaxial load. This method was successfully applied to the sintering of alumina powder[4,5] and a glass/ceramic composite for the low-temperature co-fired ceramics (LTCC) [6,7]. Guillon, Rödel and Bordia[8] revealed that the continuum mechanical parameters were affected by powder processing method, even when the same powder was used. Discontinuous sinter forging is an

effective approach to obtain reliable data, but it is an expensive and tedious procedure since many pre-sintered specimens are required.

The purpose of this chapter 4 is to measure Σ^s and K in viscous sintering of glass particles experimentally by macroscopic sinter forging test, and to compare with those estimated from microstructure observation by X-ray microtomography, which is obtained in chapter 3. I performed discontinuous sinter forging of calcium aluminosilicate (CAS) glass particles at different uniaxial pressures. The continuum mechanical parameters were compared with those estimated from X-ray microtomography in viscous sintering of aluminosilicate glass. I show that both methods give consistent values, when the difference in viscosity and particle size are corrected. These parameters in viscous sintering of glass will provide a basic for understanding more complex processes, such as the liquid phase sintering[9,10] and the sintering of LTCC[6,7].

4.2 Mechanics of sinter forging

The constitutive equation of sintering (Eq. (1.6)) is written in cylindrical coordinates by using uniaxial viscosity[11]:

$$\dot{\varepsilon}_z = \dot{\varepsilon}_f + \frac{1}{E}[\sigma_z - \nu\ (\sigma_r + \sigma_\theta)] \tag{4.1}$$

$$\dot{\varepsilon}_r = \dot{\varepsilon}_f + \frac{1}{E}[\sigma_r - \nu\ (\sigma_\theta + \sigma_z)] \tag{4.2}$$

where $\dot{\varepsilon}_z$ is the axial strain rate, $\dot{\varepsilon}_r$ is the radial strain rate, E is the uniaxial viscosity, and ν is the viscous Poisson's ratio. $\dot{\varepsilon}_f$ is the free strain rate, i.e. the strain rate without any external applied load, and related to the sintering stress by:

$$\dot{\varepsilon}_f = -\Sigma^s / 3K \tag{4.3}$$

During uniaxial sinter forging of a cylindrical sample under a uniaxial stress σ_z, the radial and hoop stresses should be $\sigma_r = 0$ and $\sigma_\theta = 0$. Thus, Eq. (4.3) can be simplified to:

$$\dot{\varepsilon}_z = \dot{\varepsilon}_f + \sigma_z / E \tag{4.4}$$

Experimentally, *E* is determined as the reciprocal of the slope of $\dot{\varepsilon}_z$ vs. σ_z plot in sinter forging tests using specimens previously pre-sintered to obtain a fixed relative density. The volumetric strain rate $\dot{\varepsilon}_V = 2\dot{\varepsilon}_r + \dot{\varepsilon}_z$, is equivalent to the trace of $\dot{E}_{ij}$ in Eq. (1.6):

$$\dot{\varepsilon}_V = 3\dot{\varepsilon}_f + \sigma_z / 3K \tag{4.5}$$

The bulk viscosity *K* is determined from the reciprocal of the slope of $\dot{\varepsilon}_V$ vs. σ_z plot[7]. The shear viscosity *G* and the viscous Poisson's ratio ν are calculated from *E* and *K*:

$$G = 3KE/(9K - E) \tag{4.6}$$

$$\nu = (3K - E)/6K \tag{4.7}$$

Uniaxial sintering stress σ^s is defined as the uniaxial tensile stress necessary to stop the shrinkage ($\dot{\varepsilon}_z = 0$ in Eq. (4.4)):

$$\sigma^s = -E\dot{\varepsilon}_f \tag{4.8}$$

From Eq. (4.3), Eq. (4.8), and the relation $K = E/3(1-2\nu)$, the hydrostatic sintering stress is given by:

$$\Sigma^s = 3K\sigma^s / E = \sigma^s / (1-2\nu) \tag{4.9}$$

4.3 Experimental procedure

A commercially available glass powder composed of 35 wt% CaO, 30 wt% Al_2O_3, and 35 wt% SiO_2 (calcium aluminosilicate glass designated as CAS, EG2705; Ferro Corp., Cleveland, OH) was chosen in this study. The glass had a softening point of 925 °C, annealing point of 825 °C, and a grass transition temperature of 800 °C. The density of the glass was 2.8 kg/m^3, and the mean particle size was 2.7 μm (Cumulative percentile values D10 and D90 were 1.8 and 3.8 μm, respectively). The powder was uniaxially pressed at 200 MPa to shape cylindrical green bodies with diameter of 8.06 ± 0.01 mm and height of 10.66 ± 0.14 mm. The relative density of green bodies was 56.7 ± 0.4 % (calculated from the weight, height, and diameter of the cylinders). The specimens were pre-sintered in a conventional furnace in air to achieve defined relative densities of, 68%, 74%, 82%, 90% and 95%. Final densities were also measured by the Archimedes method, and it keeps a good consistency with those calculated values.

Samples were sintered in air using a modified sinter-forging setup[12], composed of a vertical split furnace fixed on a mechanical testing machine (Model 5565; Instron Corp. Norwood, MA). The pre-sintered bodies were located at the centre of the furnace and between two alumina discs, which served as reference markers for measuring the specimen height. A minimal load of 5 N was applied during the whole thermal cycle to ensure the contact between the samples and the discs. Height and diameter of the samples were measured in-situ by a high-resolution laser scanner (162-100; BETA LaserMike, Dayton, OH) with a resolution of 0.5 μm every second. As a result, axial and radial true strains can be continuously calculated during the densification of the specimens. The temperature was controlled by a type R thermocouple in contact with the lower supporting alumina disc, and at only 4-5 mm from the sample. The specimens were heated at 30 °C/min up to 850 °C. The sinter forging tests were conducted at 5, 10, 15 and 20 N at 850 °C. The load was kept constant during the isothermal holding time.

4.4 Results

Figure 4.1 (a) shows the microstructure of a sample calcined at 850 °C for 0 min (relative density of 58 %). The large particles maintained angular shapes typical of crushed glass, meanwhile the smaller particles became spherical during pre-sintering. Spherical closed pores were formed in the final stage of sintering (Fig. 4.1 (b), relative density of 95 %). The X-ray diffraction results showed no crystalline peaks even after the sinter forging tests.

Figure 4.2 shows sintering strain curves of specimens (pre-sintered to relative density of 67 %) as a function of sintering time. The axial strain was negative (shrink) and the radial strain was positive (expand). The strain rate was defined as the slope of the curve at 250 sec after the application of load. For pre-sintered specimens with different relative densities, axial strain rate $\dot{\varepsilon}_z$ and volumetric strain rate $\dot{\varepsilon}_V$ were plotted as functions of uniaxial stress σ_z in Fig. 4.3 (a) and (b), respectively. The absolute value of free strain rate, which was estimated by extrapolation to zero stress, decreased with densification generally. However, the inspection of Fig. 4.3 (a) showed that the free strain rate at the relative density of 95 % was higher than that at relative density of 74 %. Since it is unphysical, we did not include the data at relative density of 95 % in further analysis. Assuming the linear relationship between strain rates and uniaxial stress, uniaxial viscosity E and bulk viscosity K were calculated from the slope of lines in Fig. 4.3 (a) and (b), respectively. In addition, the shear viscosity G was also calculated by Eq. (4.6). Figure 4.4 shows E , K , and G increase with relative density. K is lower than E at low density region, and becomes larger than E at high density region. G

increased with relative density in the range from $E/2$ to $E/3$. The uniaxial viscosity in viscous sintering of CAS glass at 850 °C was higher than that of LTCC at 820 °C, in which the chemical composition of the glass phase was 20.8 wt% CaO, 9.7 wt% Al_2O_3, 63.4 wt% SiO_2, and 6 wt% B_2O_3.[7] It is supposed that the low uniaxial viscosity of LTCC material arises from the difference in chemical composition of glass phase. The viscous Poisson's ratio ν was calculated by Eq. (4.7), and plotted in Fig. 4.5. Generally viscous Poisson's ratio increases with increasing relative density. The Poisson's ratio obtained in viscous sintering of glass showed the same tendency with those obtained in sintering of alumina ceramics[5]. On the other hand, the viscous Poisson's ratio of LTCC showed a quite different curve, probably due to the initial anisotropy of the LTCC tape[12].

The hydrostatic sintering stress Σ^s was calculated from the free strain rate by using Eqs. (4.8) and (4.9). We plotted sintering stress of CAS glass and LTCC[7] determined by discrete sinter forging test in Fig. 4.6 (a). The sintering stress increased with densification. While the sintering stress can reach several tens of MPa in sintering of alumina with the initial particle size of several hundred nanometers[4, 5, 8], it was less than 1 MPa in viscous sintering of glass particles with the size of a few μm.

4.5 Discussion

4.5.1 Methods to estimate sintering stress from the microstructure

As described in chapter 3, the sintering stress in viscous sintering is estimated from microstructures obtained by X-ray microtomography. The microstructure in the initial stage is characterized as the formation and growth of contact between neighboring particles, where relative density increases from 50 % to 60 %. The sintering stress is given by:

$$\Sigma^s = F^s / A \qquad \text{(Sintering force method)} \qquad (4.10)$$

where F^s is the sintering force, and A is the area of the face of Wigner-Seitz cell, which depends on the coordination number. The sintering force, F^s, acting between two identical particles can be approximated as a parabolic function of contact radius, c, in the early stage ($0.1 \le c/r_0 \le 0.7$) [14]:

$$F^s = \gamma_S r_0[-11.53(c/r_0)^2 + 13.58(c/r_0) + 0.40] \qquad (4.11)$$

In the intermediate stage of sintering, the pore structure evolves into interconnected channels where surface curvature depends on position. The sintering stress is estimated by:

$$\Sigma^s = \rho\gamma_s\bar{\kappa} + \frac{2\gamma_s A_{pore}}{3V} \qquad \text{(Mixed method)} \qquad (4.12)$$

where ρ is the relative density, γ_s is the surface energy, $\bar{\kappa}$ is the average of curvature on pore surface, and A_{pore} is the total surface area in a volume element *V*. The final stage begins when the pinch-off of interconnected pore channel forms closed pores at relative density of 90 %. The sintering stress is simply expressed by [15]:

$$\Sigma^s = \frac{2\gamma_s A_{pore}}{3V_{pore}} \qquad \text{(Energy method)} \qquad (4.13)$$

where V_{pore} is the total pore volume in the volume element.

The microstructure observation by X-ray microtomography provides the average coordination number, the average contact radius, ρ, V_{pore}, A_{pore}, and $\bar{\kappa}$ in real porous microstructure during sintering. Figure 4.6 (b) shows sintering stress estimated from X-ray microtomography observation of viscous sintering of spherical soda lime glass particles with the average particle radius of 80 μm. The glass had the composition of 72.0 wt% SiO_2, 13.5 wt% Na_2O/K_2O, 9.0 wt% CaO, 3.4 wt% MgO, and 2.0 wt% Al_2O_3, 0.1 wt% Fe_2O_3. The sintering stress Σ^s in Fig. 4.6 (b) is normalized by γ_s/r_0 where r_0 is the average initial particle radius. The estimated sintering stress was about γ_s/r_0 in the initial stage, and increased to $4\gamma_s/r_0$ in the final stage.

4.5.2 Comparison with sinter forging results

The sintering stress of CAS glass measured by discrete sinter forging was normalized by assuming r_0 = 1.35 μm and γ_s = 0.4 J m^{-2}. Here, the surface energy γ_s at 850 ºC was estimated from the surface tension at 1600 ºC (See Fig. 8 in Ref. 16) and the temperature coefficient, $d\gamma_s/dT$ [16-18]. The normalized sintering stress of CAS glass in Fig. 4.6 (b) was in fair agreement with values estimated by the mixed method from the microtomography data of soda lime glass, although the initial particle size, particle shape, and chemical composition were different.

Mackenzie and Shuttleworth gave the relation between bulk viscosity and porosity in the final stage of viscous sintering by assuming spherical pores of identical size. It is written as a function of relative density:

$$K = \frac{4\mu\rho}{3(1-\rho)} \tag{4.14}$$

where μ is the viscosity of glass. The experimental data in Fig. 4.4 was fitted by Eq. (4.14) with μ = 2.0 × 10^9 Pa·s for the CAS glass. The dashed line depicts the fitted curve. The bulk viscosity of CAS glass was normalized by μ, and K/μ was plotted as a function of relative density in Fig. 4.7. The bulk viscosity of soda lime glass was also estimated by using Eq. (4.3) from free strain rates and sintering stresses obtained by the X-ray microtomography. The bulk viscosity of soda lime glass was normalized by using μ = 6.0 × 10^7 Pa·s, and plotted in Fig. 4.7 for comparison. In the initial stage, these normalized bulk viscosity K/μ obtained by discrete sinter forging agreed fairly well with that obtained by the mixed method (X-ray microtomography). In the final stage, the difference of K/μ between the mixed method and the energy method decreased, and K/μ obtained by the discrete sinter forging agreed with the values obtained by X-ray microtomography. This experimental result supports the theoretical analysis that the bulk viscosity is proportional to the viscosity of glass, and is simply a function of relative density, independent of the distribution function of pore size [15].

4.5.3 Difference between the viscous sintering and the sintering of crystalline materials

Zuo et al. [4] reported that the sintering stress of alumina increased slightly with density, and then, decreased at the final stage of sintering as significant grain growth

took place. For a single closed pore in sintering of crystalline material, Raj[19] expressed the sintering stress as follows:

$$\Sigma^s = \gamma_s \kappa_{pore} + \alpha \frac{\gamma_{gb}}{d} \tag{4.15}$$

where κ_{pore} is the curvature of pore, γ_{gb} is the grain boundary energy, and d is the grain size. Therefore, both pore coarsening and grain growth decrease the sintering stress in the final stage. On the other hand, the sintering stress increased with decreasing pore size even at the final stage in Fig. 4.6 (a), because there is no grain growth in viscous sintering. However, it should be noted that pore coarsening can occur in constrained sintering due to tensile stress in the film. In this case, sintering stress decreases with increasing density in viscous sintering [13, 20].

4.6 Conclusions

The discontinuous sinter forging technique was applied for the experimental determination of parameters in viscous sintering of glass particles. The bulk viscosity and shear viscosity increased with increasing relative density. The sintering stress increased with relative density. The decrease of sintering stress in the final stage, which had been reported during sintering of crystalline particles, was not observed in viscous sintering. The parameters obtained by the discontinuous sinter forging were compared with those estimated from the microstructural observation by using X-ray microtomography. Even though the initial particle size and chemical composition of glass particles were different, both techniques provided consistent and reliable values when the bulk viscosity was normalized by the viscosity of glass and the sintering stress was normalized by the surface tension and the initial particle size.

Recently the vertical sintering technique was developed to measure uniaxial viscosity of thin ceramic layer[21] and LTCC[22], because sinter forging experiments are not applicable to thin layers. The knowledge of sintering stress and uniaxial viscosity are useful to analyze camber evolution and stress development in bilayer laminates[23]. The authors believe the present technique by using X-ray microtomography will be also applicable to analyze thin layers in laminates.

References

1. E.A. Olevsky, Theory of sintering: from discrete to continuum, Mater. Sci. Eng. R23, 41-100 (1998).
2. K.R. Venkatachari, R. Raj, Shear deformation and densification of powder compacts, J. Am. Ceram. Soc. 69, 499-506 (1986).
3. M.N. Rahaman, L.C. de Jonghe, G.W. Scherer, R.J. Brook, Creep and densification during sintering of glass powder compacts, J. Am. Ceram. Soc. 70, 766-774 (1987).
4. R. Zuo, R., E. Aulbach, J. Rödel, Experimental determination of sintering stresses and sintering viscosities, Acta Mater. 51 4563-4574 (2003).
5. R. Zuo, R., E. Aulbach, J. Rödel, Viscous Poisson's coefficient determined by discontinuous hot forging, J. Mater. Res. 18, 2170-2176 (2003).
6. J.B. Ollagnier, O. Guillon, J. Rödel, Viscosity of LTCC determined by discontinuous sinter-forging, Int. J. Appl. Ceram. Tech. 3 437-441 (2006).
7. J.B. Ollagnier, O. Guillon, J. Rödel, Effect of anisotropic microstructure on the viscous poperties of an LTCC Material, J. Am. Ceram. Soc. 90, 3846-3851 (2007).
8. O. Guillon, J. Rödel, R.K. Bordia, Effect of green-state processing on the sintering stress and viscosity of alumina compacts, J. Am. Ceram. Soc. 90, 1637-1640 (2007).
9. T. Ostrowski, A. Ziegler, R.K. Bordia, J. Rödel, Evolution of Young's modulus, strength, and microstructure during liquid-phase sintering, J. Am. Ceram. Soc. 81, 1852-1860 (1998).
10. J. Gonzalez-Julian, O. Guillion, Effect of electric field/current on liquid phase sintering, J. Am. Ceram. Soc. 98, 2018-2027 (2015).

11. R.K. Bordia, G.W. Scherer, On constrained sintering – II. Comparison of constitutive models, Acta Mater. 36, 2399-2409 (1988).
12. E. Aulbach, R. Zuo, J. Rödel, Laser-assisted high-resolution loading dilatometer and applications, Exp. Mech. 44, 71-75 (2004).
13. G. Okuma, D. Kadowaki, T. Hondo, A. Sato, S. Tanaka, F. Wakai, Computation of sintering stress and bulk viscosity from microtomographic images in viscous sintering of glass particles, J. Am. Ceram. Soc. 100, 867-875 (2017).
14. F. Wakai, K. Katsura, S. Kanchika, Y. Shinoda, T. Akatsu, K. Shinagawa, Sintering force behind the viscous sintering of two particles, Acta Mater. 109, 292-299 (2016).
15. F. Wakai, Mechanics of viscous sintering on the micro- and macro scale, Acta Mater. 61, 239-247 (2013).
16. D.A. Weirauch Jr, D.P. Ziegler, Surface tension of calcium aluminosilicate glass using computerized drop shape analysis, J. Am. Ceram. Soc. 79, 920-926 (1996).
17. K. Mukai, T. Ishikawa, Surface tension measurements on liquid slags in CaO-SiO_2, CaO-Al_2O_3 and CaO-Al_2O_3-SiO_2 system by a pendant drop method, J. Japan. Inst. Met. 45, 147-154 (1981).
18. L. R. Barret, A. G. Thomas, Surface tension and density measurements on molten glasses in the CaO-Al_2O_3-SiO_2 system, J. Soc. Glass Technol. 43, 179T-190T (1959).
19. R. Raj, Analysis of the sintering pressure, J. Am. Ceram. Soc. 70, C210-C211 (1987).
20. F. Wakai, O. Guillon, Evaluation of Sintering Stress from 3-D visualization of microstructure: Case study of glass films sintered by viscous flow and imaged by

X-ray microtomography, Acta Mater. 66, 54-62 (2014).

21. M. Cologna, V. M. Sglavo, Vertical sintering to measure the uniaxial viscosity of thin ceramic laryers, Acta Mater. 58, 5558-5564 (2010).
22. L. Yu, S. Qi, Z. Ma, R. Zuo, Experimental determination of the uniaxial viscosity of low-temperature co-fired ceramic tapes by vertical sintering, Ceram int. 40, 9367-9375 (2014).
23. D. W. Ni, V. Esposito, C. G. Schmidt, T. T. Molla, K. B. Andersen, A. Kaiser, S. Ramousse, N. Pryds, Camber evolution and stress development of porous ceramic bilayers during co-firing. J. Am. Ceram. Soc. 96, 972-978 (2013).

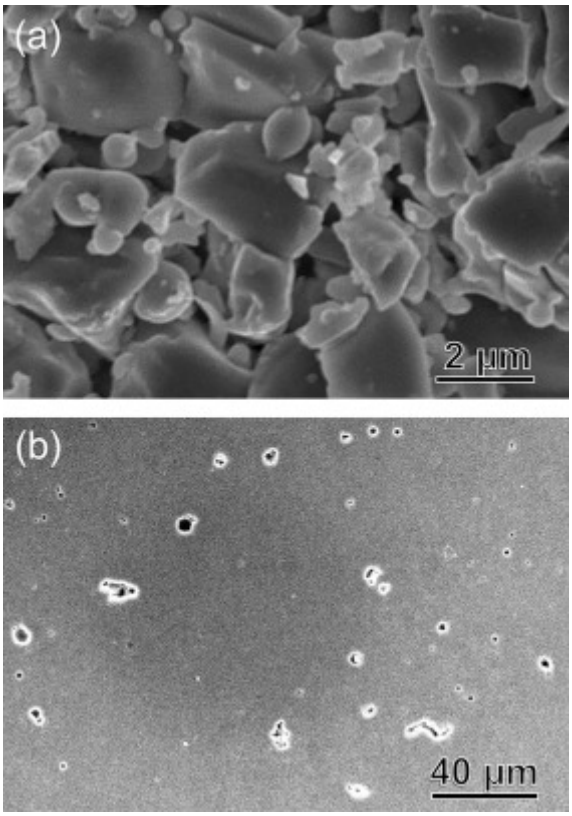

Fig.4.1. Microstructure of CAS glass sample. (a) fracture surface of a calcined specimen (relative density of 58%), (b) polished surface of a specimen pre-sintered to relative density of 95%.

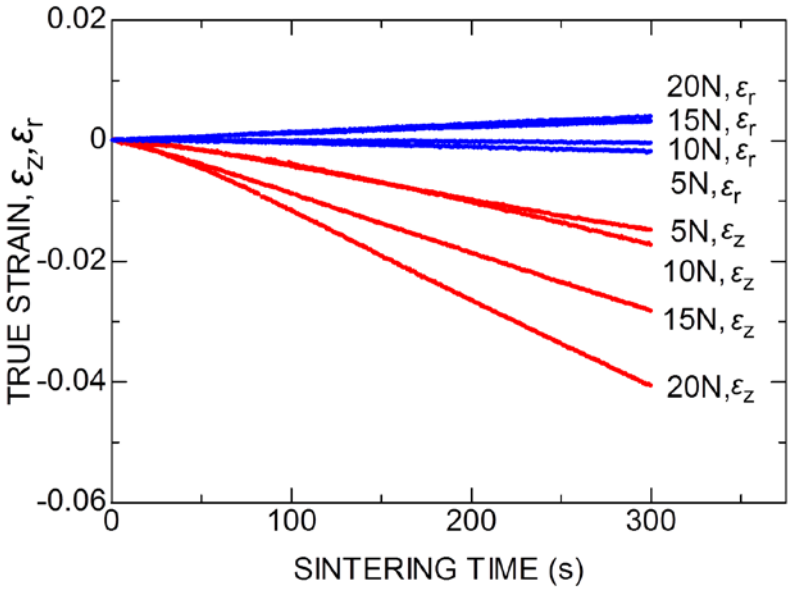

Fig.4.2. Sintering strain curves of CAS glass as a function of sintering time at 850 °C: ε_z is the axial strain and ε_r is the radial strain. A fixed uniaxial load (5, 10, 15, and 20 N) was applied to each pre-sintered specimen with the relative density of 67%.

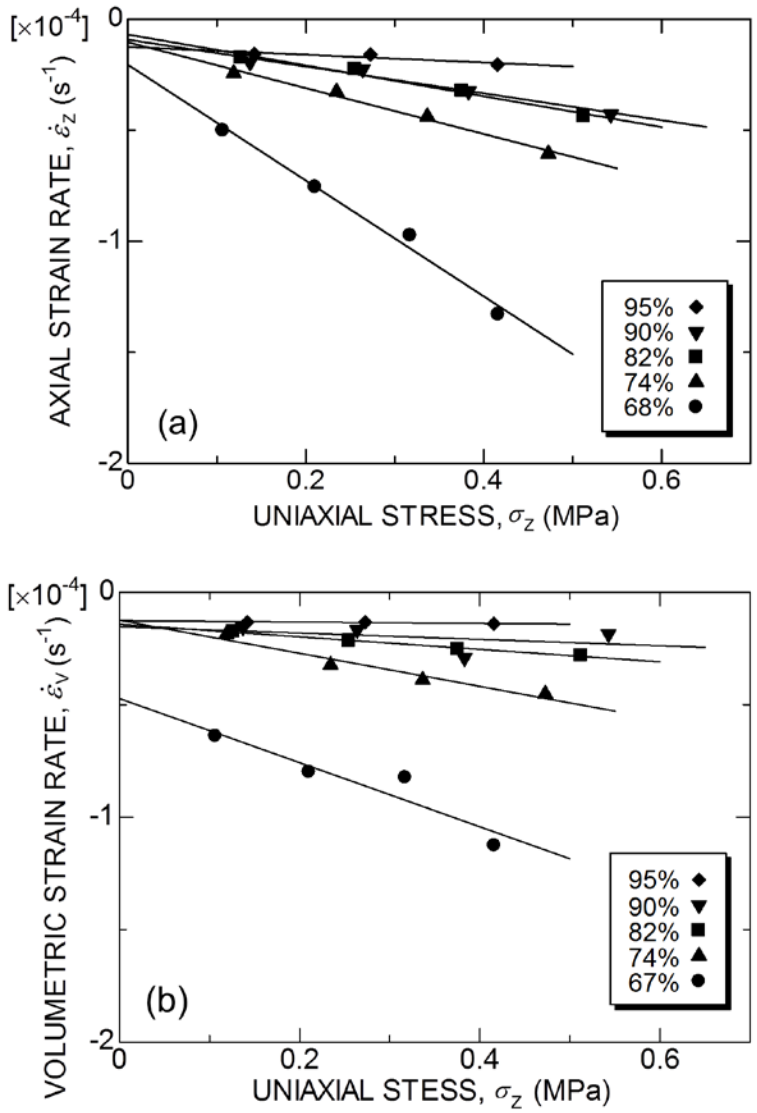

Fig.4.3. Linear relationship between strain rate and uniaxial stress of CAS glass. (a) Axial strain rate ε_z vs. uniaxial stress σ_z, (b) Volumetric strain rate ε_v vs. uniaxial stress σ_z. The relative densities of pre-sintered specimens were 68% (●), 74% (▲), 82% (■), 90% (▼), and 95% (♦).

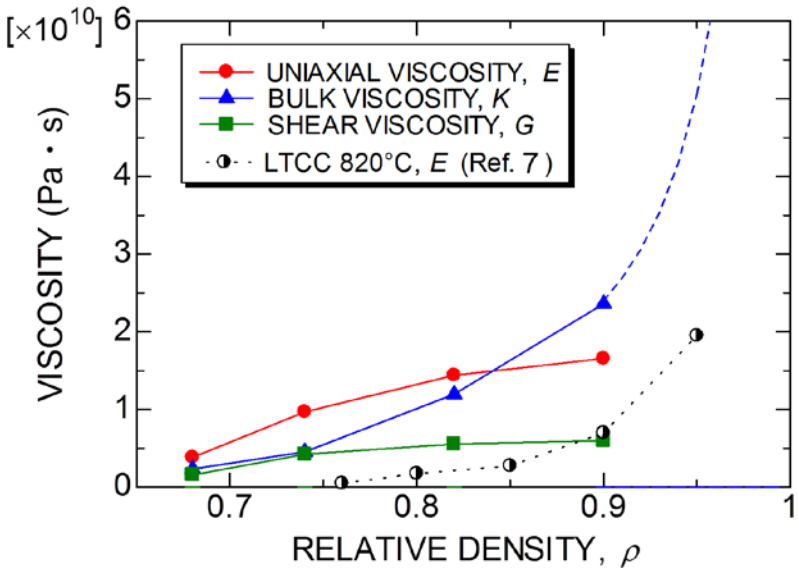

Fig.4.4. Viscosities as a function of relative density at 850 °C. Dashed line shows Mackenzie-Shuttleworth's model on bulk viscosity.

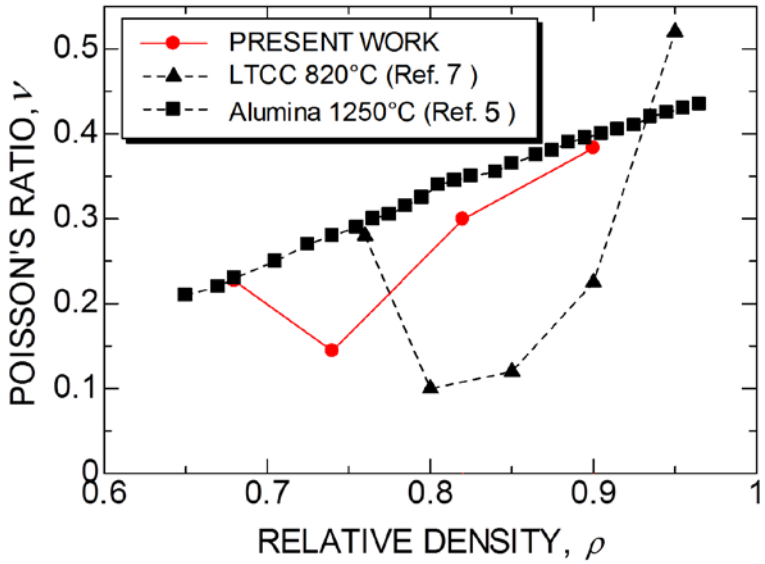

Fig.4.5. Viscous Poisson's ratio as a function of relative density at 850 °C.

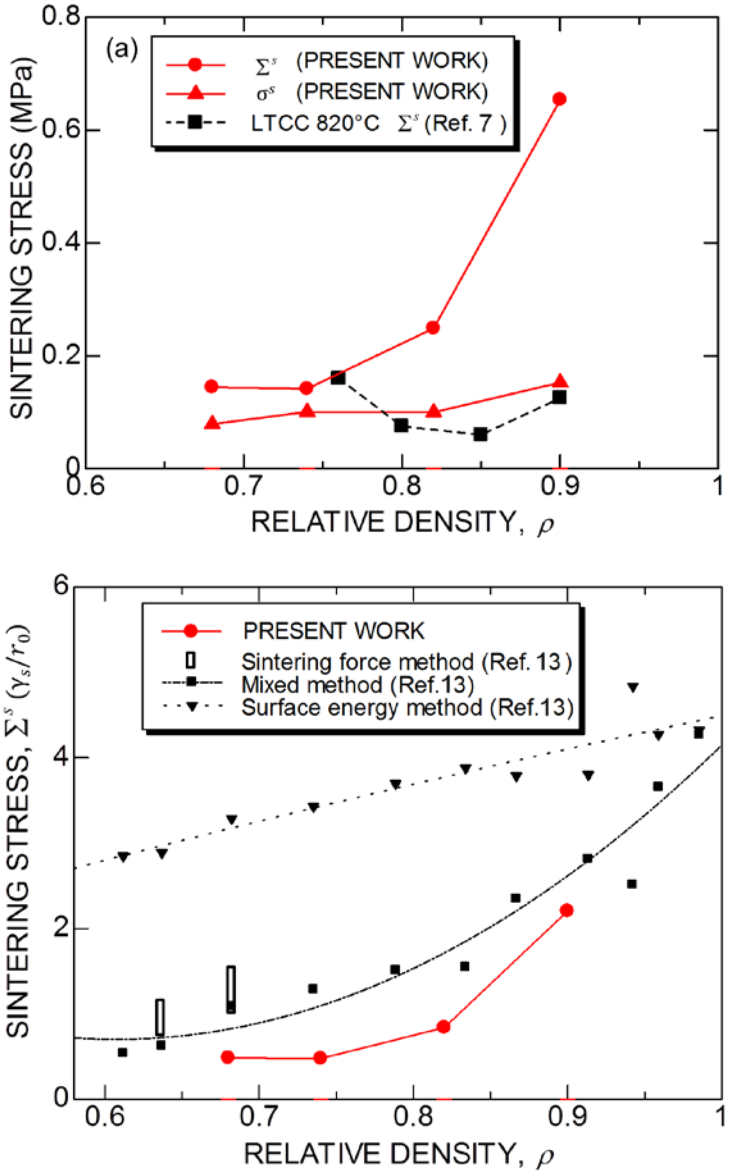

Fig.4.6. Sintering stress as a function of relative density. (a) Sintering stress determined by discrete sinter forging test, (b) Comparison with sintering stress estimated from X-ray microtomography observation.

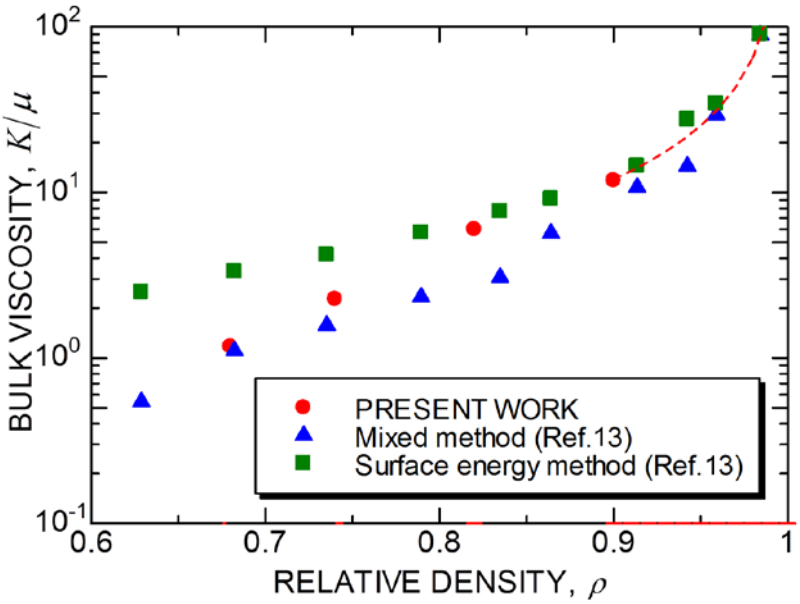

Fig.4.7. Normalized bulk viscosities determined from DSF tests and estimated from X-ray microtomography [13].

Chapter 5 Determination of the size of representative volume element for viscous sintering

5.1 Introduction

The continuum mechanics is normally concerned with the behavior of matter on a macroscopic scale that is large compared with discrete particles. However, although there is general agreement on the need for a unified treatment of continuous media, there is no agreement as to the proper level at which this unification should take place. In this chapter, I introduce the concept of the representative volume element (RVE), which is a volume that is sufficiently large to contain enough information at the micro scale in order to be representative, but it should be much smaller than the macroscopic body.[1] The macroscopic properties in heterogeneous materials are defined as the average over the RVE. This separation of scales is known as the Micro-Meso-Macro principle,[2] so that the property of RVE provides a basis for multiscale analysis. Several works have investigated the existence of an RVE and the possibility to determine its size by using statistical-numerical analysis.[3-7] These studies intended to predict the effective mechanical properties of composites. Recent advances in X-ray microtomography[8] and focused ion beam-scanning electron microscopy[9] have opened the door for observation of detailed microstructural evolution during sintering, and provides an opportunity to analyze the RVE from the knowledge of microstructure experimentally. In the field of particle packing, for example, Razavi and coworkers[10] reported that the concept of RVE provides an effective means of developing macroscopic measures in the description of granular materials. The RVE size has been

determined for electrodes of a Li-ion battery[11] and solid oxide fuel cell.[12-14]

In this chapter, the RVE size was determined from the X-ray microtomography observation for fundamental properties in sintering: relative density, specific surface area, and hydrostatic component of sintering stress. I show that the minimum size of RVE depends on the material property and level of precision required for the analysis. In this chapter, the energy method was used to calculate sintering stress on each stage of sintering. The hydrostatic component of sintering stress in a volume element V is simply calculated from its relative density ρ and its specific surface area $S_V = A_{pore} / V$ for viscous sintering[15,16]

$$\Sigma^s = \frac{2\gamma_s S_V}{3(1-\rho)} \tag{5.1}$$

where γ_s is the surface energy, and A_{pore} is the surface area of pores.

5.2 Experimental procedure

Processing of glass films from spherical particles and synchrotron X-ray microtomography experiment has been performed by Bernard, Guillon, Combaret and Plougorven in Ref. 4. Experimental procedure is described as follows in detail;

A model material was chosen in this study for viscous flow sintering. Spheriglass 5000 powder (Potters Industries, Valley Forge, PA, USA) is composed of glass microspheres of mean size 3.5-8 μm. At least 75% of the particles have a diameter under 12 μm (all particles being smaller than 45 μm). It is a soda lime A glass, composed of 72.5% SiO_2, 13.7% Na_2O, 9.8% CaO, 3.3% MgO, and impurities of aluminium oxide, iron oxide and potassium oxide, at less than 0.4% each (density 2.50

g cm^{-3}, softening point 740 °C).

To obtain a more homogeneous particle size distribution around 8 μm, particles were wet sieved twice (nickel sieves, Precision Eforming, Cortland, NY, USA), in order to remove particles smaller than 7 μm and bigger than 15 μm. Particle size distribution was then measured by means of laser scattering (Analysette 22, Fritsch, Germany). If 99% of all particles of the remainder were below 15 μm and the modal grain size was 7 μm, 25% were still under 3 μm after longer sieving. This will have consequences on the microstructure of tapes and subsequent sintering.

Films ~300 μm thick were tape cast on alumina substrates (Rubalit 710, CeramTec, Germany) by means of a laboratory tape-casting apparatus. First, polyvinylalcohol (PVA) (MW = 10,000-15,000, Erkol, Spain) was dissolved in deionized water to a concentration of 22 wt.% to act as a binder. Powder was gradually added to the solution to obtain an aqueous slurry with 45 vol.% solid content. Polyelectrolyte Dolapix CE64 (Zschimmer & Schwarz GmbH & Co. KG, Germany) was used as a dispersant (0.7 mg m^{-2} of glass powder surface). 1-3 drops of Surfynol DF110D (Air Products BV, the Netherlands) were added to avoid air bubbling. Slurry was homogenized by ultrasonication for >10 min under cooling conditions. After mixing in containers on the rolling bench at medium speed overnight the slurry was homogenized by ultrasonication for a second time and tape-cast on alumina substrate with a blade height of 0.5 mm and at a speed of 1.6 m s^{-1}. After drying overnight in ambient conditions the tapes were cut into 2 × 2 cm^2 squares. The initial film density of about 61.5% was measured by the Archimedes' method performed in water on slightly consolidated specimens, which were easily removed from the underlying substrate.

Sintering conditions were as follows: heating rate of 5 °C min^{-1} up to 600 °C to

obtain a complete binder burn-out and then 20 °C min^{-1} up to 700-750 °C. Isothermal times between 0 and 10 min result in four different densities ranging from ~64% to ~98%. Small pieces with dimensions smaller than 600 μm were cut with a diamond wire saw and glued onto a specimen holder for the synchrotron computed microtomography. Due to the difficulty of specimen preparation, it was impossible to coincide its coordinate system with the global coordinate system of the tape-casting process (except for the thickness).

X-ray microtomography data were acquired by a monochromatic beam (20.5 keV) at the experimental station ID19 of the European Synchrotron Radiation Facility (ESRF, Grenoble, France). Radiographs were acquired by rotating the sample by steps of 0.12° until 180°. The 3-D mapping with voxel size of 0.28 × 0.28 × 0.28 μm were reconstructed were reconstructed from the acquired data by the filtered backprojection method. The 3-D visualization and geometrical measurements were performed using Amira (VSG) in the present study. The watershed transform was used to segment the gray value image into pore and material. The pore surface was discretized using triangular meshing, from which the surface area and the pore volume were calculated.

5.3 Results and discussion

5.3.1 Micro structural evolution in viscous sintering

The pore space evolution in viscous sintering of spherical glass particles observed by synchrotron X-ray microtomography are shown in Figure 5.1. In the initial stage (Fig. 5.1(a), Stage 1), the pore structure is a continuous network with numerous circular holes resulting from contacts between particles. As holes expand with the neck growth, ligaments are pinched-off, breaking the continuous network into fragments:

closed pores are formed one by one in the intermediate stage (Fig. 5.1(b) Stage 2, and (c) Stage 3). Complicated shaped pores become spherical in the final stage of sintering (Fig. 5.1(d) Stage 4).

Figure 5.2 shows a 2-D section extracted from the specimen in Stage 1, which is easier to examine the microstructural heterogeneity. The smallest particles have segregated at the bottom of the layer, then, I analyze the average properties of the layer in the middle region marked in Fig. 5.2. Sub-volumes extracted from a total material domain are restricted to cubic geometries. As many as possible independent cubes with edge length of 160, 80, 40, 20, and 10 μm were extracted from each sample for four stages. The RVE size is given by using the edge length L of cubic volume element.

5.3.2 Relative density, specific surface area and sintering stress

The relative density of sub-volume in each stage is plotted as a function of the edge length of cubic volume element in Fig.5.3. I measure the relative density of sub-volume by the local threshold method using Amira (VSG). Figures in brackets refer to the number of sub-volumes. The mean relative density is almost independent of edge length when sufficiently large number of sub-volumes is analyzed; the number of voxels per particle diameter was 29 in the present experiments. The scatter of data at small edge length indicates the scale of microstructural inhomogeneity. Figures 5.4 and 5.5 show the specific surface area and the sintering stress as functions of edge length. For all three quantities the scatter of data increases with decreasing the edge length L, while their mean values were almost independent of the edge length.

Both mean value of specific surface area and that of sintering stress depends on sintering stage or mean value of relative density. The linear relation was observed

between mean specific surface and mean relative density.[15] The mean sintering stress was almost constant from stage 1 to stage 3, and decreased slightly at the final stage. In the final stage of sintering, where closed pores are dispersed sparsely, the macroscopic sintering stress is dominated by the largest residual pores.[16] The mean sintering stress decreased in stage 4, because the coarsening in pore structure resulted in residual pores more than two times larger than the initial particle size as shown in Fig. 5.1(d).

Standard deviation for given edge length is shown in Fig. 2.6, as a function of L. It can be seen that the standard deviation is quite large for a small L; it decreases as L increases, and converges to a constant value. The variation of standard deviation on L reflects the microstructural heterogeneity. I may assign the edge length L_r , above which the heterogeneity no longer affects the standard deviation, as the minimum size of the RVE. From this definition the RVE size is estimated to be from 90 μm to 135 μm for relative density, specific surface area, and sintering stress. Here, the non-dimensional RVE size L * is defined as

$$L^* = L/d \qquad (2.2)$$

where d is the average initial particle size (8 μm). The non-dimensional RVE size was from 11 to 17 in the present experiments. This result agrees with the values reported for granular materials.[10] However, this normalization is done with respect to the initial microstructure, which completely disappears during sintering.

Alternatively the RVE size can be defined from standard deviation-edge length curves. Since both mean value and standard deviation of each quantity varies with relative density, we normalized standard deviation by the mean value at stage 1 (ρ=63.5%).

The RVE size was defined with the normalized standard deviation; either 5 % or

2 % for the RVE size of relative density $L_{r,d}$, and specific surface area $L_{r,a}$, and either 8 % or 5 % for that of sintering stress $L_{r,s}$ .The RVE size was plotted as a function of relative density in Figure 5.7. The RVE size must be larger when the desired accuracy is higher. The RVE size of relative density (Fig. 5.7(a)) is relatively small in stage 1 where inhomogeneities can be envisioned as local fluctuation caused by differences in random particle packing. However, larger RVE size in the later stages suggests that the characteristic length to describe microstructural heterogeneity increases from the particle size to the distance between coarse spherical pores during the microstructural evolution. The increase in the characteristic length can be called coarsening in a broad sense. The RVE size of specific surface area (Fig. 5.7(b)) decreased at stage 4. We suppose it is an artifact due to the definition of $L_{r,a}$, from the normalized standard deviation, because the mean value of specific surface area and also its standard deviation approach to zero at the final stage of sintering. The RVE size of sintering stress (Fig. 2.7(c)) increased with densification. The scatter of sintering stress in each volume element increases with the relative density ρ, because the sintering stress is inversely proportional to porosity $1-\rho$ which is close to zero in the final stage. Since the sintering stress is dominated by the largest pores, the RVE size for sintering stress is related to the average distance between large pores in the final stage.

5.4 Conclusions

The microstructural evolution of thin glass film during constrained sintering on a rigid substrate, imaged by synchrotron X-ray microtomography, was analyzed to evaluate fundamental quantities, i.e., relative density, specific surface area, and sintering stress. These parameters are important for the continuum mechanical description of viscous sintering. The minimum size of RVE was defined as the edge length of cubic volume elements above which the heterogeneity no longer affects the standard deviation.

The RVE size was estimated to be from 11 to 17 times larger than the average initial particle size. Alternatively the RVE size was defined from the value of normalized standard deviation. The RVE size increased when the desired accuracy was higher. The RVE size was dependent on relative density, and varied with microstructural evolution. The relationship between RVE size and relative density was dependent on the physical property of interest.

References

1. R. Hill. Elastic properties of reinforced solids: Some theoretical principles. J. Mech. Phys. Solids, 11, 357-372 (1963).

2. Z. Hashin, Analysis of Composite Materials—A Survey. J. Appl. Mech. 50, 481-505 (1983).

3. W. J. Drugan and J.R. Willis, J. Mech. Phys. Solids. A micromechanics-based nonlocal constitutive equation and estimates of representative volume element size for elastic composites. 44, 497-524 (1996).

4. K. Kanit, S. Forest, I. Galliet, V. Mounoury and D. Jeulin. Determination of the size of the representative volume element for random composites: statistical and numerical approach. Int. J. Solids Structures, 40, 3647-3679 (2003).

5. I. M. Gitman, H. Askes and L.J. Sluys. Representative volume: Existence and size determination. Engineering Fracture Mechanics 74, 2518-2534 (2007).

6. C. Pelissou, J. Baccou, Y. Monerie and F. Perales. Determination of the size of the representative volume element for random quasi-brittle composites. Int. J. Solids Structures, 46, 2842-2855 (2009).

7. W. M. Harris and W.K.S. Chiu. Determining the representative volume element size for three-dimensional microstructural material characterization. Part 1: Predictive models. J. Power Sources, 282, 552-561 (2015).

8. D. Bernard, O. Guillon, N. Combaret and E. Plougonven. Constrained sintering of glass films: Microstructure evolution assessed through synchrotron computed microtomography. Acta. Mater. 59, 6228-6238 (2011).

9. S. Hara, A. Ohi, N. Shikazono. Sintering analysis of sub-micron-sized nickel powders: Kinetic Monte Carlo simulation verified by FIB–SEM reconstructionJ. Power

Sources. 276, 105-112 (2015).

10. M. R. Razavi, B. Muhunthan, O. A. Hattamleh. Representative elementary volume analysis of sands using X-ray computed tomography. Geotechnical Testing Journal, 30, No. 3 (2007)

11. P. R. Shearing, L. E. Howard, P. S. Jorgensen, N. P. Brandon and S.J. Harris. Characterization of the 3-dimensional microstructure of a graphite negative electrode from a Li-ion battery. Electrochem. Commun.12, 374-377 (2010).

12. J. Joos, M. Ender, T. Carraro, A. Weber and E. Ivers-Tiffee. Representative volume element size for accurate solid oxide fuel cell cathode reconstructions from focused ion beam tomography data. Electrochimica. Acta, 82, 268-276 (2012).

13. J. Laurencin, R. Quey, G. Delette, H. Suhonen, P. Cloetens and P. Bleuet. Characterisation of Solid Oxide Fuel Cell Ni–8YSZ substrate by synchrotron X-ray nano-tomography: from 3D reconstruction to microstructure quantification. J. Power Sources. 198, 182-189 (2012).

14. W.M. Harris and W.K.S. Chiu. Determining the Representative Volume Element Size for Three-Dimensional Microstructural Material Characterization—Part 2: Application to Experimental Data. J. Power. Sources. 283, 622-629 (2015).

15. F. Wakai, O. Guillon. Evaluation of sintering stress from 3-D visualization of microstructure: case study of glass films sintered by viscous flow and imaged by x-ray microtomography. Acta. Mater. 66, 54-62 (2014).

16. F. Wakai. Mechanics of viscous sintering on the micro-andmacro-scale. Acta. Mater. 61, 239-247 (2013).

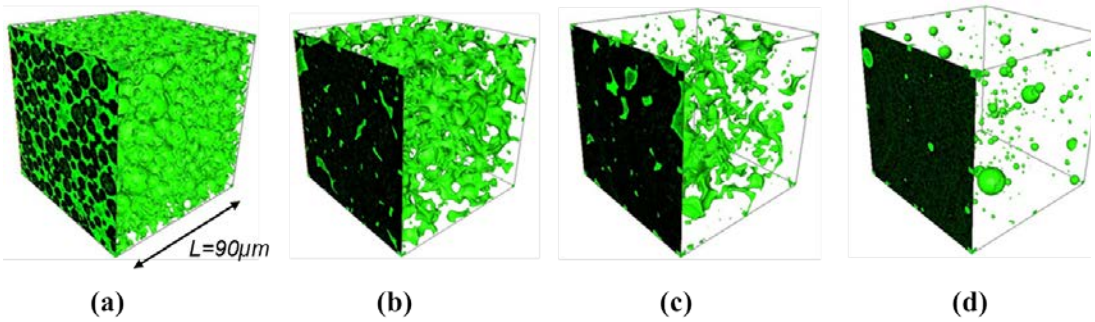

Fig.5.1 Evolution of pore space in sintering: (a) stage1 (relative density, ρ=63.5%); (b) stage2 (ρ=87.8%); (c) stage3 (ρ=94.1%); (d) stage4 (ρ=98.4%).

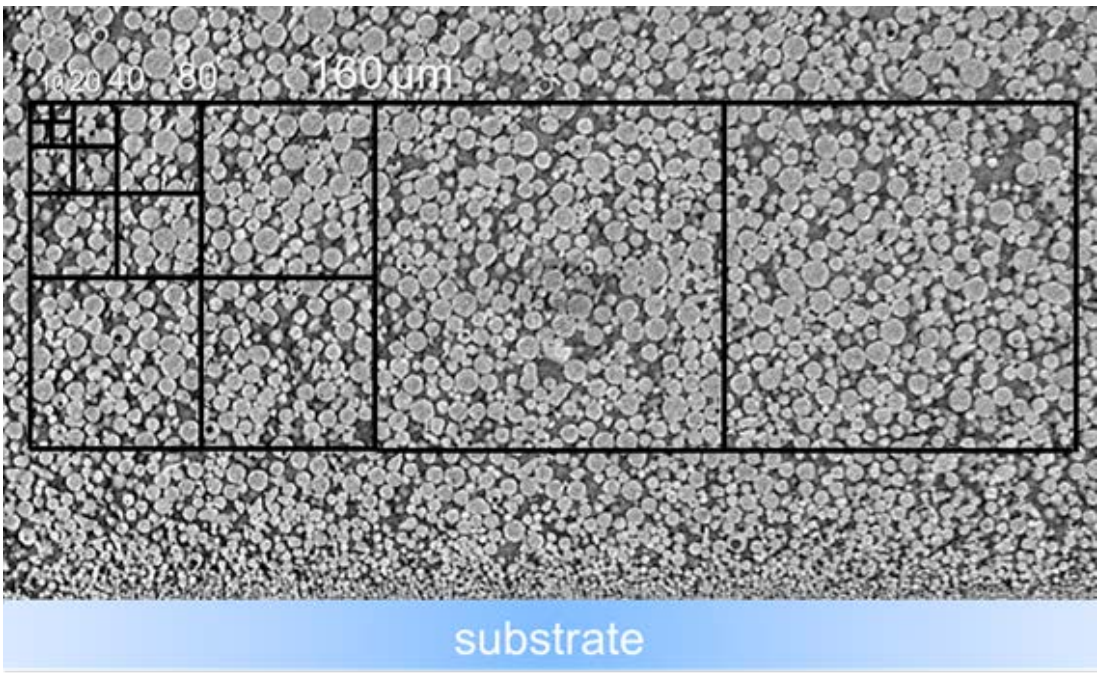

Fig.5.2 Section of a sample (stage1, relative density ρ =63.5%). The size of cubic volume elements are illustrated for comparison to the initial particle diameter.

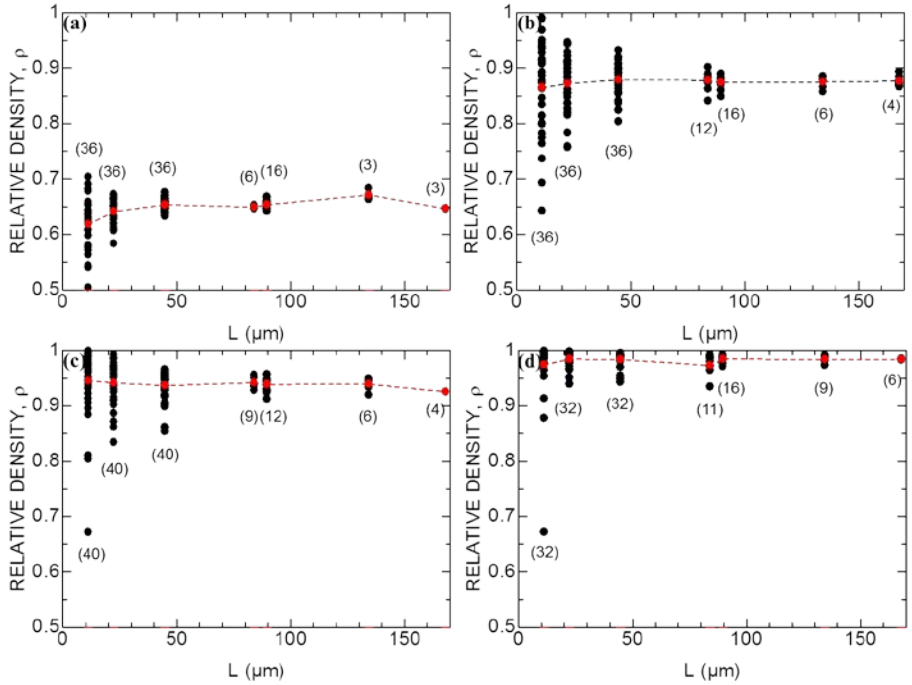

Fig.5.3. Relative density of each volume element : (a) stage1; (b) stage2; (c) stage3; (d) stage4. The dotted line shows the mean value.

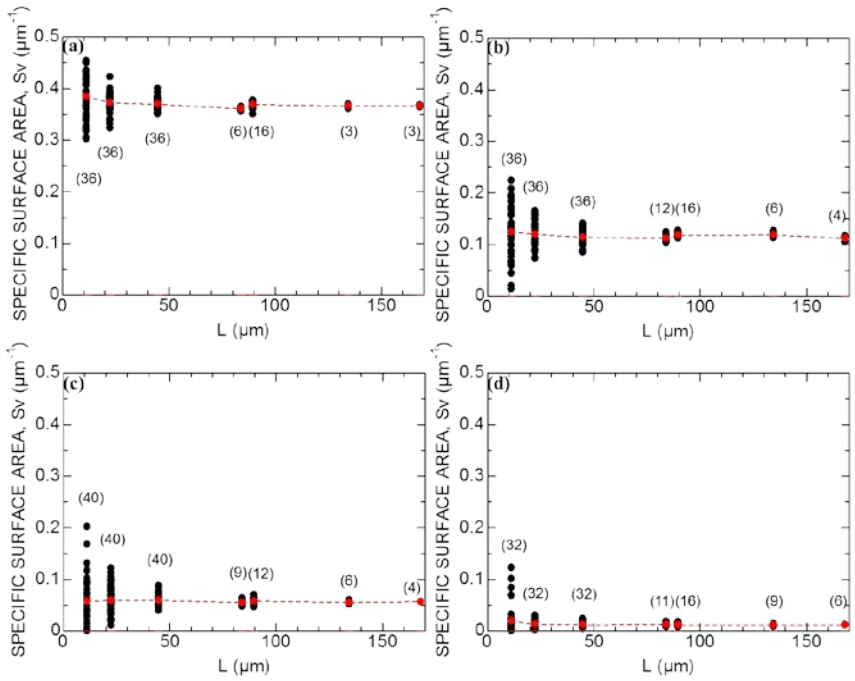

Fig.5.4. Specific surface area of each volume elements: (a) stage1; (b) stage2; (c) stage3; (d) stage4. The dotted line shows the mean value.

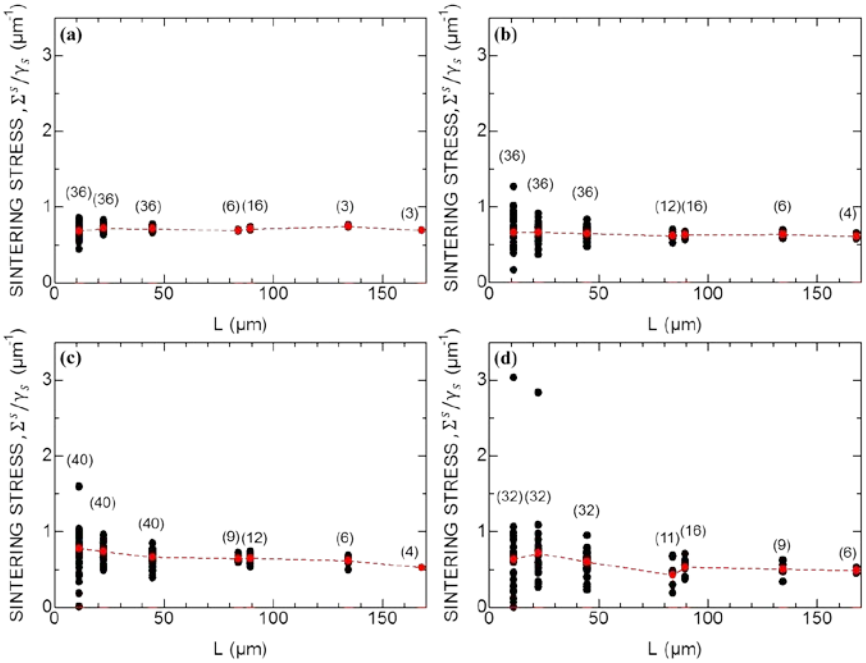

Fig.5.5. Sintering stress of each volume element: (a) stage1; (b) stage2; (c) stage3; (d) stage4. The dotted line shows the mean value.

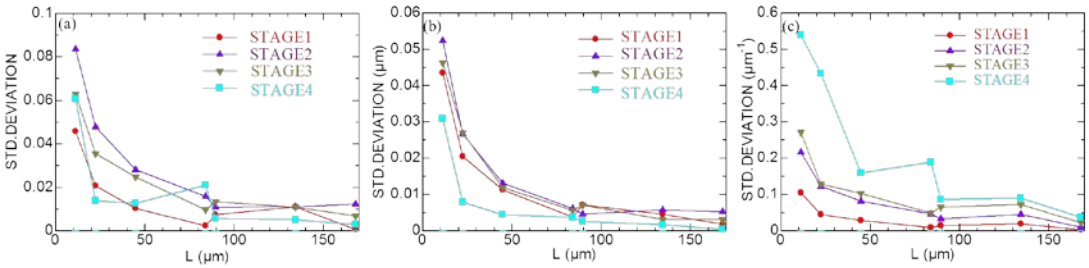

Fig.5.6. Standard deviation as a function of the edge length of cubic elements: (a) relative density; (b) specific surface area; (c) sintering stress.

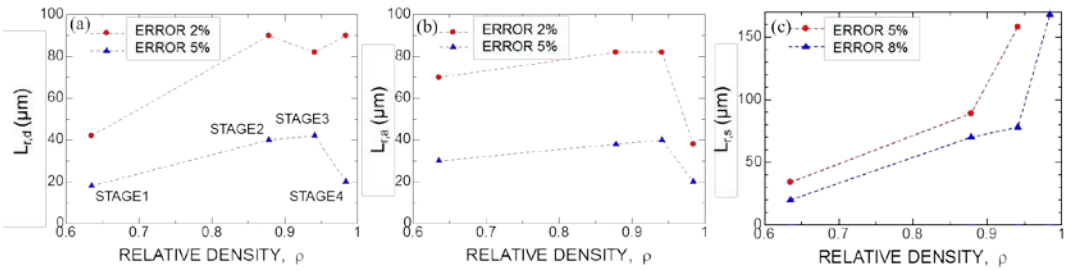

Fig.5.7. RVE size as a function of relative density. (a) relative density ($L_{r,d}$), (b) specific surface area of pores ($L_{r,a}$), and (c) sintering stress ($L_{r,s}$) .

Chapter 6 Summary

The purpose of this doctoral dissertation is to construct the experimental and theoretical methods to estimate sintering parameters, such as sintering stress that is the thermodynamic driving force for sintering, and bulk viscosity, which are fundamental quantities for predicting the macroscopic shrinkage behavior in sintering, from 3D visualization of microstructures observed by X-ray microtomography. Glass was chosen as a model material, because the mechanism of material transport during sintering of glass is much simpler than that of crystalline particle, and hence, we only consider about viscous flow mechanism. The speedy and reliable method of predicting the sintering stress and bulk viscosity was proposed in this research.

This doctoral dissertation was divided into 6 chapters, and abstract of each chapter was described as below;

Chapter 1: Introduction

The macroscopic continuum mechanics of sintering and the sintering process in microscopic scale were described, followed by the objective of this doctoral dissertation.

Chapter 2: **Interface topology for distinguishing stages of sintering**

Sintering is a common process during which nanoparticles and microparticles are bonded, leading to the shrinkage of interstitial pore space. Understanding morphological evolution during sintering is a challenge, because pore structures are elusive and very complex. A topological model of sintering is presented here,

providing insight for understanding 3-D microstructures observed by X-ray microtomography. It is found that the topological evolution is described by Euler characteristics as a function of relative density. The result is general, and applicable not only to viscous sintering of glasses but also to sintering of crystalline particles. It provides criteria to distinguish the stages of sintering, and the foundations to identify the range of applicability of the methods for determining the thermodynamic driving force of sintering.

Chapter 3: **Computation of sintering stress and bulk viscosity for each stage of sintering**

Sintering stress and bulk viscosity were derived as functions of relative density from microtomographic images in viscous sintering of glass particles. Three methods were proposed to estimate the sintering stress from relative density, specific surface area, and average of curvature on pore surface, which were directly measured by X−ray microtomography. These methods for determining sintering stress should be selected depending on sintering stage, which was determined in chapter 2. The surface energy method gave valid value in the final stage of sintering, while the mixed method gave better estimation in the intermediate stage. For the initial stage of sintering, the sintering stress was calculated from the average contact radius and the average coordination number observed by X‐ray microtomography. The sintering stress at the final stage increased in free sintering, but it decreased in constrained sintering due to pore coarsening. The bulk viscosity was calculated from the shrinkage rate and the sintering stress.

Chapter 4: Experimental verification of sintering stress and bulk viscosity estimated from X-ray microtomography

The macroscopic sintering parameters, sintering stress, bulk viscosity, and shear viscosity, were measured by the discontinuous sinter forging experiment for viscous sintering of calcium aluminosilicate (CAS) glass. The calculated results were compared with experimental values from the microstructural evolution during viscous sintering of spherical soda lime glass particles by X-ray microtomography in chapter 3. The sintering stress of CAS glass normalized by surface energy and the initial particle size was in good agreement with values estimated from the microtomography data of soda lime glass, despite the differences in particle shape and chemical composition. The bulk viscosity obtained by discontinuous sinter forging agreed fairly well with that estimated by X-ray microtomography observation, when they were normalized by glass viscosity.

Chapter 5: Determination of the size of representative volume element for viscous sintering

The representative volume element (RVE) is a basic concept in the continuum mechanics of sintering of random heterogeneous porous materials. A quantitative determination of its size was performed by using synchrotron X-ray microtomography data of constrained sintering of thin glass film on a rigid substrate. A RVE size is associated with a property of interest; I determined it for relative density, specific surface area, and hydrostatic component of sintering stress. The RVE size was estimated to be from 11 to 17 times larger than the average initial particle size. The RVE size was associated with a given precision of the property. It depended on the volume fraction of porous structure, or, relative density, so that it varied with microstructural evolution.

List of publications

(1) Journal Paper (Reviewed)

1) G. Okuma, J. Gonzalez-Julian, O. Guillon, F. Wakai, Comparison between sinter forging and X-ray microtomograhy methods for determining sintering stress and bulk viscosity, J. Euro. Ceram. Soc, 38, 4, 2053-2058, (2018).

2) G. Okuma, D. Kadowaki, T. Hondo, S. Tanaka, F. Wakai,
Interface topology for distinguishing stages of sintering, Sci Rep,**7**, 11106 (2017).

3) G. Okuma, D. Kadowaki, T. Hondo, A. Sato, S. Tanaka, F. Wakai, Computation of Sintering Stress and Bulk Viscosity from Microtomographic Images in Viscous Sintering of Glass Particles, J. Am. Ceram. Soc, **100**, 867-875 (2017).

4) G. Okuma, D. Kadowaki, Y. Shinoda, T. Akatsu, O. Guillon and F. Wakai, Determination of the size of representative volume element for viscous sintering, J. Ceram. Soc. Japan, **124** [4], 421-425 (2016).

5) F. Wakai, O. Guillon, **G. Okuma**, N. Nishiyama, Sintering Forces Acting among Particles during Sintering by Grain Boundary/Surface Diffusion, J. Am. Ceram. Soc. DOI10.1111/jace.15716

(2) Other publication - Review article

6) G. Okuma, F. Wakai, S. Tanaka, T. Hondo, J. Gonzalez-Julian, O. Guillon, , Determination of sintering stress and bulk viscosity from sinter-forging and X-ray microtomography methods, Materials Today Proceedings, ISAC-6 (2018). submitted

7) 大熊 学, 菅近 駿, 田中 諭, 若井 史博, X 線マイクロトモグラフィーによる焼結過程の微構造の 3 次元可視化と巨視的力学量の評価, 粉体粉末冶金 講演特集 第 64 巻 第 9 号 495-500 (2017). 査読有

8) 大熊 学, 若井 史博, 粉体成形プロセスにおける微視的な粒子充填構造と焼結における巨視的な収縮との関連の 3 次元トモグラフィーによる解明, ホソカワ粉体工学振興財団年報 No.24, 144-147 (2016).　査読無

List of presentations

(1) International conference

1) **G. Okuma**, S. Tanaka and F. Wakai, Distinction of stages of sintering from 3D visalization of microstructure in sinteting by using X-ray microtomography, 42nd International Conference and Exposition on Advanced Ceramics and Composites, Daytona Beach, Florida, USA, January (2018). **(Invited)**

2) **G. Okuma**, F. Wakai , J. Gonzalez-Julian, O. Guillon, Comparison between sinter forging and X-ray microtomograhy methods for determining sintering stress and bulk viscosity, 6th International Symposium on Advanced Ceramics (ISAC-6) March (2018). **(Reviewed)**

3) **G. Okuma**, F. Wakai , J. Gonzalez-Julian, O. Guillon, Sinter forging and X-ray microtomograhy methods for determining sintering stress and bulk viscosity, The 6th International Conference on Characterization and Control of Interface for High Quality Advanced Materials (ICCCI2018) July (2018). **(Student Poster Award)**

4) **Gaku Okuma**, Satoshi Tanaka, Fumihiro Wakai. Mechanics and evolution of microstructural topology in viscous sintering observed by X-ray microtomography, Sintering2017, Nov (2017). **(Reviewed)**

5) **Gaku Okuma**, Daiki Kadowaki, Satoshi Tanaka, Fumihiro Wakai. Mechanics and evolution of interfacial topology for distinguishing stages of sintering, The Sixth International Education Forum, Dec (2017). **(Reviewed)**

6) **Gaku Okuma**, Daiki Kadowaki, Tsuyoshi Hondo, Satoshi Tanaka, Fumihiro Wakai. Evolution of interface topology from microscopic observation of viscous sintering of glass particles by using X-ray microtomography, The 34th International Japan-Korea Seminar on Ceramics, Nov (2017).

7) **Gaku Okuma**, Daiki Kadowaki, Satoshi Tanaka, FUMIHIRO WAKAI. Distinction of sintering stage by interfacial topology, The 10th International Conference on the Science and Technology for Advanced Ceramics (STAC-10), Aug (2018). **(Poster Award)**

8) **G. Okuma**, D. Kadowaki, S. Tanaka, F. Wakai. Bulk viscosity and sintering stress in viscous sintering of glass particles estimated from microscopic observation by using X-ray microtomogtaphy, The Fifth International Education Forum, Dec (2016).

(Reviewed)

9) **G. Okuma**, D. Kadowaki, S. Tanaka, F. Wakai. Estimation of bulk viscosity and sintering stress from microscopic observation of viscous sintering of glass particles by using X-ray microtomography, The International Symposium on the Science of Engineering Ceramics (EnCera 2016), May (2016). **(Best Poster Award)**

10) **G. Okuma**, D. Kadowaki, F. Wakai. Size Determination of Representative Volume Element in Microstructure Evolution during Sintering, The Fourth International Education Forum, Dec (2015). **(Reviewed)**

11) **G. Okuma**, D. Kadowaki, F. Wakai. Size determination of representative volume element in microstructure evolution during sintering, The 9th International Conference on the Science and Technology for Advanced Ceramics (STAC-9), Oct (2015).

12) Fumihiro Wakai, **Gaku Okuma**, Norimasa Nishiyama. Role of microscopic forces in densification of particles in solid state sintering, The 6th International Symposium on Advanced Ceramics (ISAC-6), Mar (2018).

13) Fumihiro Wakai, Shun Kanchika, **Gaku Okuma**, Norimasa Nishiyama. Microscopic sintering forces acting among particles during sintering by grain boundary/surface diffusion, Sintering2017, Nov (2017).

14) Fumihiro Wakai, **Gaku Okuma**, Satoshi Tanaka. Microscopic Sintering Forces behind Macroscopic Continuum Theory of Sintering, Japan-India YNU Symposium 2017, Dec (2017).

(2) Domestic conference

15) 大熊 学, Jesus Gonzalez-Julian, O. Guillon, 若井 史博. X 線トモグラフィーにより推定した焼結応力の焼結鍛造試験による実験的検証, 平成 30 年度春季大会 (第 121 回講演大会) 粉末冶金協会, May (2018).

16) 大熊 学, Jesus Gonzalez-Julian, O. Guillon, 若井 史博. 焼結鍛造試験による焼結応力および粘性係数の決定と X 線マイクロトモグラフィーによる微視的構造観察からの推定結果との比較, 日本セラミックス協会 2018 年年会, Mar (2018).

17) 大熊学, 門脇大騎, 田中諭, 若井史博. 焼結中の微構造の 3 次元可視化による焼結段階の分類, 第 56 回セラミックス基礎科学討論会, Jan (2018).

18) 大熊 学, 門脇 大騎, 田中 諭, 若井 史博. 焼結段階を区別するための界面トポロジー, 第 30 回日本セラミックス協会秋季シンポジウム, Sep (2017).

19) 大熊 学, Jesus Gonzalez-Julian, Olivier Guillon, 若井 史博. 焼結鍛造試験による焼結応力および粘性係数の決定と X 線マイクロトモグラフィーによる微視的構造観察からの推定結果との比較, 第 55 回セラミックス基礎科学討論会, Jan (2017).

20) 大熊 学, 門脇 大騎, 田中 諭, 若井 史博. 焼結段階を区別するための界面トポロジー, バルクセラミックスの信頼性に関するワークショップ（第 6 回バルクセラミックス若手セミナーを兼ねる）, Sep (2017).

21) 大熊 学, 門脇 大騎, 田中 諭, 若井 史博. X 線マイクロトモグラフィーによるガラス粒子の粘性焼結における微視的構造観察からの巨視的粘性係数と焼結応力の推定, 第 29 回日本セラミックス協会秋季シンポジウム, Sep (2016).

22) 大熊 学, 門脇 大騎, 田中 諭, 若井 史博. X 線マイクロトモグラフィーによるガラス粒子の粘性焼結の微視的構造観察からの巨視的粘性係数と焼結応力の推定, 平成 28 年度春季大会 (第 117 回講演大会) 粉末冶金協会, May (2016).

23) 大熊 学, 門脇 大騎, 篠田 豊, 赤津 隆, 若井 史博. 焼結中の微構造変化における代表体積要素の寸法決定, 第 28 回日本セラミックス協会秋季シンポジウム, Sep (2015).

24) 若井 史博, 大熊 学, 西山 宣正, Olivier Guillon, 3 粒子の固相焼結の背後にある焼結力, 日本セラミックス協会 2018 年年会, Mar (2018).

25) 若井史博, 大熊学, 田中諭. 焼結プロセスにおける内部応力の起源のミクロスケール力学解析, 第 37 回エレクトロセラミックス研究討論会, Oct (2017).

26) 若井 史博, 大熊 学, 田中 諭, Olivier Guillon. 理論とシミュレーションに基づく X 線マイクロトモグラフィー観察からの粘性焼結の構成式の推定, 平成 28 年度秋季大会 (第 118 回講演大会) 粉末冶金協会, Nov (2016).

27) 門脇 大騎, 大熊 学, 若井 史博, 本堂 剛, 佐藤 暁洋, 田中 諭. X 線マイクロトモグラフィーによるガラス粒子の粘性焼結における気孔形態の 3 次元解析, 第 28 回日本セラミックス協会秋季シンポジウム, Sep (2015).

Achievement

(1) Grant

1) 日本学術振興会(JSPS) 特別研究員奨励費 - DC2

研究課題名: 3 次元可視化による焼結の熱力学的駆動力の解明と制御

2) ホソカワ粉体工学振興財団 研究者育成のための援助

研究課題名: 粉体成形プロセスにおける微視的な粒子充填構造と焼結における巨視的な収縮との関連の 3 次元トモグラフィーによる解明

3) SPring-8: 2018A 大学院生提案型課題（旧名：萌芽的研究支援課題）

研究課題名: 結像型 CT による焼結プロセスのナノスケール 3 次元観察

(2) Scholar ship

4) 日本学生支援機構(JASSO) 特に優れた業績による全額返還免除 (修士課程)

5) 日本学生支援機構(JASSO) 特に優れた業績による返還免除 (博士課程-二年次)

(3) Awards

6) Student Poster Award – Sinter forging and X-ray microtomography methods for determining sintering stress and bulk viscosity, ICCCI2018, Kurashiki, July (2018)

7) Poster Award - Distinction of sintering stage by interfacial topology, The 10th International Conference on the Science and Technology for Advanced Ceramics STAC10, Yokohama, Aug (2017)

8) Best Poster Award - Estimation of bulk viscosity and sintering stress from microscopic observation of viscous sintering of glass particles by using X-ray microtomography, The International Symposium on the Science of Engineering Ceramics, EnCera2016, Niigata, May (2016)

(4) Invited lecture

9) Distinction of stages of sintering from 3D visalization of microstructure in sinteting by using X-ray microtomography, 42nd ICACC, Daytona Beach, Florida, USA, January (2018)

Acknowledgements

This work was mainly supported by Prof. Fumihiro Wakai. I would like to express my sincere gratitude to Prof. Wakai. In addition, Associate Prof. Norimasa Nishiyama, Dr. Yutaka Shinoda, Prof. Satoshi Tanaka (Nagaoka University of Technology), Daiki Kadowaki and laboratory roommates give me some advice. Thanks a lot.